Computer simulations of supercooled polymer melts in the bulk and in confined geometry

2005 J. Phys.: Condens. Matter 17 R851

(http://iopscience.iop.org/0953-8984/17/32/R02)

INSTITUTE OF PHYSICS PUBLISHING JOURNAL OF PHYSICS: CONDENSED MATTER

J. Phys.: Condens. Matter **17** (2005) R851–R953 doi:10.1088/0953-8984/17/32/R02

TOPICAL REVIEW

Computer simulations of supercooled polymer melts in the bulk and in confined geometry

J Baschnagel[1] **and F Varnik**[2]

[1] Institut Charles Sadron, 6 rue Boussingault, 67083 Strasbourg Cedex, France
[2] Max-Planck-Institut für Eisenforschung, Max-Planck-Straße 1, 40237 Düsseldorf, Germany

E-mail: baschnag@ics.u-strasbg.fr and varnik@mpie.de

Received 6 June 2005
Published 29 July 2005
Online at stacks.iop.org/JPhysCM/17/R851

Abstract

We survey results of computer simulations for the structure and dynamics of supercooled polymer melts and films. Our survey is mainly concerned with features of a coarse grained polymer model—a bead–spring model—in the temperature regime above the critical glass temperature T_c of the ideal mode-coupling theory (MCT). We divide our discussion into two parts: a part devoted to bulk properties and a part dealing with thin films. The discussion of the bulk properties focuses on two aspects: a comparison of the simulation results with MCT and an analysis of dynamic heterogeneities. We explain in detail how the analyses are performed and what results may be obtained, and we critically assess their strengths and weaknesses. In discussing the application of MCT we also present first results of a quantitative comparison which does not rely on fits, but exploits static input from the simulation to predict the relaxation dynamics. The second part of this review is devoted to extensions of the simulations from the bulk to thin films. We explore in detail the influence of the boundary condition, imposed by smooth or rough walls, on the structure and dynamics of the polymer melt. Geometric confinement is found to shift the glass transition temperature T_g (or T_c in our case) relative to the bulk. We compare our and other simulation results for the T_g shift with experimental data, briefly survey some theoretical ideas for explaining these shifts and discuss related simulation work on the glass transition of confined liquids. Finally, we also present some technical details of how to perform fits to MCT and give a brief introduction to another approach to the glass transition based on the potential energy landscape of a liquid.

0953-8984/05/320851+103$30.00

Contents

1. Introduction

Polymer melts are bulk liquids consisting of macromolecules [1]. In the simplest case of linear homopolymers each macromolecule contains N monomeric repeat units of the same type, which are connected to form a chain. The chain length N may be large. A typical range in experiments is $10^3 \lesssim N \lesssim 10^5$. This implies that the average size of a polymer, measured e.g. by the radius of gyration R_g [2, 3], varies between $R_\mathrm{g} \sim 100$ Å and $R_\mathrm{g} \sim 1000$ Å. The size of a chain thus exceeds that of a monomer ($\sim$1 Å) by several orders of magnitude.

These different length scales are reflected in the particular features of a polymer melt. In the melt the monomers pack densely, leading to an amorphous short range order on a local scale and to an overall low compressibility of the melt. Both features are characteristic of the liquid state. Qualitatively, the collective structure of the melt thus agrees with that of nonpolymeric liquids. Additional features, however, occur if one considers the scale of a chain. A long polymer in a (three-dimensional) melt is not a compact, but a self-similar object [3–5]. It possesses a fractal ‘open’ structure which allows other chains to penetrate into the volume defined by its radius of gyration. On average, a polymer experiences $\sqrt{N}$ intermolecular contacts with other chains, a huge number in the large N limit. This strong interpenetration of the chains has important consequences. For instance, intrachain excluded volume interactions, which would swell the polymer in dilute solution, are screened by neighbouring chains [2–4, 6–8]. A polymer in a melt thus behaves on large scales as if it were a random coil, implying that its radius of gyration scales with chain length like $R_\mathrm{g} \sim \sqrt{N}$. Furthermore, the interpenetration of the chains creates a temporary network of topological constraints [2–4, 9]. These entanglements

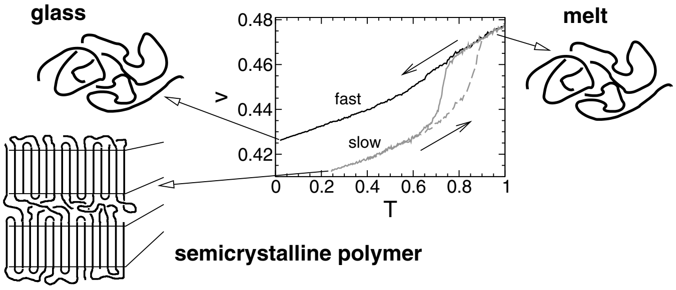

Figure 1. Volume per monomer v versus temperature T for a polymer melt which tends to crystallize. In the high T liquid phase the chains have configurations that are random coil-like and the structure of the melt is amorphous. The amorphous structure is preserved when the melt is cooled rapidly enough to avoid crystallization. Then, it undergoes a glass transition at T_g. For slower cooling the melt transforms into a semicrystalline material at the crystallization temperature T_{crys}. In the semicrystalline state, sections of folded chains order in lamellar sheets that coexist with amorphous regions. On heating (dashed grey line) the crystal melts at $T_m > T_{crys}$. This hysteresis is characteristic of first-order phase transitions. The volume–temperature diagram shown is a result of molecular dynamics simulations for a model of poly(vinyl alcohol) (courtesy of H Meyer; see [10, 11] for further details).

greatly slow down the chain dynamics and render the melt in general very viscous compared to low molecular weight liquids.

Polymeric solids: crystallization and glass transition. Polymeric solids are either glassy or semicrystalline (figure 1) [12]. Semicrystalline polymers contain both amorphous and crystalline regions. The crystalline regions consist of lamellar sheets in which the polymers are folded back and forth so that sections of chains can align parallel to each other. The sheets twist and branch as they grow outward from a nucleus into spherulitic structures [12]. This hierarchy of morphological features, ranging from the lamellar ordering of the chains (~10 nm) to the macroscopic packing of the spherulites (100 μm and larger), reflects the complexity of the underlying crystallization process which is not yet fully understood [13–16].

The ability to form crystal crucially depends on the microstructure of the chains. Only polymers with regular configurations, e.g. isotatic or syndiotatic orientations of the sidegroups [3] or chains without sidegroups, polyethylene being the prime example, can align parallel to each other so as to pack into crystalline lamellae. However, even in these favourable cases full crystallization is almost never achieved (see e.g. [14]).

Due to this intrinsic difficulty of crystal formation, polymer melts are in general good glass formers [17–19]. Either they can be readily supercooled (figure 1) or, due to the irregular configuration of the chains, a crystalline phase does not exist at all. There are numerous examples for the latter case. They comprise homopolymers with an atactic orientation of (bulky) sidegroups, e.g. atactic polystyrene, or random copolymers, such as *cis–trans* polybutadiene, in which monomers, having the same chemical composition, but different microstructures (*cis–trans* configuration of butadiene), are randomly concatenated. These polymeric glass formers exhibit features that are also prevalent in other (intermediate and fragile) glass-forming liquids [18, 19]. For instance, as the melt is cooled from the liquid state toward the glass transition temperature T_g, it displays a non-Arrhenius increase of all measured structural relaxation times. In proportion to this huge effect on the dynamics, the amorphous structure of the melt only changes very little on cooling. This discrepancy poses a formidable scientific problem. Understanding its molecular origin represents an important issue in the research on the glass transition [19–22].

Scope of the article. The present article reviews recent simulation results for glass-forming polymer melts. Even within this scope there are several respects in which our discussion will be limited. We adopt the view that the glass transition is approached by slow cooling from the liquid. 'Slow cooling' means that the melt is always in thermal equilibrium. This condition restricts our attention to temperatures above the critical glass temperature T_c of mode-coupling theory (MCT) [21–24]. Thus, we do not discuss interesting sub-T_g phenomena, such as physical ageing [17, 18] (see also [25] for a topical review) or the response of polymeric glasses to external deformation fields [26, 27]. Furthermore, our survey will be mainly concerned with molecular dynamics (MD) studies of a bead–spring model of a polymer melt. This model—a representative of the class of coarse grained generic simulation models [28]—may be considered as an archetypal model for polymer solutions and melts [29, 30]. Work on realistic polymer models will only be touched upon briefly in comparison to the results presented here. Comprehensive reports of these realistic modelling approaches may be found e.g. in [31, 32]. Finally, our discussion, which represents an update on results reviewed in [33, 34], has surely devoted disproportionately much space to our own contributions. This is mainly because we hope to explain them best.

Outline. We have chosen to organize our survey as follows. We begin (section 2) by compiling some information on polymer modelling and technical aspects of the simulation. In particular, we introduce the coarse grained model that will mainly be discussed in the next two sections: one devoted to the features of the bulk (section 3), the other to those of thin films (section 4).

In section 3, our discussion will revolve around two aspects, a comparison of the simulation results with MCT (section 3.3) and an analysis of dynamic heterogeneities emerging in the cold melt above T_c (section 3.4). We explain how the analyses are carried out and what results may be obtained from them, and we assess their strengths and weaknesses as we go. Especially for mode-coupling theory, there are some technical details of the quantitative analysis which are not essential for the logic of the text but may be beneficial if one wants to apply the theory. Accordingly they are addressed separately, in appendix A.

There is another approach to the properties of glass-forming liquids, based on the features of the potential energy landscape. This approach is extensively pursued in simulation studies at present, and we felt that it should be included somewhere in this article, although it was not applied to our polymer model. Appendix B provides a brief introduction.

The second part of this review deals with the extension of the simulations from the bulk to thin polymer films. Section 4 identifies and explores what appears to be an important issue here—the influence of the boundary condition, imposed by the confining walls, on the structural (section 4.2) and dynamic properties (section 4.3) of the melt. Geometric confinement is generically found to shift T_g (or T_c in our case) relative to that of the bulk. We compare our and other simulation results for the T_g shift with experimental data, give a brief survey of some recent theoretical ideas for explaining these shifts (section 4.3.2) and discuss related simulation work on the glass transition of confined liquids (section 4.4).

Finally, section 5 provides a synopsis of the results presented.

2. Simulation of glass-forming polymers: models and computational aspects

This section aims at providing an introduction to computer simulations of glass-forming polymer melts. Certainly, our presentation will not be exhaustive, neither as regards the modelling of polymer melts nor as regards specific computational aspects associated with glass-forming systems in general. There are, however, excellent reviews on these topics, e.g. [29, 35–38], as far as the modelling of polymer melts is concerned, or [39, 40] for problems centred around the simulation of glass-forming systems.

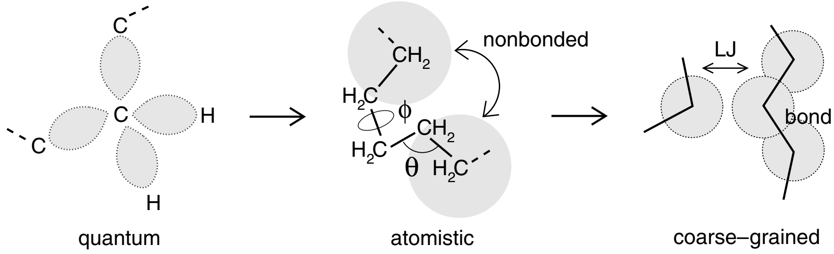

Figure 2. Schematic representation of different levels one may utilize to model polymers. The quantum level takes account of the electrons to calculate the interactions between the nuclei 'on the go'. At present, using such an approach to simulate polymer melts is computationally too demanding. Less demanding and currently feasible are simulations at the atomistic level [32]. Here, the electronic degrees of freedom are replaced by a force field. A force field is the total potential energy resulting from the interactions of all atoms ('explicit atom model') or from the interactions of spherical sites comprising several atoms (e.g. CH_2; the 'united atom model'). In the middle figure, two united atoms are indicated by the shaded circles. Typically, a force field contains contributions from bonded and nonbonded interactions. Bonded interactions comprise potentials for the bond length (nearest neighbour), the bond angle θ (second-nearest neighbour) and the torsional angle ϕ (third-nearest neighbour). Between neighbours (atoms or united atoms) that are further apart along the backbone of the chain nonbonded interactions are taken into account. For uncharged polymers they are often modelled by a Lennard-Jones (LJ) potential. Computationally still less demanding than atomistic models are simulations at the coarse grained level. Here, a monomer is associated with a spherical site and the realistic potentials are replaced by simpler ones. This simplification, if carried out systematically, can lead to coarse grained models for a specific polymer—recent approaches have been reviewed in [35, 36, 41]. Otherwise it leads to generic models, such as the model described in section 2.2.

2.1. Coarse graining: from atomistic to generic polymer models

In any material, the interaction potential results from the adaptation of the electronic degrees of freedom to the positions of the nuclei. It may thus appear natural to model polymer melts via the Car–Parrinello method [42]. This method is a molecular dynamics (MD) technique [43, 44] which allows the electrons to adiabatically follow the motion of the nuclei. It thereby replicates authentically the energy landscape that the nuclei feel at any instant of their motion. However, given the current computer power this authenticity carries a price: the inclusion of the electrons in the simulation restricts the system size to about 100 nuclei and requires a time step of $\sim 10^{-17}$ s. As typically $\sim 10^{8}$ time steps may be performed in a long run, such an *ab initio* approach could simulate a melt of 10 chains with $N = 10$ for about 1 ns. This time barely suffices to equilibrate the system at high temperature in the liquid state [38, 45].

Thus, the modelling of polymer melts nowadays still necessitates simplifications. These simplifications generally invoke some kind of coarse-graining procedure. That is, one forgoes the explicit treatment of fast degrees of freedom and incorporates them in effective potentials. There are several levels to this [32, 36, 41].

Atomistic models. The preceding discussion suggests that a compulsory simplification (at present) should consist in replacing the electronic degrees of freedom by empirical potentials for the bond lengths, the bond angles, the torsional angles and the nonbonded interactions between distant monomers along the chain ('quantum level → atomistic level'; see figure 2). This step introduces a 'force field', i.e., the form of the potentials is postulated and the corresponding parameters (e.g. equilibrium bond length, force constants) are determined from quantum chemical calculations and experiments [32, 41].

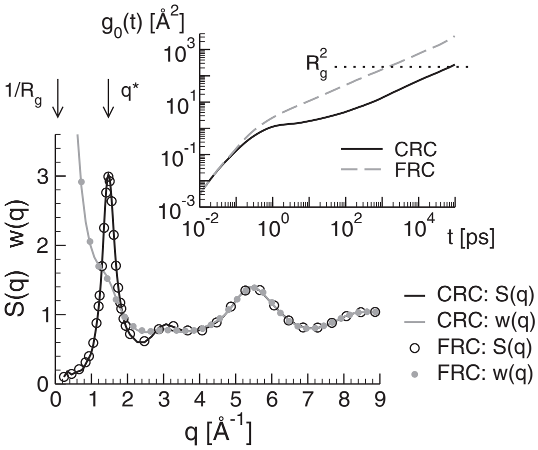

Figure 3. Simulation results for *cis–trans* 1,4-polybutadiene (adapted from [53], with permission). Main panel: collective static structure factor, $S(q)$ (see equation (11)), and single-chain structure factor, $w(q)$ (see equation (12)), versus the modulus of the wavevector $\boldsymbol{q}$ at $T = 273$ K. Two united atom models are compared: a chemically realistic model (CRC) and the same model but without torsional potential (FRC). The vertical arrows indicate the values of q associated with the radius of gyration R_g and with the first maximum of $S(q)$ ('amorphous halo'). The maximum occurs at $q^* \simeq 1.47$ Å^{-1}. In real space, this value would correspond to an intermonomer distance of ≈4.3 Å which is roughly compatible with the average Lennard-Jones diameter of the model ($\sigma \approx 3.8$ Å). Inset: mean square displacement $g_0(t)$, averaged over all monomers, versus time for the CRC and FRC models at $T = 273$ K. The horizontal dotted line indicates the radius of gyration $R_g^2 = 218$ Å^2 (which is found to be the same for the two models [54]).

Throughout the past decades several such force fields have been proposed for both explicit atom models and united atom models. An explicit atom model treats every atom present in Nature as a separate interaction site, whereas a united atom model lumps a small number of real atoms together into one site [32, 36, 41]. Typical united atoms are CH, CH_2 and CH_3. The reduction of force centres translates into the computational advantage of allowing longer simulation times. With a time step of $\sim 10^{-15}$ s—compared to $\sim 10^{-17}$ s for the Car–Parrinello method—a few thousand united atoms can be simulated over a time lapse of several 100 ns, about an order of magnitude longer than for an explicit atom simulation of comparable system size.

Both explicit atom models and united atom models have been utilized in the study of glass-forming polymers (see e.g. [31, 46] for reviews on older work). Current examples include polyisoprene (explicit atom model; [47, 48]), atactic polystyrene (united atom model; [49–51]) and *cis–trans* 1,4-polybutadiene (united and explicit atom models; [32, 52–56]). Certainly, the ultimate objective of these modelling efforts is that the simulation results lend themselves to a quantitative comparison with experiments. Such a comparison may, however, require a careful fine-tuning of the force field. For the family of neutral hydrocarbon polymers the optimization of the torsional potential appears particularly crucial. Not only the position and the relative height of the minima, but also the barriers between them should be accurately determined, as local relaxation processes, involving transitions between the minima, are exponentially sensitive to them. In extreme cases, imprecise barrier heights may seriously affect the dynamics while leaving structural features of the melt unaltered.

Such an extreme example is shown in figure 3. The figure compares simulation results for two models of a polybutadiene melt [53, 54]: a carefully validated united atom model which reproduces the experimentally found structure and dynamics of the melt, and the same model with the torsional potential switched off. Apparently, suppression of the torsional potential has no influence on the structure, but considerably accelerates the monomer dynamics.

This example demonstrates that different potentials may lead to a realistic representation of structural properties, but to diverging predictions for the dynamics. Such an observation is not limited to polymers; it was also made e.g. for amorphous SiO_2 [40]. This suggests that the design of a chemically realistic model, aiming at a parameter-free comparison between simulation and experiment, should involve information about both structural and dynamic properties.

Generic models. Atomistic simulations of carefully designed models are the best way to explore the properties of specific polymers, including the glass transition. However, the strong slowing down of the dynamics on cooling, which eventually leads to the freezing in of an amorphous state, is observed for all glass-forming polymers, irrespective of their chemical structure. If the focus is on these general features, it appears permissible to forego fast degrees of freedom (bond length and bond angle vibrations, etc) in favour of a coarse grained model ('atomistic level → coarse grained level'; see figure 2). A special type of coarse grained models is constituted by so-called 'generic models' [36]. A generic model only retains the most basic features of polymer chains. For (uncharged) linear polymers these features are presumed to be chain connectivity, excluded volume interactions and, possibly, monomer–monomer attractions and/or some stiffness along the chain backbone. Various such generic models have been studied in the literature (for reviews see [28, 38, 57]). In the following we present one of these models, which was used in our simulations [58–73], in more detail.

2.2. The Bennemann model: a bead–spring model for glass-forming polymer melts

In 1985 [74] Grest and Kremer proposed a versatile bead–spring model for the simulation of polymer systems. The 'Kremer–Grest' model has ever since been deployed to investigate numerous problems in polymer physics, including relaxation processes in polymer solutions [75] and melts [30, 76, 77], the behaviour of polymer brushes [78, 79] or rheological properties of complex fluids [29], just to name a few. These diverse successful applications prompted Bennemann *et al* [58] to suggest a variant of the model for the study of glass-forming polymer melts.

The Bennemann model. In this model, the chains contain N identical monomers of mass m. All monomers, bonded and nonbonded ones, interact through a truncated and shifted Lennard-Jones (LJ) potential

$$U_{\mathrm{LJ}}^{\mathrm{ts}}(r) = \begin{cases} 4\epsilon[(\sigma/r)^{12} - (\sigma/r)^{6}] + C(r_{\mathrm{cut}}) & \text{for } r \leqslant r_{\mathrm{cut}}, \\ 0 & \text{else.} \end{cases} \tag{1}$$

The parameter $C(r_{\mathrm{cut}}) = 127/4096\,\epsilon$ shifts the potential to zero at the cut-off distance $r_{\mathrm{cut}} = 2r_{\mathrm{min}}$ where $r_{\mathrm{min}} = 2^{1/6}\sigma$ is the minimum of equation (1). The choice for r_{cut} is motivated by the wish to work with a potential that is as short ranged as possible[3] while still including the major part of the attractive van der Waals interaction. Even though attractive

---

[3] Computational expediency suggests working with a short range potential because the number of neighbours n_{i} with which a particle interacts scales with the cut-off distance as $n_{\mathrm{i}} \propto r_{\mathrm{cut}}^3$ [84, 85]. So one expects a simulation of the Kremer–Grest model, where $r_{\mathrm{cut}} = 2^{1/6}$, to be about eight times faster than that of the Bennemann model ($r_{\mathrm{cut}} = 2 \times 2^{1/6} \approx 2.25$). In fact, our experience confirms this expectation (the speed-up factor for the Kremer–Grest model is rather 5 than 8). This computational advantage was presumably one of the motivations for using the Kremer–Grest model also to study supercooled polymer melts [338]. (In this case, however, the glass transition temperature appears to be distinctly smaller than in the Bennemann model, which outweighs the speed-up factor mentioned above.) On the other hand, the cut-off distance of the Bennemann model is of course not necessarily the only possible choice. The slightly larger (classical [84, 85]) value $r_{\mathrm{cut}} = 2.5$ was used e.g. in [99, 121].

interactions are not expected to appreciably affect the local structure in a dense melt[4], they may have a significant effect on thermodynamic properties. Furthermore, they are important for simulations of e.g. the phase behaviour of polymer solutions [80, 81], thin films with a film–air interface [82, 83] and crazing in polymer glasses [26, 27]. The idea of Bennemann *et al* was to suggest a model which could be employed to explore various physical situations without the need to be modified.

In addition to the LJ potential, nearest neighbour monomers along the chain interact through a FENE (finitely extendible nonlinear elastic) potential[5]

$$U_{\mathrm{FENE}}(r) = -\frac{1}{2}kR_0^2\ln\left[1-\left(\frac{r}{R_0}\right)^2\right], \qquad R_0 = 1.5\sigma, \quad k = \frac{30\epsilon}{\sigma^2}. \tag{2}$$

Equation (2) diverges logarithmically if $r \to R_0$ ('finite extensibility') and vanishes parabolically close to the origin ('elastic behaviour'). So the FENE potential alone does not prevent monomers from overlapping. Local excluded volume is imposed by the LJ interaction. The superposition of the FENE and the LJ potentials yields a steep effective bond potential with a minimum at $r_{\mathrm{b}} = 0.9606$ (see e.g. [71]).

Lennard-Jones units and approximate mapping to real units. The parameters of equation (1) define the characteristic scales of the melt: ϵ the energy scale, σ the length scale and $\tau_{\mathrm{LJ}} = (m\sigma^2/\epsilon)^{1/2}$ the timescale. In the following, we utilize LJ units. That is, $\epsilon = 1$, $\sigma = 1$ and $m = 1$. Furthermore, temperature is measured in units of ϵ/k_{B} with the Boltzmann constant $k_{\mathrm{B}} = 1$.

Although reduced units are commonly employed in simulations and are of technical advantage [84, 85], it might still be interesting to obtain a feeling for how they translate into physical units. Such a mapping of the Bennemann model to real systems has recently been carried out by Virnau *et al* [81, 86] and by Paul and Smith [32]. Virnau *et al* explored the phase separation kinetics of a mixture of hexadecane ($C_{16}H_{34}$) and carbon dioxide (CO_2). By identifying the critical point of the liquid–gas transition in hexadecane with that of bead–spring chains containing five monomers they found $\sigma \simeq 4.5 \times 10^{-10}$ m and $\epsilon \simeq 5.8 \times 10^{-21}$J. Paul and Smith compared the dynamics of chemically realistic models for nonentangled melts of polyethylene and polybutadiene with that of the Bennemann model. This comparison allowed them to convert τ_{LJ} to seconds. The result is $\tau_{\mathrm{LJ}} \simeq 2.1 \times 10^{-11}$s. These values for σ, ϵ and τ_{LJ} are compatible with the estimates obtained by Kremer and Grest when comparing the dynamics of entangled bead–spring melts to those of real polymers (see table III of [74]; see also section 4.7 of [29] for further discussion).

Choice of the chain length. In polymer glass simulations the chain length N is usually chosen as a compromise between two opposing wishes: on the one hand, N should be sufficiently large to separate the scales of the monomer and the chain size so that polymer-specific effects (or at least the onset thereof) become observable. On the other hand, computational expedience suggests working with short chains. Because the simulations aim at following the increase of the monomeric relaxation time τ_0 with decreasing temperature over as many decades as possible, slow relaxation processes, already present at high T due to entanglements, should

---

[4] In glass-forming colloidal suspensions, however, attractions of quite short range and moderate-to-high strength may influence the local packing. Depending on the external control parameters this can increase the density where the glass transition occurs, or lead to gelation phenomena [364–366].

[5] According to [74], the values given in equation (2) for R_0 and k prevent the bonds from crossing each other in the course of the simulation. This imposes topological constraints [2] which ultimately lead to reptation-like dynamics in the limit of large chain length [74, 77].

be avoided. Thus, the chain length should be smaller (or at least not much larger) than the entanglement length N_{e}. Extensive studies of the Kremer–Grest model show that $N_{\mathrm{e}} \approx 32$.[6] Shorter chains exhibit Rouse-like dynamics:

$$\tau_N = \tau_0 N^{\approx 2}. \tag{3}$$

As the Bennemann model is expected to have a similar N_{e}, the chain length $N = 10$ was proposed as a possible compromise [58]. This chain length was used in all subsequent studies pertaining to glass-forming polymer melts [58–73].

2.3. Extending the model to thin films: smooth and rough walls

A 'polymer film' is a system in which a polymer melt is geometrically confined in one spatial direction. The confinement can result from two polymer–air interfaces ('freely standing films'), from two inequivalent interfaces (e.g. polymer–air and polymer–substrate) or from enclosing the melt between two substrates. It is the latter situation that we will be mainly concerned with here.

Even though real substrates can have a complex structure, it appears natural in the spirit of the polymer models discussed above to treat the substrate also at a generic level. One obvious feature is its impenetrability. So a minimal model must at least respect monomer–substrate excluded volume interactions. Further generic features could be some surface roughness and adhesive power. On the basis of this reasoning, simulations often model the substrate as a crystal [87, 88] made of particles that interact with each other and with the monomers through LJ potentials. If we adopt that model, two limiting cases may be distinguished:

(i) *Smooth and structureless walls.* The presence of the substrate leads us naturally to consider two directions: the direction parallel to the wall ($\boldsymbol{s} = (x, y)$) and the z direction perpendicular to it (figure 4). So the interaction potential between the monomers and the substrate is in general a function $U_{\mathrm{w}}(\boldsymbol{r}) = U_{\mathrm{w}}(\boldsymbol{s}, z)$. If our interest is restricted to the average potential which the substrate exerts on a monomer, we may treat the wall as a continuum and integrate over the parallel (x, y) directions and the vertical direction up to position z. Carrying out this calculation for the LJ potential yields

$$U_{\mathrm{w}}(z) = \epsilon_{\mathrm{w}}\left[\left(\frac{\sigma}{z}\right)^9 - f_{\mathrm{w}}\left(\frac{\sigma}{z}\right)^3\right], \tag{4}$$

where ϵ_{w} denotes the monomer–wall interaction energy and f_{w} is a constant. While the second attractive term is important if one wants to study polymer adsorption [89] or wetting phenomena [90, 91], the first term of equation (4) suffices for imposing a geometric confinement. This is the stance we adopted in most of the simulations on supercooled polymer films [68–71, 73]: By choosing $\epsilon_{\mathrm{w}} = \epsilon$ and $f_{\mathrm{w}} = 0$ we introduce two smooth, structureless and completely repulsive walls in the z direction. The walls are a distance h apart (figure 4). We refer to h as the 'film thickness'. In equation (4), the distance coordinate is thus given by $z = |z_{\mathrm{monomer}} - z_{\mathrm{smooth\,wall}}|$ with $z_{\mathrm{smooth\,wall}} = \pm h/2$, where z_{monomer} is the coordinate of the monomer perpendicular to the wall.

(ii) *Rough and crystalline walls.* Rough walls may be implemented by restoring the first crystalline layer. To this end, we chose [72] to tether the wall atoms to the sites of a triangular lattice with harmonic springs (the 'Tomlinson model' [92]):

$$U_{\mathrm{T}}(\boldsymbol{r}) = \tfrac{1}{2}k_{\mathrm{T}}(\boldsymbol{r} - \boldsymbol{r}_{\mathrm{eq}})^2, \qquad k_{\mathrm{T}} = 100. \tag{5}$$

---

[6] The estimate $N_{\mathrm{e}} \approx 32$ results from an analysis of monomer mean square displacements [74, 77]. Another estimate that is about twice as large may be derived from rheological data [77, 367, 368].

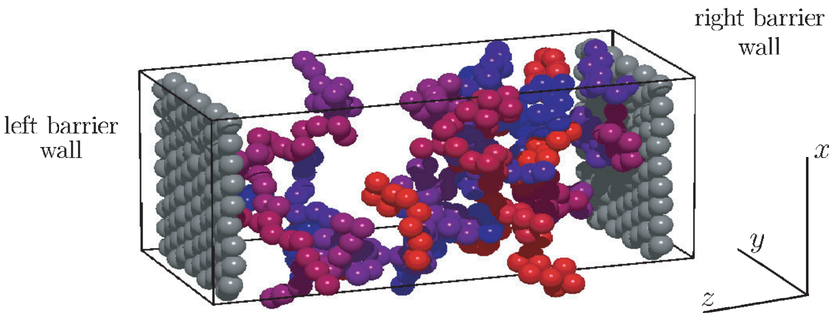

Figure 4. Snapshot of a polymer film between rough walls (only 40 chains out of 200, containing $N = 10$ monomers each, are shown). The walls consist of two parts: a layer of atoms tied to a triangular lattice via equation (5) and a barrier modelled by the repulsive part of equation (4). The barrier is indicated by solid lines on the opposite faces of the simulation box in the z direction. In the lateral (x, y) directions, periodic boundary conditions are employed [84, 85]. The system size in these directions is $L_x = L_y = 10.05$, while the distance between the triangular lattice planes is $h = 20$.[9] The barrier walls are placed at $z_{\text{smooth wall}} = \pm(1 + h/2)$. In the case of a film confined between smooth walls the crystalline layers are absent and the barrier walls are placed at $z_{\text{smooth wall}} = \pm h/2$. This figure is taken from [72].

(This figure is in colour only in the electronic version)

Here, $\boldsymbol{r}_{\text{eq}}$ denotes the equilibrium position of an atom on the triangular lattice and k_{T} the spring constant[7]. The wall atoms are LJ particles that interact with each other and with the monomers. The parameters (ϵ and σ) for these interactions—wall–wall and monomer–wall—are the same as in equation (1). We expect this choice to lead to a 'stick boundary condition'[8].

---

[7] The value $k_{\text{T}} = 100$ is close to the force constant corresponding to the harmonic approximation of the LJ force in an fcc lattice. This choice was motivated by a study of the pressure tensor in simple liquids [369]. On the other hand, the Tomlinson model (equation (5)) appears to have an unrealistic feature. It allows a wall atom to vibrate, to some extent, independently around its equilibrium position $\boldsymbol{r}_{\text{eq}}$. For instance, an up–down motion is possible without perturbing the neighbours. In reality, one might, however, expect a compression at some position to also cause an indentation in the local environment. So, displacements of neighbouring particles should be correlated. These correlations may be taken into account in the so-called Frenkel–Kontorova–Tomlinson model [92]. However, it is not clear whether these correlations are of crucial importance or not. For instance, reasonable results for the viscous flow of a polymer melt can be obtained both with the Tomlinson model alone [370] and with the Tomlinson model supplemented with excluded volume interactions between the wall atoms [72].

[8] This expectation is motivated by the experience we gained from nonequilibrium MD simulations of shear flow in a polymer melt (Bennemann model) [72] and in a binary LJ mixture (Kob–Andersen mixture) [371]. In [72], partial slip at the crystalline wall was found at the monomer density $\rho_{\text{m}} = 0.795$ when the LJ parameters of the monomer–wall interaction were the same as in the bulk (i.e., $\sigma_{\text{mw}} = 1$ and $\epsilon_{\text{mw}} = 1$). To realize a 'stick boundary condition' at $\rho_{\text{m}} = 0.795$ we took $\sigma_{\text{mw}} \approx 0.89$ and $\epsilon_{\text{mw}} = 2$. As $\sigma_{\text{mw}} < \sigma$ and $\epsilon_{\text{mw}} > \epsilon$, the monomers can approach the wall more closely than they could approach each other and they are attracted by the wall more strongly than they would attract each other in the bulk. The combination of the two effects enhances the ability of the polymer melt to adapt to the wall structure, and this leads to the 'stick boundary condition' [327, 370] (see also [93] for further details). A similar adaptation to the wall structure should also be attainable for $\sigma_{\text{mw}} = 1$ and $\epsilon_{\text{mw}} = 1$ when the monomer density is high (i.e., $\rho_{\text{m}} \simeq 1$). This is the case for the simulations discussed in section 4.3.3.

[9] The simulation box for this (large) film thickness is not symmetric; we have $h/L_x \simeq 2$. We explored the influence of this asymmetry on the features of the films and ascertained that it is negligible—for both static and dynamic properties—if h/L_x is not much larger than 2 [93]. Otherwise, there may be important finite size effects. For smooth walls we found that the dynamics is accelerated in smaller systems, that is, in systems with $h/L_x \gg 2$. This result is contrary to what has been observed in bulk simulations of e.g. LJ mixtures [208, 333], soft sphere mixtures [334] and a model of silica [335, 336]. In the bulk, the dynamics (in the supercooled state) slows down with decreasing system size. Certainly, more work has to be done to understand these asymmetry and finite size effects better.

A monomer interacts not only with the first crystalline layer, but also with all deeper layers of the wall. We represent this interaction with the repulsive part of equation (4). In equation (4), the distance coordinate is now given by $z = |z_{\text{monomer}} - z_{\text{smooth wall}}|$. Here, $z_{\text{smooth wall}} = \pm(1 + h/2)$; h denotes the distance between the crystalline layers on the left and right sides of the system. The presence of this smooth wall behind the crystalline layer has the extra benefit of supplying a barrier that renders the wall impenetrable (see [72, 93] for further discussion).

Smooth or rough walls, of the types we have just discussed, are commonly employed in simulations of confined liquids. These walls affect the local structure of the liquid in their vicinity (cf section 4.2.1 and the end of section 4.3.3). If these perturbations should be avoided, at least to a large extent, one has to adapt the structure of the walls to that of the bulk liquid. A cunning way of tackling this problem consists in 'building' the walls from bulk simulations [94]: first, a bulk liquid is equilibrated at a specific thermodynamic state point; then, 'amorphous' walls are introduced by 'freezing' all particles outside of a volume of a given geometry. Here, we are in principle at liberty to choose whatever geometry we like—spherical, cylindrical, film etc. For simple liquids this procedure has an additional advantage. Since the walls are inscribed in a previously equilibrated system, no further equilibration is needed after their introduction [94]. For polymer melts, however, the situation can be more complicated, due to chain connectivity. When freezing a portion of the melt we cannot prevent some chains from participating in both the wall and fluid parts of the system. If a clear separation of the two parts is desired, these chains must be 'removed'; and this will in general require further equilibration.

To construct such amorphous walls for polymer films we proceeded in the following way:

(iii) *Rough and amorphous walls.* We begin by generating an equilibrated configuration of the bulk polymer melt at the desired thermodynamic state point. Then, we freeze all monomers in two slices each having a thickness of three monomer diameters, one slice at the edge of the simulation box and the other in the middle of the box. This choice appears appropriate if one wants to construct walls whose structures are independent of each other (if we utilized for the second wall e.g. the opposite edge of the simulation box, a correlation between the walls would exist due to the periodic boundary conditions). After this assignment of monomers to the walls there will be chains that have monomers inside and outside of the slices; we now remove all monomers outside of the slices. This provides us with two amorphous walls which are then inserted in place of the two smooth walls—i.e., at $\pm h/2$—in a previously equilibrated polymer film being confined by the structureless walls described in point (i). (Additionally, as for the crystalline walls, a smooth barrier wall is inserted at $z_{\text{smooth wall}} = \pm(3 + h/2)$.) Finally, the resulting configuration is equilibrated.

One may think (or hope) that these amorphous walls would allow one to avoid the above-mentioned structural changes due to confinement. Unfortunately, the present procedure does not fully accomplish this goal (as we will see at the end of section 4.3.3). For example, density oscillations are still observed; their amplitude, however, is much weaker than that found near the crystalline walls.

2.4. Remarks on the simulation methodology

Imposing constant temperature and pressure. Molecular dynamics (MD) simulations constitute a numerical scheme which integrates the classical equations of motion associated with a many-body potential. Therefore, the natural thermodynamic ensemble of MD is the microcanonical NVE ensemble. (Here, N denotes the total number of particles, V the volume of the system and E its total energy.) In many situations, it is however desirable to switch to another ensemble. For instance, experiments are typically carried out at constant temperature T and constant pressure p. This implies that the equations of motion must be modified to allow for fluctuations of both E and V in response to the fixed temperature and pressure.

Several efficient techniques have been developed to achieve this [84, 85]. The work of [58–73] on which we will mainly focus in the following utilizes the Nosé–Hoover thermostat [85, 95] and the Andersen–Hoover barostat [96, 97] (see [58, 65, 93] for more details). Numerical evidence obtained from the Bennemann model in the bulk [58] and in thin films [70] as well as theoretical arguments [98] demonstrate that simulations in the canonical NVT ensemble using the Nosé–Hoover thermostat replicate the classical microcanonical dynamics provided that the system size is large enough (total number of monomers larger than a few hundred). By contrast, addition of the Andersen–Hoover barostat seems to engender large volume fluctuations, particularly at low T [65] and for small film thicknesses [70], which strongly perturb the relaxation dynamics of the melt. Therefore, the MD simulations were performed in two steps: in a first step, the average volume corresponding to a prescribed external pressure p (mainly $p = 1$) is determined; the second step fixes this volume and continues the simulation in the canonical ensemble using the Nosé–Hoover thermostat only. A similar procedure was also chosen in the recent work by Barbieri *et al* [99].

There is one further technical point about constant-pressure simulations which we want to address now [68, 69]. In the bulk, the pressure is a scalar. In an inhomogeneous system, however, it depends on the spatial direction and the position $\boldsymbol{r}$ where it is determined. Quite generally, the pressure is thus a tensor function $\mathbf{P}(\boldsymbol{r})$ [100–102]. For a film in equilibrium we can further specify this function. Exploiting the property that the film is isotropic in the lateral x and y directions and using the condition of mechanical stability for a fluid at equilibrium, one finds that only the diagonal elements of $\mathbf{P}$ are nonzero and given by [68, 100, 101]

$$P_{xx}(z) = P_{yy}(z) = P_{\mathrm{T}}(z) \qquad \text{and} \qquad P_{zz}(z) = P_{\mathrm{N}} = \text{constant}. \tag{6}$$

The fact that the pressure profile is constant across the film suggests a simulation method which equates P_{N} to an imposed external pressure $P_{\mathrm{N,ext}} = p$. This mimics experiments on thin films which are usually carried out at constant normal pressure. If P_{N} is fixed, the thermodynamically conjugate variable, the film thickness h, should fluctuate. However, experiments also reveal that the (average) film thickness increases by only a few per cent on heating the film above its glass transition temperature [103, 104]. As our interest is mainly in the behaviour of our model at low T, this experimental finding suggests fixing both P_{N} and h in the simulation. Contrary to the bulk case, such a constraint can be realized for the film. Imposing the film thickness still allows the surface area A of the system to vary, and so the volume $V = hA$ is a fluctuating quantity. Details on how to implement this algorithm may be found in [69].

Molecular dynamics versus Monte Carlo. In the framework of computer simulations it appears natural to address dynamical problems via MD techniques. However, if we are interested in equilibrating long chain glass-forming polymer melts at low T, MD does not necessarily lend itself to addressing this problem efficiently. The realistic MD dynamics carries the price that the equilibration time can exceed the maximum time of a few hundred nanoseconds that one is currently able to simulate.

At that point, one might envisage resorting to Monte Carlo (MC) techniques [105]. The strategic advantage offered by this method is the range of ways in which MC moves may be designed to explore configuration space. The hope is to find an algorithm that, freed of the need to capture the real dynamics, efficiently decorrelates the configurations of glass-forming polymer melts at low T.

This demand on the algorithm appears to exclude as a possible candidate the simplest MC technique, the application of local MC moves. A local MC move consists in selecting a monomer at random and in attempting to displace it by a small amount in a randomly chosen direction [28]. Not only should the local character of coordinate updating share the essential problematic features of the (local) MD dynamics at low T, but also one may expect that local MC moves will yield an unfavourably large prefactor for the relaxation time due to their stochastic character. This conjecture is based on an observation made by Gleim *et al* [106]. Gleim *et al* compared the relaxation dynamics of a glass-forming binary mixture simulated, on the one hand, by MD and, on the other hand, by a stochastic (Brownian) dynamics (which is in some respects similar to MC). They demonstrated that, although the structural relaxations at long times are the same for the two methods, MD is roughly an order of magnitude faster than the stochastic dynamics. These findings are supported by the recent work of Voigtmann *et al* [107].

However, MC moves need not be local. They can be tailored to alter large portions of a chain. A prominent example of such nonlocal moves is the configurational bias Monte Carlo (CBMC) technique [28, 85]. Application of this technique to dense polymer systems in the canonical ensemble usually involves an attempt to remove a portion of a chain starting from one of its monomers that is randomly chosen, and to regrow the removed portion subject to the constraints imposed by the local potential energy. If successful, this should imply a large modification of the chain configuration, thereby promising efficient equilibration. However, Bennemann *et al* found that even in the limit where only the end is reconstructed (‘smart reptation’), CBMC is inferior to ordinary MD [58]. In a dense melt, the probability of inserting a monomer becomes vanishingly small everywhere except at the position where it was removed. So, the old configuration of the chain is just restored. This trapping of the chain makes the relaxation become very slow.

Thus, successful nonlocal chain updates in dense systems should involve moves that do not require empty space. Promising candidates are double-bridging algorithms which were successfully employed in simulations of polyethylene chains [108, 109], of the Kremer–Grest model [110] and of a lattice model, the bond fluctuation model [28]. The basic idea of the algorithm is to find pairs of neighbouring chains which one can decompose into two halves and reconnect in a way that preserves the monodispersity of the polymers. Such a connectivity-altering move drastically modifies the conformation of the two chains involved and thus strongly reduces the dynamic slowing down related to chain length. However, if we attempt to repeat this move over and over again on the melt configuration we started with, a successful double-bridging event is likely to annihilate one of its predecessors by performing the transition between two chains in the reverse direction. To avoid this inefficiency the nonlocal chain updating should be complemented by a move which efficiently mixes up the local structure of the melt. At low T, efficient relaxation of the liquid structure calls for a method which alleviates the glassy slowing down in general. Thus, any algorithm achieving this aim in nonpolymeric liquids should also accelerate the equilibration of glassy polymer melts, provided that it can be generalized to respect chain connectivity. At present, no technique has been established to solve this problem (see [111] for a topical review). However, possible candidates appear to be ‘parallel tempering’ [112, 113] (see however [114]) or a recently proposed variant of ‘Wang–Landau sampling’ [115].

3. Structure and structural relaxation in the bulk

3.1. Vitrification versus crystallization

The Bennemann model (see section 2.2) implements two features which effectively eliminate the risk of crystallization: first, the bond and the LJ potentials introduce two mutually incompatible length scales, $r_b \neq r_{\min}$ (equations (1) and (2)). This implies that the bond potential locally distorts possible crystalline arrangements of the monomers (fcc or bcc), which the LJ potential alone would impose (see figure 2). Second, the chains are very flexible. Backfolding of adjacent bonds is only suppressed by the repulsive part of the LJ potential, and not by some additional potential for the bond angle.

The latter feature is indeed crucial. If the model were supplemented by a bending potential favouring large bond angles, crystallization on cooling from the melt would occur, despite the incompatibility of r_b and $r_{\min}$. This was demonstrated by extensive MD simulations of a semiflexible bead–spring model [10, 11, 116]. These studies show that short chains (with e.g. $N = 10$) form extended-chain crystals in which the chains align parallel to each other.

We can set up such a crystalline state also for the Bennemann model [65]. A configuration in which all chains are perfectly stretched out along the z direction and the monomers are placed on a tetragonal Bravais lattice corresponds to a high density state that may be further optimized by energy minimization. As the resulting structure has almost identical linear dimensions in all three spatial directions, a cubic simulation cell was chosen to explore the melting of this ‘perfect’ crystal [65]. The study of [65] gives a melting temperature of $T_m \approx 0.76$. The results should be treated with care due to the constraints imposed by the periodic boundary conditions and by the cubic shape of the (small) system. On the basis of the experience gained from the above-mentioned semiflexible bead–spring model one estimates that such a procedure may overrate T_m considerably [117]. Very roughly we expect $0.65 \lesssim T_m \lesssim 0.76$. In the following, we will be concerned with the temperature interval $0.45 < T \leqslant 1$. In this interval, no crystallization was observed upon cooling the melt quasistatically from high T toward the critical temperature T_c of mode-coupling theory ($T_c \simeq 0.45$; see sections 3.2 and 3.3). Thus, the Bennemann model is well suited for exploring the properties of an amorphous polymer melt in the supercooled state.

Remark on the term ‘supercooled state’. Within the framework of first-order phase transitions a ‘supercooled state’ is defined as the region between the binodal and the spinodal lines in the phase diagram. There, the system is in ‘metastable equilibrium’: it is in a long lived state protected by a free energy barrier against transformation into the ordered phase. For the Bennemann model this barrier is essentially infinite. The model preserves a fully equilibrated amorphous structure on cooling through the region of the putative melting temperature. It shares this property with real polymeric glass formers, such as atactic polymers, and with other computational models for simple glass formers[10]. These examples suggest that metastability with respect to a crystalline phase is not a *conditio sine qua non* for the emergence of glassy

---

[10] Different choices as regards avoiding crystallization in simple fluids have been deployed. A commonly used approach involves binary mixtures. Here, an extensively studied system is the binary mixture of Lennard-Jones particles introduced by Kob and Andersen [155, 168]. In this system, crystallization is kinetically strongly suppressed by a careful choice of the LJ parameters. However, a crystalline ground state has recently been discovered [372]. An alternative to using binary mixtures is using monatomic systems with specifically tailored interactions. Examples include the Dzugutov model [373, 374], a single-component simple liquid with an interaction potential preventing crystallization via the formation of local icosahedral structures, and Lennard-Jones systems supplemented with a perturbation that depends on the static structure factor [354, 375], and polydisperse hard sphere-like systems [107, 157, 219].

behaviour, and the classical definition of a ‘supercooled state’ should not be applied literally. In our context, we refer to the melt as ‘supercooled’ if the temperature is so low that the slow relaxation processes which ultimately lead to the glass transition of the melt can be observed (see also [23, 40] for further discussion of this point). For the Bennemann model this implies $T \lesssim 0.7 \approx T_{\mathrm{m}}$ (see e.g. figure 8 in section 3.3). Note, however, that there are systems, such as amorphous silica [118], in which the slow relaxation characteristic of the supercooled state is already fully developed above T_{m} (in particular, $T_{\mathrm{c}} > T_{\mathrm{m}}$ for silica).

3.2. Static properties: structure factors and PRISM theory

In the supercooled state the monomer number density ρ_{m} of the melt varies between $\rho_{\mathrm{m}}(T = 0.7) = 0.91$ and $\rho_{\mathrm{m}}(T = 0.46) = 1.04$ [58]. A density of order 1 implies that there is no free space for motion. This implies that, if all except one of the monomers were frozen, that monomer could only vibrate around its initial position. Any displacement over larger distances thus requires cooperative rearrangements of many monomers, that is, spatio-temporal fluctuations of the density about the average value ρ_{m}. These dynamic features will be addressed in section 3.3. Here, we want to focus on their static counterparts.

Structure factors of the melt and the chains. Density fluctuations for the wavevector $\boldsymbol{q}$ can be measured using static structure factors [119]. For a polymeric liquid it is natural to distinguish between the structure factor of a chain and that of the melt.

To introduce these quantities we consider a system containing n monodisperse chains of length N in a volume V. The chain density ρ and the monomer density ρ_{m} are then given by

$$\rho = \frac{n}{V}, \qquad \rho_{\mathrm{m}} = \frac{nN}{V}. \tag{7}$$

Now let $S_{ab}(q)$ denote the collective static structure factor of two monomers a and b $(a, b = 1, \ldots, N)$. We write $S_{ab}(q)$ as a sum of an intrachain and an interchain part:

$$S_{ab}(q) = w_{ab}(q) + \rho h_{ab}(q) \qquad (q = |\boldsymbol{q}|). \tag{8}$$

The intrachain part is given by

$$w_{ab}(q) = \frac{1}{n}\left\langle \sum_{i=1}^{n} \exp[-\mathrm{i}\boldsymbol{q}\cdot(\boldsymbol{r}_i^a - \boldsymbol{r}_i^b)] \right\rangle, \tag{9}$$

and the interchain part by

$$\rho h_{ab}(q) = \frac{1}{n}\left\langle \sum_{i\neq j}^{n} \exp[-\mathrm{i}\boldsymbol{q}\cdot(\boldsymbol{r}_i^a - \boldsymbol{r}_j^b)] \right\rangle. \tag{10}$$

In these equations $\boldsymbol{r}_i^a$ is the position of the ath monomer in the ith chain. When averaging the site-resolved quantities $w_{ab}(q)$ and $h_{ab}(q)$ over all monomer pairs (a, b) we obtain the static structure factor of the melt

$$S(q) = \frac{1}{N}\sum_{a,b=1}^{N} S_{ab}(q) = w(q) + \rho_{\mathrm{m}} h(q) \tag{11}$$

with

$$w(q) = \frac{1}{N}\sum_{a,b=1}^{N} w_{ab}(q) \qquad \text{and} \qquad h(q) = \frac{1}{N^2}\sum_{a,b=1}^{N} h_{ab}(q). \tag{12}$$

Here, $w(q)$ is static structure factor of a chain and $h(q)$ the Fourier transform of the intermolecular pair correlation function [119].

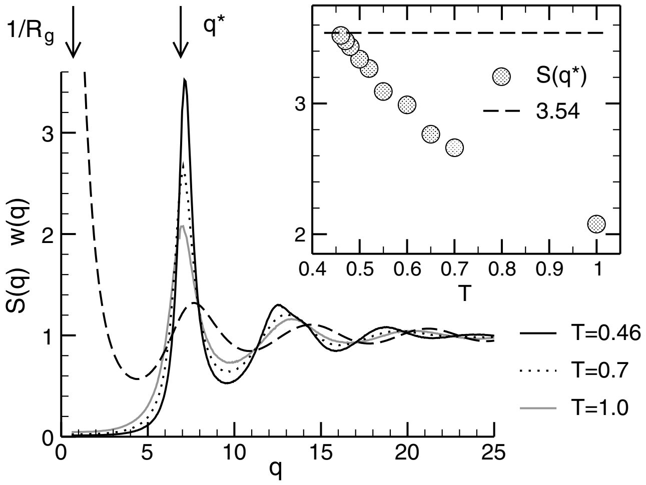

Figure 5. Main figure: static structure factor $S(q)$ of the melt (equation (11)) and intrachain structure factor $w(q)$ (equations (12) and (9)) versus the modulus of the wavevector $\boldsymbol{q}$ for the Bennemann model (section 2.2). $S(q)$ is shown for three different temperatures as indicated. Since $w(q)$ is (almost) independent of T, it is depicted only for $T = 0.46$ (dashed line). The arrows indicate the value of q corresponding to the radius of gyration ($R_g \simeq 1.45$) and the position of the amorphous halo, q^*, at $T = 1$. q^* slightly increases on cooling: $q^*(T = 1) \simeq 6.9$ and $q^*(T = 0.46) \simeq 7.15$. In real space, q^* thus corresponds to a distance of the order of the monomer diameter, in qualitative agreement with the behaviour of PB (cf figure 3). Inset: amplitude of the amorphous halo $S(q^*)$ versus T. The dashed horizontal line at 3.54 indicates the Hansen–Verlet freezing criterion for the glass transition of hard spheres [120]. ($S(q^*)$ and q^* are expected to increase slightly with chain length N; see e.g. [121].) This figure is adapted from [67].

Simulation results for $S(q)$ and $w(q)$ obtained from a chemically realistic model of *cis–trans* 1,4-polybutadiene (PB) at $T = 273$ K ($T_c \approx 216$ K [122, 123]) have already been shown in figure 3. Figure 5 presents the counterpart for the Bennemann model. Here, the temperature interval extends from the high T 'normal' liquid state of the melt ($T = 1$) to temperatures in the supercooled state slightly above the critical temperature T_c of mode-coupling theory ($T_c \simeq 0.45$; section 3.3). As also found for PB [53], we observe that the dependence of $w(q)$ on T is negligible. This demonstrates that the chains preserve a random coil-like conformation upon cooling. There is no discernible trend of incipient crystallization. The same applies to the collective structure factor. Although $S(q)$ changes with temperature, the qualitative signature expected for a disordered, dense system manifests itself in the wavevector dependence of $S(q)$. The structure factor is small at low q, reflecting the small compressibility of the melt[11]. Then, it increases with increasing q toward a maximum, the so-called 'first sharp diffraction peak' or 'amorphous halo', before it converges to 1 in an oscillatory manner as $q \to \infty$. Compared to the PB melt (cf figure 3), the Bennemann model exhibits similarities and differences. In addition to the local intrachain structure being of course different, there are qualitative disparities as regards the importance of the intrachain and interchain contributions to $S(q)$ beyond the amorphous halo. For PB, like other polymers (see e.g. [124]) and low molecular weight glass formers (see e.g. [125, 126]), the structure factor is almost entirely intramolecular, whereas both intrachain and interchain parts clearly contribute to $S(q)$ for the Bennemann model. On

---

[11] From $S(q \to 0) = k_B T \rho_m \kappa_T$, we can estimate the isothermal compressibility (κ_T) relative to the ideal gas ($1/k_B T \rho_m$). For the Bennemann model we find $k_B T \rho_m \kappa_T \sim 0.02$ in the supercooled state. This value is similar to what would be obtained for low molecular weight glass formers [376]. For polymer melts, however, one typically finds $k_B T \rho_m \kappa_T \sim 0.1$ [377].

the other hand, the Bennemann model and the chemically realistic model for PB agree with each other in that $w(q)$ is essentially independent of T. Thus, modifications of $S(q)$ with decreasing temperature must be caused by changes in the intermolecular packing. We find for the Bennemann model, and we expect for PB, that the position q^* of the amorphous halo and its amplitude $S(q^*)$ grow on cooling as a consequence of the increase of density and the attendant tighter packing of the monomers on a local scale.

We may interpret this observation in terms of an empirical freezing criterion, the Hansen–Verlet criterion [127]. According to this criterion a liquid solidifies as soon as $S(q^*)$ surmounts a critical value. For crystallization this threshold is $S(q^*) \approx 2.85$.[12] To our knowledge, no threshold value has yet been established for the glass transition. Guidance can be obtained from hard sphere systems—an appropriate model for some colloidal suspensions [128–130]—in which a glass transition occurs for volume fractions φ larger than a critical value φ_{c}. Within the framework of ideal mode-coupling theory (MCT) the glass transition of hard spheres is related to local packing constraints which become so strong at φ_{c} that the system freezes [131]. At φ_{c} MCT predicts $S(q^*) \approx 3.54$ [120].

We can compare this prediction with our simulation results. The inset of figure 5 shows that it is close to the value found for $S(q^*)$ at $T = 0.46$. This temperature in turn lies slightly above the critical temperature $T_{\mathrm{c}} \simeq 0.45$, deduced from an extensive analysis of the dynamics of the Bennemann model (cf [58–61, 63, 64] and section 3.3). The close agreement between the hard sphere results and our simulation results suggests that the criterion $S(q^*) \approx 3.54$ may be employed to approximately locate T_{c}, at least in systems in which the glass transition is driven by packing constraints resulting from the repulsive interactions between the particles [120].

Site-resolved structure factors: comparison with PRISM theory. The ‘polymer reference interaction site model’ (PRISM) has been proposed as a liquid state approach to the equilibrium properties of polymeric systems [124, 132]. The key idea of the theory is to subdivide a polymer into spherical interaction sites [133]. The sites need not coincide with the monomers of a chain. The handling of most real polymers requires one to identify an interaction site with a subgroup of a monomer (see e.g. [134, 135]). For bead–spring-like models, however, such complications do not arise [136–138]. Thus, we use ‘site’ as a synonym for ‘monomer’ in the following and we enumerate the sites from $a = 1$ to N.

Starting from the decomposition of the chains into interaction sites, PRISM theory then establishes an approximate relation between the intrachain and interchain contributions to $S_{ab}(q)$ via a generalized site–site Ornstein–Zernike equation [119, 133]

$$h_{ab}(q) = \sum_{x,y=1}^{N} w_{ax}(q) c_{xy}(q) \big[w_{yb}(q) + \rho h_{yb}(q) \big]. \tag{13}$$

Here, $w_{ab}(q)$ and $h_{ab}(q)$ are defined in equations (9) and (10), $\rho = n/V$ is the chain density and $c_{ab}(q)$ denotes the direct correlation function for the sites a and b. Qualitatively, we may interpret $c_{ab}(q)$ as the effective pair potential that two monomer densities, located on different chains, experience in the melt [124]. The direct correlation function can be expressed in terms of $w_{ab}(q)$ and $S_{ab}(q)$ by solving equation (13) for $c_{ab}(q)$. This gives

$$\rho c_{ab}(q) = \big[w_{ab}^{-1}(q) - S_{ab}^{-1}(q) \big] \qquad (a, b = 1, \ldots, N), \tag{14}$$

where $X_{ab}^{-1}(q)$ represents the (a, b) element of the inverse of the matrix $\mathbf{X}(q)$.

---

[12] For two-dimensional [378] and three-dimensional [379] colloidal suspensions in thermal equilibrium different phenomenological freezing criteria were compared and shown to yield identical results. Reference [380] extends these studies to a nonequilibrium situation. Under the influence of an external oscillatory field the freezing criteria hold as well, provided that the system is not too far from equilibrium.

The Ornstein–Zernike equation is a computationally demanding problem; it is of order N^2. The number of equations quickly becomes prohibitively large, as the chain length increases. Simplifications are thus necessary in the large N limit. However, just in this limit one would expect correlations between different chains to be only weakly affected by the presence of chain ends. This suggests taking all interaction sites as equivalent. This 'equivalent-site approximation' is usually made for the direct correlation function. That is,

$$c_{ab}(q) = c(q). \tag{15}$$

The approximation does not entail that the site dependence of the intermolecular correlations also vanishes. This can be made explicit by the following argument: we insert equation (15) into equation (13) and utilize the definition of $h(q)$ (equation (12)) to obtain the site-averaged Ornstein–Zernike equation

$$h(q) = w(q)\,c(q)\left[w(q) + \rho_{\mathrm{m}} h(q)\right]. \tag{16}$$

This result and equation (15) can then be re-inserted into equation (13), allowing us to write the site–site structure factor $S_{ab}(q)$ as

$$\begin{aligned} S_{ab}(q) &= w_{ab}(q) + \rho h_{ab}(q) \qquad \text{(see equation (8))} \\ &= w_{ab}(q) + \rho \frac{h(q)}{w(q)^2}\left[\sum_{x=1}^{N} w_{ax}(q)\right]\left[\sum_{y=1}^{N} w_{by}(q)\right]. \end{aligned} \tag{17}$$

Thus, PRISM theory predicts that the site dependence of intermolecular correlations stems entirely from the intrachain structure.

If the chain length is small, it is not clear whether equations (15) and (17) apply. Figure 6 tests the validity of the equivalent-site approximation for the Bennemann model with $N = 10$. We determined the site dependent direct correlation functions $c_{ab}(q)$ via matrix inversion of $S_{ab}(q)$ and $w_{ab}(q)$ according to equation (14). The site-averaged direct correlation function was calculated from the simulation results for $w(q)$ and $S(q)$ using

$$\rho_{\mathrm{m}} c(q) = \frac{1}{w(q)} - \frac{1}{S(q)}; \tag{18}$$

this relation follows from equations (11) and (16). The comparison of $c_{ab}(q)$ and $c(q)$ reveals that the equivalent-site approximation works well, even for decamers, unless $c_{ab}(q)$ includes a chain end ($a = 1$ or N). Then, deviations occur close to q^* and for $q \lesssim 5$. Nonetheless, the overall agreement between $c_{ab}(q)$ and $c(q)$ is good, so we can use equation (15) to interpret the intermolecular site–site correlations of our model.

This is done in figure 7. The figure compares simulation results for $S_{ab}(q)$ to the predictions of PRISM theory. We find that $S_{ab}(q)$ is well reproduced by equation (17). This demonstrates that the structural properties of the Bennemann model, even subtle monomer–monomer correlations—as well as correlations between the monomers and the centre of mass of a chain [67]—may be calculated from the average interchain direct correlation function and the fully site dependent intrachain structure factors, both of which are determined in the simulation.

3.3. Structural relaxation: comparison with mode-coupling theory

The previous section revealed that the structure of the polymer melt changes smoothly on cooling; in particular, it remains amorphous. The decrease of temperature alters the intermolecular structure—the packing becomes tighter—but has essentially no effect on the intrachain structure (cf figure 5). This state of affairs becomes very different if we turn to the

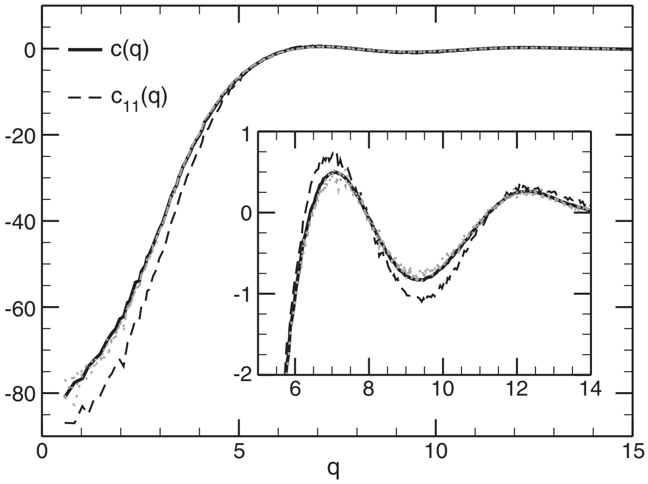

Figure 6. Test of the equivalent-site approximation (equation (15)) for the Bennemann model at $T = 0.47$. The chain length is $N = 10$. The site-averaged direct correlation function (solid line) is compared to various site dependent direct correlation functions $c_{ab}(q)$. The dashed line represents the end–end correlation $c_{11}(q)$, the dotted grey lines the autocorrelation between the monomers $a = 2, \ldots, N/2$, i.e., $c_{22}(q)$, $c_{33}(q)$, $c_{44}(q)$, $c_{55}(q)$. The inset magnifies the behaviour close to q^*. This figure is taken from [67].

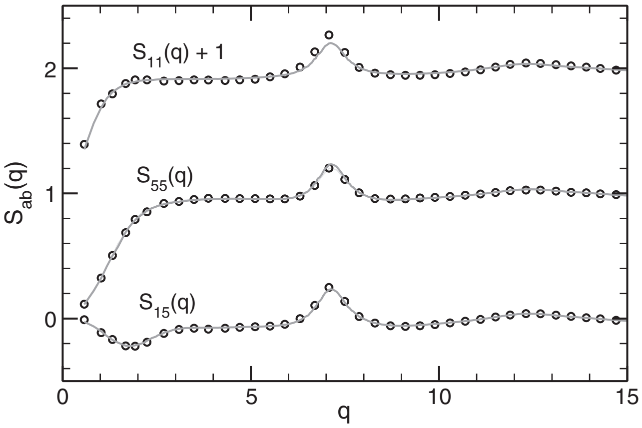

Figure 7. Comparison of the site–site static structure factor $S_{ab}(q)$ determined from the simulation at $T = 0.47$ (circles) and from PRISM theory (solid lines; equation (17)). The simulation results are obtained from the Bennemann model with $N = 10$. The end–end structure factor $S_{11}(q)$ is shifted vertically for clarity.

dynamic generalizations of the static structure factors. Both the relaxation of the chain and that of the melt undergo a strong slowing down in the same temperature interval where only weak changes of the structure occur [59, 63, 64].

As an example, we consider the coherent intermediate scattering function $\phi_q(t)$. This function is defined by

$$\phi_q(t) = \frac{1}{MS(q)}\left\langle \sum_{i=1}^{M}\sum_{j=1}^{M} \exp\{-\mathrm{i}\boldsymbol{q}\cdot[\boldsymbol{r}_i(t) - \boldsymbol{r}_j(0)]\}\right\rangle, \qquad (19)$$

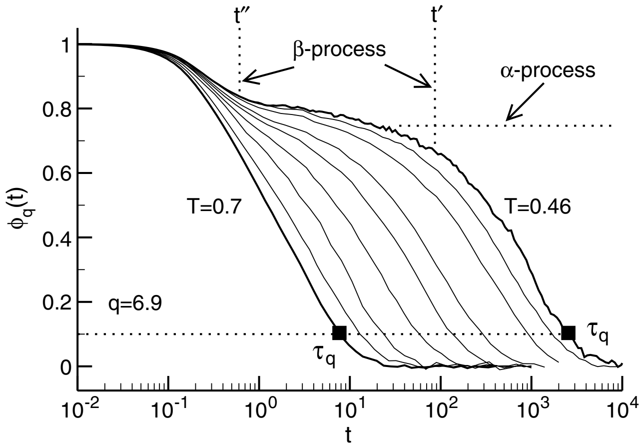

Figure 8. Coherent intermediate scattering function $\phi_q(t)$ versus time t at $q = 6.9$ ($\simeq q^* =$ maximum of $S(q)$; see figure 5). Different temperatures are shown. From left to right: $T = 0.7$, 0.65, 0.6, 0.55, 0.52, 0.5, 0.48, 0.47, 0.46 ($T_c \simeq 0.45$). For $T = 0.7$ and 0.46 the α relaxation time τ_q, defined by the condition $\phi_q(\tau_q) = 0.1$, is indicated ('■'). For $T = 0.46$ the (approximate) time intervals where the MCT β and α processes occur are shown. This figure is adapted from [63, 64].

where $\boldsymbol{r}_i(t)$ denotes the position of the ith monomer in the melt at time t and the melt contains M ($=nN$) monomers in total. Qualitatively, $\phi_q(t)$ may be interpreted as the overlap, measured on the scale of the wavelength $1/q$, between the initial configuration of the melt and its configuration at time t, both of which are fully specified by the set of monomer positions $\{\boldsymbol{r}_i(t)\}$. Equation (19) shows that the overlap is normalized at $t = 0$ and decays to 0 in the long time limit provided that the temperature is so high that the configurations can fully decorrelate. A possible means to quantify this loss of memory of the initial state is to introduce a relaxation time, the 'α relaxation time' τ_q, through the condition that $\phi_q(\tau_q)$ has decayed to some small value. Typically, we choose $\phi_q(\tau_q) = 0.1$ [64].

Figure 8 depicts the time dependence of $\phi_q(t)$ for $q \simeq q^*$, as the melt is cooled from $T = 0.7$ to 0.46. In this temperature interval, the α relaxation time increases by more than two orders of magnitude. This disproportionately large change of the dynamics compared to the moderate variation of the structure is an indication for the onset of glass-like behaviour in the Bennemann model. Figure 8 points to a possible origin of the retarded dynamics. With decreasing temperature an intermediate time window emerges, where the relaxation is protracted. This window increases in size on cooling, thus shifting the ultimate decay of $\phi_q(t)$, the so-called 'α relaxation', to longer times.

Such a two-step relaxation of $\phi_q(t)$ is a chief prediction of the mode-coupling theory (MCT) for the structural glass transition [21–24]. The qualitative agreement between the theoretical prediction and the simulation results suggests performing a more detailed comparison. However, since not every two-step relaxation need necessarily be related to the physics described by MCT, we split this comparison into two parts. We first test some qualitative predictions which will provide evidence that an application of MCT to our simulation data might be fruitful. Only then do we carry out the quantitative analysis. To prepare for this comparison we begin by compiling some theoretical background in the next section.

3.3.1. Ideal MCT: leading order results and corrections.

Two versions of mode-coupling theory, known as 'ideal MCT' [23, 24, 139] and 'extended MCT' [23, 24, 139–141], have been developed. The above-mentioned comparison with the simulation data will exclusively explore the applicability of the ideal MCT. So we focus on this version in the following and touch on the extended theory only briefly when discussing the range of validity of the ideal MCT. Our presentation mainly follows references [142, 143].

The ideal MCT proposes an approximate equation of motion for the collective density fluctuations $\phi_q(t)$ at wavevector $\boldsymbol{q}$. This equation couples the dynamics of $\phi_q(t)$ ('mode q') to that of all products $\phi_k(t)\phi_p(t)$, obeying $\boldsymbol{k}+\boldsymbol{p}=\boldsymbol{q}$ (whence the name 'mode-coupling theory'). The coupling coefficients are completely determined by the static structure of the glass former, e.g. by $S(q)$ and $c(q)$. These equilibrium quantities depend on an external control parameter, for instance on T if the pressure or density is fixed. As T decreases, the coupling coefficients become larger, leading to a singular behaviour of $\phi_q(t)$ at a critical temperature T_{c}. More precisely, the mathematical analysis of the mode-coupling equations reveals that the long time limit of $\phi_q(t)$ qualitatively changes at T_{c}:

$$\lim_{t\to\infty}\phi_q(t)=\begin{cases}0 & \text{for } T>T_{\mathrm{c}},\\ f_q(T) & \text{for } T\leqslant T_{\mathrm{c}}.\end{cases} \tag{20}$$

For $T > T_{\mathrm{c}}$, density fluctuations relax completely. This implies that the system eventually loses the memory of its initial state, a characteristic feature of the liquid state. By contrast, density fluctuations cannot fully decay in an amorphous solid: a particle rattles around its initial position without being able to leave the 'cage' built up by its nearest neighbours. Therefore, a finite fraction of $\phi_q(t)$, $0 < f_q < 1$, survives in the long time limit. The value of f_q serves as a measure for the 'solidity' of the amorphous solid on length scale $1/q$. f_q is termed the 'nonergodicity parameter' because the 'ideal glass phase' below T_{c} is 'nonergodic' (in the sense of [144]).

The discovery of T_{c} in the solution of the MCT equations allows one to introduce the 'separation parameter σ',

$$\sigma=C\frac{T_{\mathrm{c}}-T}{T_{\mathrm{c}}}\qquad (C=\text{system dependent constant}), \tag{21}$$

which is utilized as a small parameter to derive asymptotic expansions around T_{c}. The following equations are predictions for small $|\sigma|$.

The separation parameter determines two relevant timescales of the ideal MCT: the β relaxation time t_σ,

$$t_\sigma=\frac{t_0}{|\sigma|^{1/2a}}\qquad (0<a<0.3953), \tag{22}$$

and the α relaxation time t'_σ (valid for $T > T_{\mathrm{c}}$),

$$t'_\sigma=\frac{t_0}{|\sigma|^{\gamma}},\qquad \gamma=\frac{1}{2a}+\frac{1}{2b}\qquad (\gamma>1.765). \tag{23}$$

Here, t_0 denotes a microscopic timescale and b is called the 'von Schweidler exponent' ($0 < b \leqslant 1$). The exponents a and b are not independent of each other. They are related by the 'exponent parameter λ':

$$\lambda=\frac{\Gamma(1-a)^2}{\Gamma(1-2a)}=\frac{\Gamma(1+b)^2}{\Gamma(1+2b)}\qquad (1/2\leqslant\lambda<1). \tag{24}$$

The exponent parameter does not depend on T. It is determined by the equilibrium properties of the glass former at T_{c}.

MCT predicts that $\phi_q(t)$—and in fact all correlation functions whose temporal evolution is coupled to that of $\phi_q(t)$—should relax in two steps if $T \to T_{\mathrm{c}}^{+}$. In the first step, $\phi_q(t)$

approaches a plateau value, the so-called critical nonergodicity parameter f_q^{c} $(=f_q(T_{\mathrm{c}}))$, and in the second step, it relaxes away from f_q^{c} toward zero. MCT refers to the intermediate time window encompassing the plateau as the 'β process'. It precedes and overlaps in its late time part with the α relaxation (cf figure 8). In the following, we will present some MCT predictions for both relaxation processes.

Predictions for the β regime. Mathematically, the β regime is defined as the time window $t_0 \ll t \ll t'_\sigma$ in which $|\phi_q(t) - f_q^{\mathrm{c}}| \ll 1$. (This corresponds to $t \sim t_\sigma$ because $\phi_q(t \approx t_\sigma) = f_q^{\mathrm{c}}$.) In this time window and for $T \to T_{\mathrm{c}}^+$, $\phi_q(t)$ is predicted to obey the equation [23, 24, 142, 143]

$$\phi_q(t) = f_q^{\mathrm{c}} + h_q\sqrt{|\sigma|}\,g(\hat{t})$$
$$\qquad + h_q|\sigma|A_q\,\hat{t}^{-2a} + h_q|\sigma|B^2B_q\,\hat{t}^{2b}, \tag{25}$$

where $\hat{t} = t/t_\sigma$ and $B = B(\lambda)$ is a constant [145]. The first line of equation (25) is called the 'factorization theorem'. This name refers to the property that the correction term for f_q^{c} is split into two factors: a factor depending only on space, the 'critical amplitude h_q', and a factor depending only on time and temperature, the 'β correlator $G(t)$', $G(t) = \sqrt{|\sigma|}\,g(\hat{t})$. Both f_q^{c} and h_q are independent of T.

The factorization theorem is the MCT result in leading order of $\sqrt{|\sigma|}$, the second line of equation (25) representing corrections to it for both short times ($\sim\hat{t}^{-2a}$) and long times ($\sim\hat{t}^{2b}$). These corrections violate the factorization property due the q dependence of the factors A_q and B_q. Expressions for A_q and B_q have been worked out for hard sphere systems [142]. For the subsequent analysis it is only important to know that (i) A_q and B_q are given in terms of the static structure at T_{c}—they are independent of T—and (ii) they exhibit the same dependence on q.

Predictions for the α regime. Within MCT the term 'α regime' refers to the decay of $\phi_q(t)$ from f_q^{c} to zero. As $f_q^{\mathrm{c}} = \phi_q(t \approx t_\sigma)$, this decay occurs for $t \geqslant t_\sigma$, thus overlapping with the β process for $t_\sigma \leqslant t \ll t'_\sigma$. t'_σ is the relevant timescale for the α process. Ideal MCT predicts that the α process satisfies a time–temperature superposition principle (TTSP) for $T \to T_{\mathrm{c}}^+$ [23, 24, 142, 143]. Quite generally, the TTSP means that correlation functions, measured at different T, collapse onto a temperature independent master curve if the time variable is rescaled by the α relaxation time. MCT derives the TTSP in the following form:

$$\phi_q(t) = \tilde{\phi}_q(t/t'_\sigma) \qquad (t \geqslant t_\sigma), \tag{26}$$

where $\tilde{\phi}_q(\cdot)$ denotes the α master curve. This equation needs some explanation, lest the key features be lost. Two points will be highlighted. (i) The master curve is independent of T, but depends on q, i.e., on the correlator under consideration. (ii) There is only one timescale $t'_\sigma(T)$ underlying the α process. Close to T_{c}, all relaxation times τ_q, defined e.g. via $\phi_q(\tau_q) = 0.1$, are predicted to be proportional to $t'_\sigma(T)$. That is,

$$\tau_q(T) = C_q t'_\sigma(T), \tag{27}$$

with C_q being a T independent constant [142].

No simple closed expression for the α master curve is known. However, it can be well approximated by a Kohlrausch–Williams–Watts (KWW) function

$$\phi_q(t) \simeq f_q^{\mathrm{K}} \exp[-(t/\tau_q^{\mathrm{K}})^{\beta_q^{\mathrm{K}}}] \qquad (t \geqslant t_\sigma), \tag{28}$$

except in the regime where β and α processes overlap (i.e., for $t_\sigma \leqslant t \ll t'_\sigma$). There, systematic deviations are expected because the short time expansion of equation (28) does not agree with the exact short time expansion of $\tilde{\phi}_q(t/t'_\sigma)$. The latter is given by

$$\phi_q(t) = f_q^{\mathrm{c}} - h_q B\left(t/t'_\sigma\right)^b \qquad (t_\sigma \leqslant t \ll t'_\sigma), \tag{29}$$

where B is the same constant as in equation (25). Equation (29) is called the 'von Schweidler law'. It shows that $\beta_q^{\mathrm{K}} \neq b$ in general [146]. However, there is a special case, the limit of large q. In this limit, it was proved [147] that there is a time interval $t/t'_\sigma \ll t_q^{\mathrm{K}}/t'_\sigma \leqslant 1$ in which the α process obeys

$$\lim_{q\to\infty} \phi_q(t) = f_q^{\mathrm{c}} \exp[-\Gamma_q (t/t'_\sigma)^b], \qquad \Gamma_q \propto q. \tag{30}$$

This implies

$$\lim_{q\to\infty} f_q^{\mathrm{K}} = f_q^{\mathrm{c}}, \qquad \lim_{q\to\infty} \beta_q^{\mathrm{K}} = b, \qquad \lim_{q\to\infty} \tau_q^{\mathrm{K}} \propto q^{-1/b}\, t'_\sigma. \tag{31}$$

The preceding results for the α process are valid in leading order of σ; corrections are of order $|\sigma|$ [142, 143]. Thus, one expects that the MCT predictions for the α process should extend to higher temperatures than those for β process, corrections to which are of order $\sqrt{|\sigma|}$ (see equation (25)).

Discussion. The previous paragraphs summarized predictions from ideal MCT. These theoretical results have to be put into the perspective of possible applications to simulation (or experimental) data. This naturally leads to the question of their range of validity. We want to briefly address this question via the following three remarks. (A detailed review of the derivation, the physical interpretation, the limitations and an extension of the ideal MCT can be found in [139].)

- MCT aims at describing the structural relaxation of supercooled liquids well outside the time window of the initial decay of $\phi_q(t)$, that is for $t \gg t_0$ (for a precise definition of t_0 see e.g. [148]). Relaxation processes for short times $t \sim t_0$ are not treated properly. Thus, deviations have to be expected in the high T liquid state, where $\phi_q(t)$ already decays on the scale t_0. Some feeling for what 'high T' means can be obtained from a recent comparison between MD simulations for a binary LJ mixture and MCT calculations in which the theory was extended by a model allowing one to describe the short time decay of $\phi_q(t)$ [149]. This study demonstrates that the nonlinear coupling of density fluctuations, responsible for the slow dynamics close to T_{c}, is irrelevant for $T \gtrsim 3$. On the other hand, the nonlinear coupling is no longer negligible at $T = 1$—that is, already for temperatures $T \approx 2T_{\mathrm{c}}$.
- For $T \approx 2T_{\mathrm{c}}$ equations (22–31) cannot be applied yet. Calculations for hard spheres suggest that some of the asymptotic results should become observable for $(T - T_{\mathrm{c}})/T_{\mathrm{c}} < 0.1$ only, whereas much smaller distances from T_{c} are required for them to be fully borne out [142, 143]. This range of validity sensitively depends on q, i.e., on the correlator under consideration, and on whether the dynamics is monitored in the time domain or in the frequency domain. The time domain appears to be better suited for analysis via the asymptotic results [142, 143].
- Not only at high T, but also very close to and below T_{c}, deviations from the ideal MCT are expected. Ideal MCT predicts a complete structural arrest at T_{c}. A freezing at T_{c} is not observed experimentally [21, 150]. (An exception is possibly provided by hard sphere-like colloidal suspensions [128].) Rather than diverging, the structural relaxation time continuously increases when cooling the glass former through T_{c} toward T_{g}. Thus, alternative relaxation mechanisms, not incorporated in the ideal MCT, must exist, which eventually become dominant as $T \to T_{\mathrm{c}}^{+}$ and particularly for $T \lesssim T_{\mathrm{c}}$. Attempts to include these missing relaxation mechanisms have led to the extended version of MCT [140, 141]. However, the validity of this extension is not well understood [151, 152]. So we base the subsequent analysis on the ideal MCT.

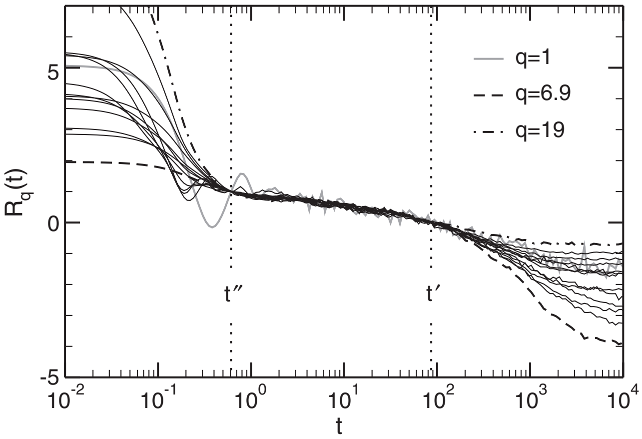

Figure 9. Test of the factorization theorem for $\phi_q(t)$ at $T = 0.46$ via equation (32). By definition, $R_q(t'' = 0.610) = 1$ and $R_q(t' = 86.43) = 0$. The times t' and t'' (vertical dotted lines) were chosen at the beginning and at the end of the plateau region (see figure 8) so that the denominator of equation (32) is large. This is advisable for numerical stability. Note that the order of $\phi_q(t)$ before the β regime is preserved when leaving it at long times (compare e.g. the curves at $q = 6.9$ and 19; the same 'ordering rule' is also observed for simple glass-forming liquids [107, 153]). This is qualitative evidence for the MCT prediction that the short and long time corrections to the factorization theorem exhibit the same q dependence (cf equation (25)). This figure is adapted from [63].

3.3.2. Qualitative comparison: β regime. In the β regime, $\phi_q(t)$ should obey the factorization theorem (cf equation (25))

$$\phi_q(t) = f_q^{\mathrm{c}} + h_q G(t).$$

This equation suggests a simple test which works directly with the simulation data without resorting to any fitting procedure. (Due to this appealing feature the same test was also performed in other simulations of fragile glass formers [107, 153–155] and of SiO$_2$ [156].) Assume that we select two times t' and t'' from the intermediate window where the plateau occurs; they can be any times one likes. Then, the ratio

$$R_q(t) = \frac{\phi_q(t) - \phi_q(t')}{\phi_q(t'') - \phi_q(t')} = \frac{G(t) - G(t')}{G(t'') - G(t')} \tag{32}$$

will be independent of the wavevector if the factorization theorem holds.

Figure 9 shows $R_q(t)$ for $T = 0.46$. We find that there is indeed an intermediate time window where the scattering functions cluster around a master curve. Similar master curves are also obtained at higher T as long as $\phi_q(t)$ decays in two steps (i.e. for $T \lesssim 0.52$; cf figure 8). Furthermore, at a given T the master curve is the same for different correlation functions, such as the incoherent scattering function, the coherent scattering function of the chains and the Rouse mode correlators [63].

Relevance of the result found. The Rouse modes provide a good example that not every two-step process satisfies the factorization property. An indiscriminate fulfilment would of course invalidate equation (32) as a meaningful hint of the applicability of MCT. The factorization theorem was applied to simulation results for the chemically realistic model of *cis–trans* 1,4-polybutadiene [53], alluded to in section 2.1. The test was motivated by the observation of a two-step relaxation for the dynamic Rouse modes (and for the monomer mean square displacement; see figure 3). This relaxation occurs, however, at $T = 273$ K; that is, at a reduced distance to $T_c \approx 216$ K of about $(T - T_c)/T_c \approx 0.26$. For the Bennemann model this would correspond to $T \approx 0.57$, a temperature too large for the two-step decay to be observed (figure 8). In fact, the factorization theorem was found to be violated in [53]. The authors rather argued that the observed two-step relaxation should be interpreted as a consequence of intramolecular rotational barriers for the torsional angles and not as a result of the 'cage effect' underlying the MCT β process (which appears to emerge, however, in the cold melt close to $T_c \approx 216$ K [52]).

Length scales of the β process: evidence for the cage effect. The term 'cage effect' means that a particle in a dense liquid is permanently surrounded by other particles, spatially organized in nearest neighbour shells. The particle is enclosed in a 'cage' and simultaneously 'cages' its neighbours. Thus, any displacement of the particle beyond early time oscillations hinges on the ability of its neighbours to move, and the caged particle itself will trigger motion of the neighbours. This picture appeals to cooperative rearrangements on the scale of the nearest neighbour shells as a prerequisite for structural relaxation to occur. The factorization theorem supplies a convenient means to quantify the spatial extent of this (so-defined) cooperativity for the β process.

Since length scales are easier to visualize in real than in reciprocal space, we introduce the Fourier transform of the intermediate scattering functions, the van Hove correlation functions [119] for the self-part ($G_s(\boldsymbol{r}, t)$) and distinct part ($G_d(\boldsymbol{r}, t)$) of the melt,

$$G_s(\boldsymbol{r}, t) = \frac{1}{nN}\left\langle \sum_{i=1}^{n}\sum_{a=1}^{N} \delta\big(\boldsymbol{r} - [\boldsymbol{r}_i^a(t) - \boldsymbol{r}_i^a(0)]\big)\right\rangle, \tag{33}$$

$$G_d(\boldsymbol{r}, t) = G_p(\boldsymbol{r}, t) + \frac{1}{nN}\left\langle \sum_{i\neq j}^{n}\sum_{a\neq b}^{N} \delta\big(\boldsymbol{r} - [\boldsymbol{r}_i^a(t) - \boldsymbol{r}_j^b(0)]\big)\right\rangle, \tag{34}$$

where $G_p(\boldsymbol{r}, t)$ is the distinct part of the van Hove correlation function for a chain

$$G_p(\boldsymbol{r}, t) = \frac{1}{nN}\left\langle \sum_{i=1}^{n}\sum_{a\neq b}^{N} \delta\big(\boldsymbol{r} - [\boldsymbol{r}_i^a(t) - \boldsymbol{r}_i^b(0)]\big)\right\rangle. \tag{35}$$

Here $\boldsymbol{r}_i^a$ denotes the position of monomer a ($a = 1, \ldots, N$) in chain i ($i = 1, \ldots, n$). In the β regime we expect

$$G_x(r, t) = F_x(r) + H_x(r)G(t) \qquad (x = s, p, d) \tag{36}$$

so the ratio [154, 155]

$$R_x(r, t) = \frac{G_x(r, t) - G_x(r, t')}{G_x(r', t) - G_x(r', t')} = \frac{H_x(r)}{H_x(r')} \qquad (r' = \text{constant}) \tag{37}$$

should be independent of time and inform us about the length scales involved in the β process for the quantity 'x'.

We computed equation (37) for various temperatures. An example for $T = 0.48$ is presented in figure 10. Of course, the main interest of the figure consists in the spatial variation of $R_x(r, t)$; but two key features also emerged from the analysis [63] which should be mentioned. (i) We find master curves which depend on the type 'x' of the correlator, but are independent of T. (ii) The master curves can only be constructed for times from the β window. For shorter and longer times no superposition of the data is obtained. Both findings are in qualitative accord with MCT.

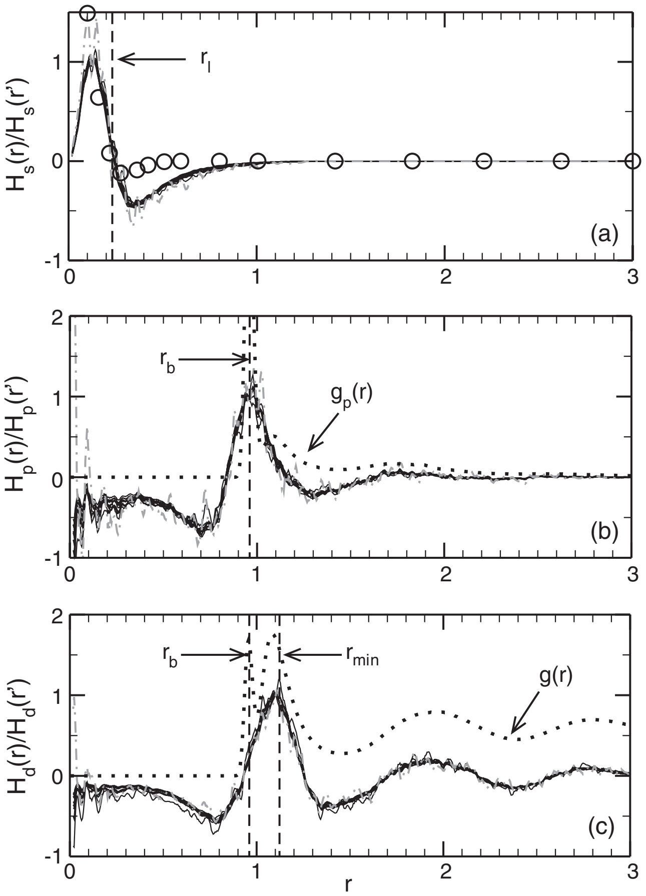

Figure 10. $R_x(r, t)$ (equation (37)) versus distance r for nine different times from the β regime at $T = 0.48$ $(t'' = 0.988 \leqslant t < t' = 21.97)$. Panel (a) shows $R_x(r, t)$ for the self-part of the van Hove function, panel (b) that for the distinct part of the chains and panel (c) that for the distinct part of the melt. For the distinct parts the corresponding pair distribution functions, $g_p(r)$ (chain) and $g(r)$ (melt), are presented for comparison (dotted lines; $g^p(r)$ and $g(r)$ are rescaled to fit into the figure). Note that the first peak of $g(r)$ reflects the two length scales of the model, $r_b \approx 0.97$ and $r_{min} \approx 1.12$ (section 2.2). The constant r' is chosen such that the (positive) denominator of $R_x(r, t)$ is largest at r'_x $(r'_s = 0.13253, r'_p = 0.9575, r'_d = 1.1025)$. This is favourable for numerical stability. In panel (a), r_l $(= 0.2323)$ denotes the zero of $R_s(r, t)$ and the circles represent the Gaussian approximation, equation (39). Equation (39) has a zero at $\sqrt{6}r_{sc} \simeq 0.2327$ and a minimum around $\sqrt{10}r_{sc} \simeq 0.3$. Here, r_{sc} $(\simeq 0.095)$ is the Lindemann localization length (compare the discussion under the heading 'β process at the level of the single-particle motion' in section 3.3.2). In all panels, the dash–dotted grey lines correspond to the time closest to t' where numerical inaccuracies occur because $R_x(r, t)$ is undetermined for $t = t'$. From [63].

Viewing this from the perspective of equation (36) we can conclude that distances for which $H_x(r)$ is zero will not contribute to the relaxation of the van Hove correlation functions. Figure 10 demonstrates that $H_x(r)$ quickly vanishes for distances larger than a few monomer diameters, the most long ranged being the distinct part of the melt, $H_d(r)$, whose oscillations persist to $r \approx 4$. On the level of the collective density fluctuations the β relaxation thus comprises a monomer and its neighbours up to about the fourth-neighbour shell. The most important contributions come from the first-and second-nearest neighbours. This local character of the relaxation is direct evidence for the cage effect.

β process at the level of the single-particle motion. For the self-part of the van Hove function we find that the monomer motion is limited to displacements smaller than 1 (equal to the monomer diameter). For shorter distances, $H_s(r)$ vanishes at $r_l = 0.2323$, is positive for $r < r_l$ and is negative for $r > r_l$. The sign of $H_s(r)$ is an important factor in determining $G_s(r, t)$, i.e., the probability of finding a displacement of size r in time t. To see this we exploit a property of the β correlator $G(t)$. It decreases monotonically with t [142]. So the rate at which the van Hove function relaxes is given by

$$\frac{\partial G_s(r,t)}{\partial t} = -H_s(r)\left|\frac{\partial G(t)}{\partial t}\right| \propto -H_s(r). \tag{38}$$

This equation suggests the following interpretation. In the course of the β process the probability for monomer displacements of size r decreases most where $H_s(r)$ is largest ($r \approx 0.13$), and increases most where it is smallest ($r \approx 0.35$). Since $r = 0.35$ is much less than the monomer diameter, we conclude that a monomer which attempts to replace one of its neighbours—that is, attempts to make a displacement of order 1—is partially reflected back to its initial position. This 'reflection' has also been demonstrated by a different analysis in a simulation of a (polydisperse) hard sphere system [157]. There, it was found that the directions of particle displacements in successive time intervals are on average opposite to each other, provided that $r \lesssim 0.8$. The intermittency of displacements of order 1 is evidence for the transient localization of the particles by their nearest neighbours in the β regime.

For $r < 1$ figure 10(a) shows that there is a characteristic distance, the distance r_l where $H_s(r)$ vanishes. Numerically, r_l agrees with the zero of the Gaussian approximation [63]

$$\frac{H_s(r)}{H_s(r')} \propto (1 - r^2/6r_{sc}^2)\exp\left(-r^2/4r_{sc}^2\right), \tag{39}$$

which occurs at $\sqrt{6}r_{sc} \simeq 0.2327$ ($r_{sc} \simeq 0.095$ [59]). The parameter r_{sc} is called the 'critical localization length' in MCT [143]. Its value may be interpreted in terms of the Lindemann criterion of melting. The criterion states that a (crystalline) solid melts if the particle displacements about the equilibrium position reach ~10% of the particle diameter (see e.g. [158, 159]). Thus, the Gaussian approximation—though only in qualitative agreement with the simulation results for $r \gtrsim r_l$ (figure 10(a))—suggests that r_{sc} is the important length scale for the single-monomer motion in the β regime.

Evidence for string-like motion? Equation (38) also applies to the distinct parts of the van Hove functions. Since $H_p(r)$ and $H_d(r)$ oscillate in phase with the corresponding pair distribution functions for $r \gtrsim 1$ (cf figure 10), distances where the probability of finding another monomer was originally high are depleted, whereas others of initial low probability are populated. So, monomers also penetrate into the region $r < 1$ that another monomer occupied at $t = 0$. Of course, the monomers can only penetrate into this region to the extent that the initially present monomer leaves it. Thus, it is not unreasonable that for $r < 1$, $H_p(r)$ and $H_d(r)$ appear to be the mirror image of $H_s(r)$ for $r \gtrsim r_l$. If a monomer moves away from its initial position by $r \approx 0.35$ (minimum of $H_s(r)$), other monomers can enter the initial exclusion zone up to $r \approx$ monomer diameter $- 0.35 \approx 0.7$ ($\approx$the minimum of $H_p(r)$ and $H_d(r)$). As the displacements involved are small, only nearest neighbours should be able to participate in this partial replacement process. So figure 10 suggests that adjacent monomers follow each other. In fact, a microscopic analysis of the monomer motion supports this interpretation. In section 3.4 we

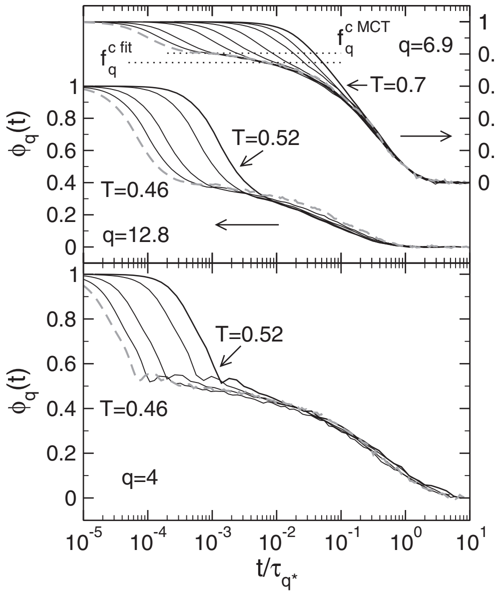

Figure 11. Time–temperature superposition (TTSP) for $\phi_q(t)$ at $q = 4$ (lower panel), 6.9 (right ordinate in upper panel), 12.8 (left ordinate in lower panel). The time axis is scaled by the α relaxation time τ_{q^*} at the maximum of $S(q)$. (Here, we took $q^* = 6.9$; see figure 5.) τ_{q^*} is defined by the condition $\phi_{q^*}(\tau_{q^*}) = 0.1$. Note that the temperature interval where TTSP is well fulfilled depends on the wavevector, and that deviations begin to occur at $T = 0.46$ (dashed lines), i.e., close to T_c ($\simeq$0.45). The dotted horizontal line, labelled '$f_q^{\mathrm{c\,fit}}$', indicates the value of the nonergodicity parameter at $q = 6.9$ resulting from an analysis of the MCT β process via equation (25) (cf section 3.3.4). The dotted horizontal line, labelled '$f_q^{\mathrm{c\,MCT}}$', is the MCT prediction based on the static input obtained from the simulation (cf section 3.3.5). This figure is adapted from [64].

will find that (highly mobile) monomers tend to follow each other in quasi-one-dimensional paths, and that this tendency gradually develops throughout the β regime, is maximum for the early α relaxation and vanishes when the monomer displacements become diffusive.

3.3.3. Qualitative comparison: α regime. In the α regime, $\phi_q(t)$—and other correlation functions coupling to $\phi_q(t)$—are expected to obey the TTSP (equation (26)).

In previous tests of equation (26) a separate scaling time was defined for every correlation function to be analysed [58–61, 64]. For $\phi_q(t)$ this implies that the scaling time depends on q. A more demanding test [149, 160] would employ the same time for all wavevectors, as suggested by equation (27). For instance, one can choose τ_{q^*}, the relaxation time at the maximum of $S(q)$, for all $\boldsymbol{q}$. This choice is made in figure 11. We still find that the TTSP holds, but the quality of the superposition is inferior to that obtained by adapting the scaling time to the q value under consideration (see e.g. [64]).

Irrespective of how the scaling time is chosen we observe deviations from TTSP at both large and small T. At large T, one may argue that the temperature is too far away from T_c for the asymptotic result (26) to apply (see section 3.3.1). Within MCT, deviations at high T are thus expected and predicted to depend on the wavevector [142, 143]. For instance, hard sphere calculations for $\phi_q(t)$ suggest that the TTSP should extend for $q \approx q^*$ to higher T than for wavevectors further away from the maximum of $S(q)$ [142]. We find the same behaviour here (cf figure 11).

The deviations from the TTSP at $T = 0.46$, however, pose a problem for the ideal MCT[13]. They are observed in several recent simulations very close to the critical temperature [161] or critical density [107, 162]. Within MCT these deviations from the ideal behaviour are attributed to additional, not yet well understood relaxation mechanisms (see the discussion at the end of section 3.3.1). Therefore, we focus, in the subsequent quantitative analysis, on $T = 0.47$. This temperature is a compromise: it is close to T_c, but not so close that the additional relaxation mechanisms obscure the characteristics predicted by the ideal MCT, such as the TTSP (cf figure 11).

3.3.4. Quantitative comparison: asymptotic results. Figure 12(a) illustrates the evolution of the structural relaxation close to T_c with two examples: $\phi_q(t)$ and its incoherent counterpart, the incoherent intermediate scattering function $\phi_q^s(t)$,

$$\phi_q^{\mathrm{s}}(t) = \frac{1}{M}\left\langle \sum_{i=1}^{M} \exp\left\{-\mathrm{i}\boldsymbol{q}\cdot\left[\boldsymbol{r}_i(t) - \boldsymbol{r}_i(0)\right]\right\}\right\rangle, \tag{40}$$

where $\boldsymbol{r}_i(t)$ denotes the position of the ith monomer at time t and M ($=nN$) the total number of monomers in the melt. $\phi_q^s(t)$ measures the decorrelation of the positions of an individual monomer with time on length scale $1/q$. Three time regimes may be distinguished in figure 12(a): early times where the initial decay of $\phi_q(t)$ and $\phi_q^s(t)$ from 1 occurs, intermediate times of the β process and late times of the α relaxation.

Early times ($t < 0.2$). The initial decay of the correlation functions is described by the exact short time expansions

$$\phi_q^{\mathrm{s}}(t) = 1 - \frac{1}{2}\,\Omega_q^{\mathrm{s}\,2}\,t^2 + \cdots \qquad \text{with } \Omega_q^{\mathrm{s}\,2} = q^2 v^2, \tag{41}$$

$$\phi_q(t) = 1 - \frac{1}{2}\,\Omega_q^2\,t^2 + \cdots \qquad \text{with } \Omega_q^2 = \frac{q^2 v^2}{S(q)}, \tag{42}$$

where $v = k_B T/m$ ($=T$ in our units) is the thermal velocity.

These short time expansions hint at a possibility for how $\phi_q^s(t)$ and $\phi_q(t)$ could behave at longer times. The term v^2t^2 also determines the initial increase of the monomer mean square displacement (MSD) $g_0(t)$, i.e.,

$$g_0(t) = \left\langle \left[\boldsymbol{r}_i(t) - \boldsymbol{r}_i(0)\right]^2 \right\rangle = 3v^2t^2 + \cdots; \tag{43}$$

this suggests a 'Gaussian approximation' for $\phi_q^s(t)$:

$$\phi_q^{\mathrm{s}}(t) = \exp\left[-\tfrac{1}{6}q^2 g_0(t)\right]. \tag{44}$$

On the other hand, appealing back to equation (42) we may assume that $\phi_q^s(t)$ and $\phi_q(t)$ are closely related to one another, $\phi_q(t)$ being given by

$$\phi_q(t) = \phi_{\tilde{q}}^{\mathrm{s}}(t) \qquad \text{with } \tilde{q} = q/\sqrt{S(q)}. \tag{45}$$

In liquid state theory, this assumption is called 'modified Vineyard approximation' [163]; in [164, 165] it is referred to as a type of 'de Gennes narrowing'.

---

[13] Note, however, that no deviations are observed in the β regime for $T = 0.46$. The simulation data still satisfy the factorization theorem (cf equation (25) and figure 9). The latter finding is not limited to our polymer model; it was also observed e.g. for amorphous silica [156], and it can be rationalized within the framework of MCT. The extended version of the theory shows that the factorization theorem still holds even if ergodicity restoring processes close to and below T_c are taken into account [141].

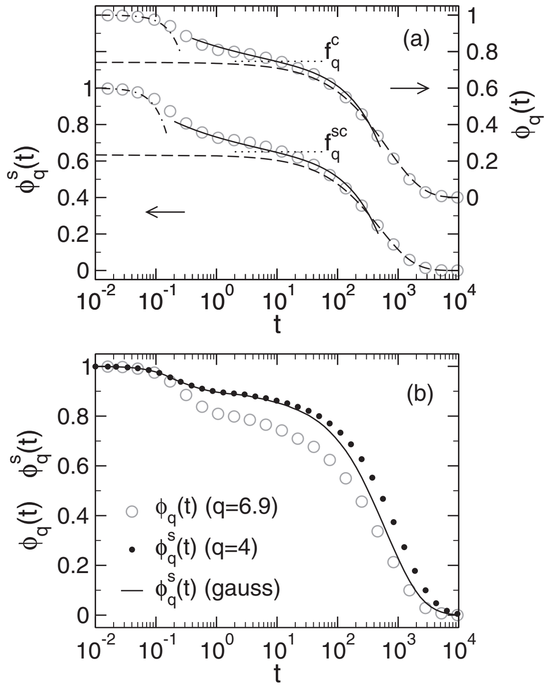

Figure 12. (a) $\phi^{\mathrm{s}}_q(t)$ (left ordinate) and $\phi_q(t)$ (right ordinate) versus time t for $T = 0.47$ and $q = 6.9$ ($\approx$ maximum of $S(q)$; see figure 5). The simulation data (circles) are compared with theoretical formulae which (approximately) describe the decay of the scattering functions in different time regimes: the exact short time expansion of $\phi^{\mathrm{s}}_q(t)$ and $\phi_q(t)$ (dash–dotted lines; equations (41) and (42)), the fit result for the MCT β process (solid lines; equation (25)) and the KWW function (dashed lines; equation (28)). To obtain the parameters of the KWW function the fit interval was limited to large times, where $\phi^{\mathrm{s}}_q(t) < f^{\mathrm{sc}}_q/2$ and $\phi_q(t) < f^{\mathrm{c}}_q/2$. The values of the nonergodicity parameters f^{sc}_q and f^{c}_q, as obtained from the MCT β analysis, are indicated by horizontal dotted lines. (b) Comparison of $\phi^{\mathrm{s}}_q(t)$ (filled circles) with the Gaussian approximation, equation (44) (solid line), at $q = 4$. This q value closely agrees with the value $q/\sqrt{S(q)}$ ($\simeq$4.1) found for $q = 6.9$. The comparison of $\phi_q(t)$ at $q = 6.9$ (open circles) with $\phi^{\mathrm{s}}_q(t)$ at $q = 4$ is thus a test of the modified Vineyard approximation (equation (45)). All data refer to $T = 0.47$.

Figure 12(b) shows that neither of these ansätze provides a satisfactory description. At $q = q^*$ ($\simeq$6.9), $\phi_q(t)$ relaxes more rapidly than $\phi^{\mathrm{s}}_{\tilde{q}}(t)$ at the (smaller) wavevector $\tilde{q}$ ($\simeq$4). $\phi^{\mathrm{s}}_{\tilde{q}}(t)$ in its turn also relaxes more slowly than the Gaussian approximation (44). These deviations reveal the weaknesses of equations (44) and (45). Equation (45) presupposes that correlations in the motion of monomers i and j can be accounted for by a mere shift of the wavenumber in the incoherent scattering function. There is no obvious reason that such a mapping of the collective dynamics onto the single-monomer dynamics is permissible for local processes where intermolecular correlations should be pronounced. On the other hand, equation (44) assumes that the displacement vectors $\boldsymbol{r}_i(t) - \boldsymbol{r}_i(0)$ are for all times Gaussian distributed random variables. This would, for instance, be true if the vectors were linear functions of a random, white noise force. Again, there is no reason to assume that the force exerted on a monomer by the surroundings has this stochastic character for all scales of time and length (outside the transient microscopic regime where equation (43) is valid). Indeed, figure 12(b) shows that $\phi^{\mathrm{s}}_q(t)$ for $q = 4$ exhibits deviations from Gaussian behaviour in the α regime.

A more detailed comparison between equation (44) and the simulation results for $\phi_q^{\mathrm{s}}(t)$ reveals that the extent of the deviations depends on q and t. The following general trends may be pointed out [59]:

(i) For $q \gtrsim q^*$, equation (44) only works for times before the β process. Its range of validity increases with decreasing q. Yet even at $q = 1$, the smallest wavevector studied, deviations are still clearly visible in the late α regime.
(ii) The neglect of some dynamic correlations in the Gaussian approximation makes equation (44) decay faster than the simulated $\phi_q^{\mathrm{s}}(t)$.

The deviations described in (i) and (ii) are not limited to the incoherent scattering function. They are observed also for the coherent scattering function $\phi_q^{\mathrm{p}}(t)$ of a chain, not only in the Bennemann model [63], but also in atomistic simulations of polyethylene [166] and polybutadiene [56, 167]. This implies that one has to be careful when fitting simulation or experimental data for $\phi_q^{\mathrm{p}}(t)$ to the Rouse model [2] of polymer dynamics because the assumption of Gaussian distributed monomer displacements underlies this model. Deviations from the theory or unsatisfactory values of the fit parameters can originate from the non-Gaussian character of the displacements on the scales of length and time where the theory is applied in practice (see also [32] for a topical review of this point).

β regime. Figure 12(a) shows that there is an intermediate time window ($1 \lesssim t \lesssim 100$) in which $\phi_q(t)$ and $\phi_q^{\mathrm{s}}(t)$ decay very slowly with time. The previous qualitative analysis identified this time window with the β relaxation of MCT. For a quantitative analysis we revert to the factorization theorem (equation (25))

$$\phi_q^{\mathrm{x}}(t) = f_q^{\mathrm{xc}} + h_q^{\mathrm{x}}\sqrt{\sigma}\, g(\hat{t}) = f_q^{\mathrm{xc}} + \frac{h_q^{\mathrm{x\,fit}}}{t_\sigma^a}\, g(\hat{t}), \tag{46}$$

where $\hat{t} = t/t_\sigma$ (t_σ is defined in equation (22)) and $h_q^{\mathrm{x\,fit}} = h_q^{\mathrm{x}} t_0^a$. Here we introduced the superscript 'x' to write the equation for incoherent and coherent scattering in a compact form: '$\mathrm{x} = \mathrm{s}$' refers to incoherent scattering, while no superscript is utilized for coherent scattering.

Equation (46) contains four fit parameters, f_q^{xc}, $h_q^{\mathrm{x\,fit}}$, t_σ, and λ which fixes the shape of $g(\hat{t})$. These parameters may be determined in the following way [59]: we start the analysis by focusing on $\phi_q^{\mathrm{s}}(t)$. First, $g(\hat{t})$ is calculated for different values of λ numerically, applying the program used in [141]. The result is then inserted into equation (46) and the remaining parameters are optimized. Iterating this procedure for other values of λ, q and T allows us to find the range of λ which provides a good fit and is consistent with theoretical expectations. The latter condition implies, for instance, that λ should be independent of T, that t_σ should obey equation (22) and that, for a given T, $\phi_q^{\mathrm{s}}(t)$ must equal f_q^{sc} for all q at the same time $t = t_{\mathrm{co}}(T)$ ($\propto t_\sigma$) because $g(\hat{t}_{\mathrm{co}}) = 0$ according to equation (46). More generally, we expect

$$\phi_q^{\mathrm{x}}(t_{\mathrm{co}}) = f_q^{\mathrm{xc}} \qquad \text{for all } q \text{ and 'x'}. \tag{47}$$

This is an important equation: it allows us to determine first t_{co} from the analysis of one correlator, $\phi_q^{\mathrm{s}}(t)$ in our case. The knowledge of t_{co} then supplies an easy means to calculate f_q^{xc} for other correlators 'x'. We applied this strategy to the coherent scattering function of a chain, $\phi_q^{\mathrm{p}}(t)$, and of the melt, $\phi_q(t)$, in [63]. The last remaining parameter, $h_q^{\mathrm{x\,fit}}$, may also be determined by exploiting the analysis of $\phi_q^{\mathrm{s}}(t)$. It can be obtained via

$$h_q^{\mathrm{x\,fit}} = \left.\frac{\partial_t \phi_q^{\mathrm{x}}(t)}{\partial_t [g(\hat{t})/t_\sigma^a]}\right|_{t=t_{\mathrm{co}}}, \tag{48}$$

where the derivatives are evaluated numerically [63].

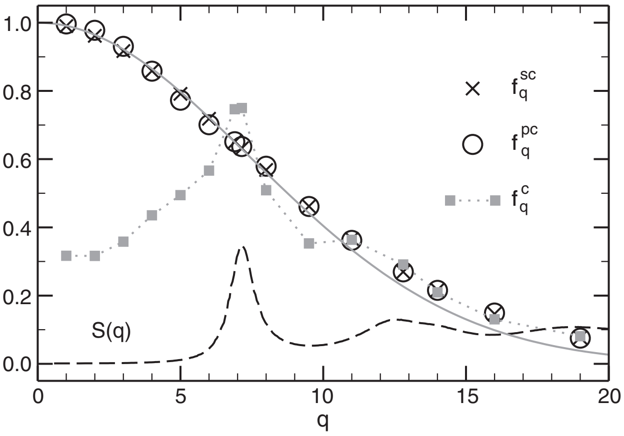

Figure 13. Nonergodicity parameters f_q^{xc} versus q (f_q^{sc}: incoherent scattering; f_q^{pc}: coherent scattering of the chains; f_q^{c}: coherent scattering of the melt). The solid line indicates the Gaussian approximation $f_q^{sc} = \exp(-q^2 r_{sc}^2)$, $r_{sc} \simeq 0.095$ being the Lindemann localization length. The collective static structure factor $S(q)$ for $T = 0.47$ is shown for comparison (dashed line; $S(q)$ is multiplied by 0.1). This figure is adapted from [63].

Figure 12(a) illustrates that the fit procedure described yields a good description of both $\phi_q^s(t)$ and $\phi_q(t)$ in the β regime. The q dependence of f_q^{xc} and h_q^x derived from the fit [59, 63] shares many qualitative features predicted theoretically [142, 143] and also found in simulations of nonpolymeric glass formers, including simple liquids [107, 162, 168, 169], diatomic molecules [170, 171], water [172], *ortho*-terphenyl [160, 161, 173] and SiO$_2$ [174]:

(i) For $q \gtrsim q^*$, f_q^c closely follows the oscillations of $S(q)$ (cf figure 13). For $q \gtrsim 11$, we find that $f_q^c \approx f_q^{sc}$. The agreement between coherent and incoherent scattering becomes better with increasing q.

(ii) f_q^{sc} monotonically decreases with q, being well described by $f_q^{sc} = \exp(-q^2 r_{sc}^2)$ for $q \lesssim 8$. Here, r_{sc} is the Lindemann localization length (compare the discussion under the heading 'β process at the level of the single-particle motion' in section 3.3.2). The value of r_{sc} is about 10% of the monomer diameter.

(iii) The critical amplitude h_q is roughly in antiphase with f_q^c for $q \lesssim 10$ (not shown). We find that, in the same way as f_q^c approaches f_q^{sc}, $h_q^c \approx h_q^{sc}$ for large q.

In addition to these features the following particularities occur for our polymer model. First, f_q^p and h_q^p, the MCT parameters corresponding to the coherent scattering function of a chain, closely agree with their incoherent counterparts, f_q^s and h_q^{sc}, except for small wavevectors ($q < q^*$) probing the size of a chain and beyond. Second, f_q^c exhibits a pronounced shoulder at $q \approx 4$ (cf figure 13). As regards the aforementioned antiphase behaviour with respect to f_q^c, h_q has a minimum at $q = 4$. These features have no parallel in $S(q)$, are absent for simple liquids, but appear to be present for the molecular glass former *ortho*-terphenyl [160, 161].

α regime. In experiments and simulations the KWW function (equation (28)) is commonly found to provide a good description of the α relaxation except at short times ($t \ll \tau_q^K$) [18, 21, 22]. Viewed from the perspective of MCT this failure at early times (for $T > T_c$) is a reflection of the von Schweidler process (equation (29)), governed by the exponent b which is in general different from β_q^K (see section 3.3.1). So, when analysing the α process via the

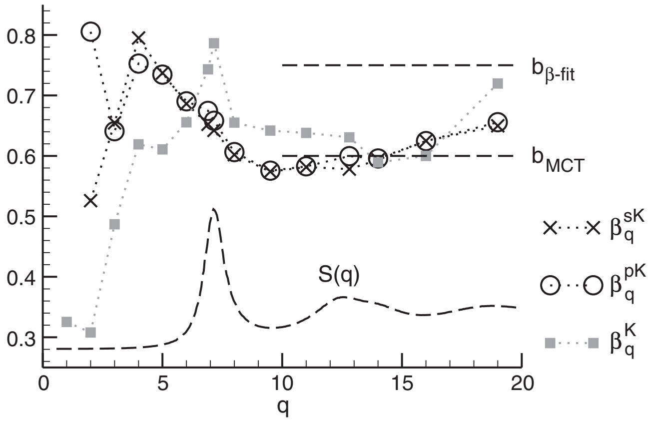

Figure 14. Stretching exponents β_q^{xK} versus q for the α decay of the incoherent (x = s), coherent chain (x = p), and coherent melt scattering functions. The exponents were obtained from a three-parameter fit (f_q^{xK}, τ_q^{xK}, β_q^{xK}) of equation (28) to the simulation data for $\phi_q^{\mathrm{x}}(t)$ at $T = 0.47$. The fit interval was limited to $\phi_q^{\mathrm{x}}(t) < f_q^{\mathrm{xc}}/2$ (see footnote 15). The horizontal dashed lines indicate the von Schweidler exponents derived from the analysis of the β relaxation by fitting the simulation data to equation (25) ($b_{\beta\ \mathrm{fit}} = 0.75$) and from an MCT calculation based on simulated static properties; cf section 3.3.5 ($b_{\mathrm{MCT}} = 0.6$). For comparison, the collective static structure factor $S(q)$ at $T = 0.47$ is shown (dashed line; scaled to fit into the figure).

KWW function we should exclude contributions from the late β regime[14]. Different strategies have been proposed for this purpose (see [63, 64] and references therein). One possibility consists in fitting the late α process only [168, 170], by restricting the fitting interval to, say, $\phi_q^{\mathrm{x}}(t) < f_q^{\mathrm{xc}}/2$.

This is the approach we have chosen here. Figure 12(a) exemplifies the results obtained at $q = q^*$ for $\phi_q^{\mathrm{s}}(t)$ and $\phi_q(t)$. As desired, the KWW function barely overlaps with the β process and provides a good description of the final relaxation. These features are not limited to q^*. Extension of the analysis to other wavevectors gives the following results [59, 64].

The dependence of the KWW amplitude f_q^{xK} on q closely agrees with that of the corresponding nonergodicity parameters for $\phi_q^{\mathrm{s}}(t)$, $\phi_q^{\mathrm{p}}(t)$, and $\phi_q(t)$ (cf figure 13).

From the three parameters of equation (28) the stretching exponent β_q^{xK} is most plagued by uncertainties of the fit[15]. This makes a quantitative interpretation problematic. Still some trends appear to emerge (figure 14).

For $q \gtrsim q^*$ the exponent β_q^{K} derived from $\phi_q(t)$ is roughly in phase with $S(q)$, whereas β_q^{sK} and β_q^{pK}, the exponents for $\phi_q^{\mathrm{s}}(t)$ and $\phi_q^{\mathrm{p}}(t)$, continuously approach a large q asymptote. The asymptote appears to be smaller than $b_{\beta\ \mathrm{fit}}$, the von Schweidler exponent derived from

---

[14] If the β process is not excluded from the analysis, one incurs the risk of finding a temperature dependent stretching exponent β_q^{xK}. Such a result obviously violates the TTSP (equation (26)). See [52, 107] for good recent discussions of this problem.

[15] When fitting the α relaxation with the KWW function one has to take into account that some parameters are very sensitive to the choice of the time interval utilized in the fit. In [64] we found the following trends. The KWW amplitude f_q^{xK} does not vary much with the fit interval. It is usually within 15% of the corresponding nonergodicity parameter f_q^{xc}. As $f_q^{\mathrm{xK}} \approx f_q^{\mathrm{xc}}$, the KWW relaxation time can be determined either by $\phi_q^{\mathrm{x}}(\tau_q^{\mathrm{xK}}) = f_q^{\mathrm{xK}}/\mathrm{e}$ or by $\phi_q^{\mathrm{x}}(\tau_q^{\mathrm{xK}}) = f_q^{\mathrm{xc}}/\mathrm{e}$. We have employed the second prescription in figure 15. In contrast to f_q^{xK} and τ_q^{xK}, the stretching exponent β_q^{xK} appears to be more sensitive to the choice of the fit interval. Depending on q, deviations up to 30% are possible. Particularly at large q ($q \gtrsim 15$), where $f_q^{\mathrm{xK}} \lesssim 0.2$, big fluctuations occur (cf figure 6 of [64] and figure 9 of [59]).

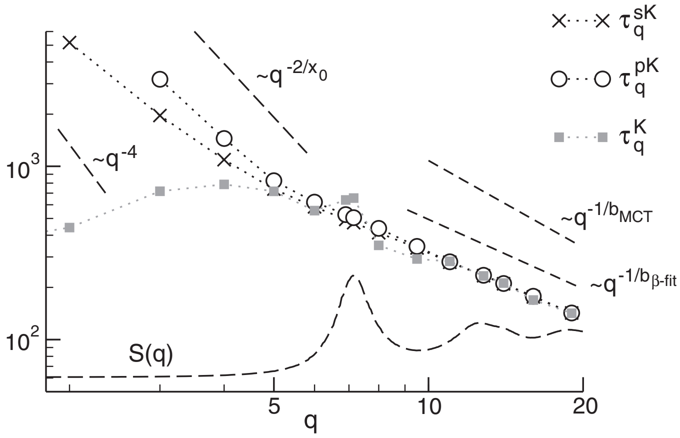

Figure 15. Log–log plot of the KWW relaxation times τ_q^{xK} versus q for the incoherent (x = s), coherent chain (x = p) and coherent melt scattering functions. τ_q^{xK} is defined by $\phi_q^x(\tau_q^{xK}) = f_q^{xc}/e$. The simulation data at $T = 0.47$ are used in the analysis. The q values shown are: $q = 2, 3, 4, 5, 6, 6.9, 7.15, 8, 9.5, 11, 12.8, 14, 16, 19$. The dashed lines labelled '$\sim q^{-1/b_{\beta\,\mathrm{fit}}}$' and '$\sim q^{-1/b_{\mathrm{MCT}}}$' show the large q prediction of MCT (equation (31)), utilizing the von Schweidler exponent from the fit to equation (25) ($b_{\beta\,\mathrm{fit}} = 0.75$) and from an MCT calculation based on static input from the simulation; cf section 3.3.5 ($b_{\mathrm{MCT}} = 0.6$). The dashed lines labelled '$\sim q^{-4}$' and '$\sim q^{-2/x_0}$' indicate respectively equation (51) and equation (53) with $x_0 = 0.63$ ($2/x_0 = 3.2$). S_q (scaled and shifted) is depicted for comparison (dashed line). Note that τ_q^{K} is roughly in phase with $S(q)$ for $q \gtrsim q^*$. This figure is adapted from [64].

Table 1. MCT parameters resulting from fits to the asymptotic formulae of the β process (labelled 'MD'; cf section 3.3.4) [59] and from '*ab initio*' MCT calculations based on static input provided by the simulation (labelled 'MCT'; cf section 3.3.5).

	T_c	λ	a	b	γ
MD	0.450	0.635	0.352	0.75	2.090
MCT	0.277	0.722	0.317	0.60	2.406

the fit to equation (25); a result seemingly in contradiction to equation (31). On the other hand, in section 3.3.5 we will sketch an '*ab initio*' comparison between simulation and theory, suggesting a smaller value for b, $b_{\mathrm{MCT}} = 0.6$ (table 1). This value appears to be in better agreement with the large q behaviour of β_q^{xK} if one takes into account the following two points: (i) β_q^{xK} is hard to determine for $q \gtrsim 15$ (see footnote 15). (ii) The limit $\lim_{q\to\infty} \beta_q^{xK} = b$ should be approached from above—and not from below as in figure 14, provided that $b = b_{\beta\,\mathrm{fit}}$—according to theory [146] and other simulations [107, 160, 162, 172, 175].

Along with the convergence of β_q^{xK} toward b, MCT also predicts $\tau_q^{xK} \sim q^{-1/b}$ in the large q limit (equation (31)) [147]. Figure 15 is indicative of such a common power law for τ_q^{sK}, τ_q^{pK} and τ_q^{K}, if $q \gtrsim 10$. The exponent is compatible with $b = b_{\beta\,\mathrm{fit}}$, but harder to reconcile with $b = b_{\mathrm{MCT}}$, contrary to what was found for β_q^{xK}. A critical inspection of the results obtained for β_q^{xK} and τ_q^{xK} must therefore come to the conclusion that it appears difficult to unambiguously confirm at a quantitative level the large q behaviour of equation (31) in the range of the wavevectors accessible to our simulation (see also [107, 160] for a discussion of this problem).

While the previous discussion focused on $q \gtrsim q^*$—that is, on local length scales for which our model resembles a simple liquid, justifying an interpretation using the MCT developed for these systems—figures 14 and 15 reveal interesting features for $q < q^*$ that are not present for simple liquids. First, $\beta_q^{\rm K}$ exhibits a maximum (or a shoulder [64]) at $q \approx 4$ (figure 14)[16]. This is the same range of q values for which $f_q^{\rm c}$ has a shoulder (figure 13) and where $\tau_q^{\rm K}$ passes through a maximum (figure 15). (A maximum of $\tau_q^{\rm K}$ for $q < q^*$ is also observed for molecular glass formers [160, 161, 170].) Second, $\beta_q^{\rm sK}$ does not continuously increase toward 1, as expected for simple liquids, but appears to tend to a smaller value (figure 14). Similarly, $\tau_q^{\rm sK}$ does not cross over to the hydrodynamic limit $\tau_q^{\rm sK} \sim q^{-2}$ for $q < q^*$, but exhibits a stronger power law dependence (figure 15).

Interpretation via the Rouse model. The range '$q < q^*$' probes length scales corresponding to the structure of chain sections, of the overall chain size and beyond. So it appears natural to search for an explanation based on the theory of polymer dynamics [2]. As long as there are no entanglements, guidance for the interpretation of the incoherent and coherent chain scattering may be obtained from the Rouse model [2, 3]. This model is a theory for a single chain in an effective field. It views a chain as a sequence of monomers ('beads') which are connected by harmonic springs with a force constant proportional to T. Each monomer of this Gaussian chain is subject to a random force and a friction force, both of which are taken to be identical for all monomers. While unrealistic on the local scale of a monomer, the Rouse model is supposed to correctly address universal aspects of polymer dynamics which appear for $q \ll q^*$ and $t \gg \tau_{q^*}$.

For $\phi_q^{\rm s}(t)$ and $\phi_q^{\rm p}(t)$ the model predicts that one has to distinguish between the hydrodynamic regime, realized for $q \ll 1/R_{\rm g}$, and the regime $1/R_{\rm g} \ll q \ll q^*$, which is sensitive to the internal structure of the chain. More precisely, we have (x = s and x = p) [2],

$$\ln \phi_q^{\rm x}(t) \sim \begin{cases} -q^2 D t & q \ll \frac{1}{R_{\rm g}}, \\ -q^2 b^2 (t/\tau_0)^{1/2} & \frac{1}{R_{\rm g}} \ll q \ll q^*, \end{cases} \tag{49}$$

where b is the statistical segment length ($b^2 = \lim_{N\to\infty} R_{\rm e}^2/N$), τ_0 the relaxation time of a monomer (equation (3)) and D denotes the diffusion coefficient of a chain.

The diffusion coefficient can be obtained from both the monomer MSD $g_0(t)$ and the MSD $g_3(t)$ of the chains' centre of mass (COM) via

$$D = \lim_{t\to\infty} \frac{g_0(t)}{6t} = \lim_{t\to\infty} \frac{g_3(t)}{6t}, \qquad g_3(t) = \left\langle \left[\boldsymbol{R}_i(t) - \boldsymbol{R}_i(0) \right]^2 \right\rangle, \tag{50}$$

where $\boldsymbol{R}_i(t)$ denotes the position of the COM of the ith chain at time t.

Equation (49) implies

$$\beta_q^{\rm xK} = \begin{cases} 1 & q \ll \frac{1}{R_{\rm g}}, \\ \frac{1}{2} & \frac{1}{R_{\rm g}} \ll q \ll q^*, \end{cases}$$

and

$$\tau_q^{\rm xK} \sim q^{-2/\beta_q^{\rm xK}} \sim \begin{cases} q^{-2} & q \ll \frac{1}{R_{\rm g}}, \\ q^{-4} & \frac{1}{R_{\rm g}} \ll q \ll q^*. \end{cases} \tag{51}$$

---

[16] In the limit $q \to 0$, the stretching of $\phi_q(t)$ is pronounced; $\beta_q^{\rm K}$ becomes very small, $\beta_q^{\rm K} \approx 0.3$ for $q \lesssim 2$ (figure 14). Such a small KWW exponent for coherent scattering is unexpected from MCT calculations for hard spheres [146]. It might indicate that the α relaxation of collective density fluctuations on large length scales is more complicated in polymer melts than in simple liquids. On the other hand, our simulation data for small q should be considered with care. As $q = 2\pi/L \approx 0.6$ is the smallest q value compatible with the linear dimension L ($\approx$10.5 [59]) of the periodic simulation box, the relatively few reciprocal wavevectors available for $q \lesssim 2$ lead to unsatisfactory statistical precision for $\phi_q(t)$, and the possibility of finite size effects cannot be excluded [63, 64]. On the simulation side, larger systems should be studied to scrutinize the relaxation for small wavevectors.

The key feature of this equation is that there is a stretched exponential decay that is related not to the glass transition, but to chain connectivity. The decrease of β_q^{sK} and β_q^{pK} as well as the power law increase of τ_q^{sK} and τ_q^{pK}, observed in figures 14 and 15 for $q < q^*$, are indications of this Rouse-like relaxation.

We used the term 'Rouse-like' deliberately in the preceding sentence. It shall be stressed that in our simulations [59, 61] we find both accord with Rouse predictions—e.g., the Rouse modes are orthogonal for all t—and deviations from them—e.g., the Rouse modes are stretched with stretching exponents depending on the mode index. Such deviations are not uncommon. They are also observed in other simulations of nonentangled polymer melts using e.g. atomistic models [32], a possible reason being that the separation of length scales $1/R_{\mathrm{g}} \ll q \ll q^*$ required in equation (49) cannot be realized without entanglements setting in[17]. If entanglements should be avoided, the chain length must be limited to $N \lesssim N_{\mathrm{e}}$; but then, finite N corrections to the Rouse behaviour should be expected.

Within the framework of MCT these corrections have recently been discussed for a melt consisting of Gaussian chains whose monomers interact via a hard sphere potential [176]. For $N = 10$, the chain length studied in our simulations, the theory semiquantitatively reproduces the deviations from Rouse behaviour observed in our simulations [59, 61].

These deviations have an impact on $\phi_q^{\mathrm{x}}(t)$ and the q dependence of the corresponding relaxation times. Instead of the Rouse prediction $g_0(t) \sim \sqrt{t}$ for $1 \ll g_0 \ll R_{\mathrm{g}}^2$ [2] we [59, 61]—and also other authors performing simulations [32]—find the monomer MSD to increase with a larger (effective) exponent (see also figure 21),

$$g_0(t) \sim t^{x_0} \qquad \text{with } x_0 = 0.63 \pm 0.03. \tag{52}$$

The monomer MSD will determine $\phi_q^{\mathrm{s}}(t)$ if the Gaussian approximation equation (44) applies. This should be the case for $q \ll q^*$. So we expect

$$\ln \phi_q^{\mathrm{s}}(t) \sim -q^2 t^{x_0} \Rightarrow \tau_q^{\mathrm{sK}} \sim q^{-(2/x_0)\approx -3.2}, \tag{53}$$

which appears to agree with the simulation data better than the Rouse prediction (51); cf figure 15. (Note that neutron scattering experiments typically find smaller values for x_0, i.e., $0.4 \lesssim x_0 \lesssim 0.57$ [47, 48].)

Critique of the quantitative analysis. The previous sections presented a quantitative comparison of the simulation data with the leading order results for the α and β relaxations (section 3.3.1). At this point, it may be appropriate to pause and to comment on the strengths and weaknesses of the analysis.

The chief advantage of the analysis is obvious. It provides detailed, otherwise unobtainable quantitative information about the dynamics of the glass former (above T_{c}). Extracting the q dependence of the relaxation allows for a comparison with the extensively studied hard sphere system [142, 143, 146, 177]. MCT proposes the hard sphere system as the archetypal example of a glass-forming liquid. The reason is as follows: different glass formers certainly differ in their intermolecular interactions. But they all have an amorphous structure, being characterized by a structure factor that is qualitatively similar to the hard sphere $S(q)$. It is $S(q)$ and related quantities that entirely determine the dynamics, according to MCT. So, the hard sphere system should be a simple, but pertinent representative for the class of glass-forming liquids. Confronting the results known for this system with those obtained from a simulated or an experimentally studied glass former helps to shape our understanding of which

---

[17] In the simulations the influence of entanglements on the dynamics may be suppressed by allowing the chains to cross. Then, Rouse-type relaxation is observed even for large N [381, 382].

aspects of the relaxation may be related to the picture proposed from MCT and which of them transcend the theory[18].

The main weakness of the analysis is that it hinges on an intricate fitting procedure. Three (KWW analysis) or four (β analysis) parameters have to be optimized simultaneously. In practice, the range of validity of the asymptotic formulae, equations (20)–(31), is not known *a priori*. Even if one uses the temperature nearest to T_c, which appears to be free from ergodicity restoring processes that the ideal MCT ignores, the distance to T_c may be not close enough to allow for a precise determination of λ [178]. In addition, we have to decide on the time interval where the fit will be performed. The choice of this interval will—or at least can—influence the numerical values of the fit parameters. At several instances, we pointed out that the KWW fit suffers from that problem. But the same concerns also apply to the β analysis.

Both problems—the difficulty of determining λ and the influence of the fit interval—are known. They are discussed in the literature (see e.g. the comment and reply in [179, 180]), but may be hard to avoid in practice [151, 178]. Let us give a case in point, our own analysis.

The analysis of the β process using equation (25) was guided by the idea that the initial part of the plateau region should be describable in terms of the short time behaviour of the β correlator $G(t)$ for $t_0 \ll t \ll t_\sigma \propto t_{\rm co}$. As $\phi_q^{\rm x}(t_{\rm co}) = f_q^{\rm xc}$ (equation (47)), our fit procedure tends to place the nonergodicity parameter in the centre of the plateau region. This analysis seems to be problematic for MD results. Recent simulation studies, comparing for the same model the deterministic MD with an overdamped stochastic dynamics, reveal that the initial decay of $G(t)$ can barely—if at all—be observed in MD simulations. It is largely hidden by the microscopic transient (cf equations (41), (42)) [106, 107]. Thus, a β analysis of MD data should not try to place $t_{\rm co}$ in the centre of the plateau region, but closer to the initial drop of $\phi_q^{\rm x}(t)$ from 1. This implies that our results for $f_q^{\rm x}$ are too small. *A posteriori*, this becomes evident from figure 11. There the TTSP is still fulfilled for $\phi_q(t) > f_q^{\rm c}$, an apparent contradiction to equation (29). This inconsistency could have been avoided if the cross-check with the TTSP had been done. So, information from the α relaxation is crucial for guiding the β analysis (cf appendix A). A similar conclusion was also drawn in [178].

3.3.5. *Quantitative comparison based on static input obtained from the simulation.*

Of course, the uncertainties to be attached to the MCT parameters estimated from the previously discussed fits—even if the fits are judiciously carried out—raise concerns that are hard to dispel. An avenue around this problem would be to avoid the fitting altogether. In principle, this is possible. MCT establishes a link between the equilibrium structure of a glass former, encapsulated in $S(q)$ and related quantities, and its dynamics. Not only do the parameters of the asymptotic formulae (λ, $f_q^{\rm c}$ etc) have precise microscopic definitions, but also the full time dependence of e.g. $\phi_q(t)$ may be calculated from the structure (outside the short time regime). This opens the possibility for an '*ab initio*' comparison between the theoretically predicted and the simulated dynamics.

There is a powerful idea here, albeit one whose applicability is limited to systems for which the theory has been developed and the required static input has been obtained with sufficiently high precision. This restrictive condition has, up to now, allowed for a few applications only. At present, they include a model for amorphous $\mathrm{SiO_2}$ melts [181], a binary LJ mixture [149], a hard sphere mixture [162], a model for *ortho*-terphenyl [160, 161], and a hard sphere(-like) system [107]. Certainly, the potential of this approach has not been fully explored yet.

---

[18] In this respect, the simulation results for *cis–trans* 1,4-polybutadiene, presented in figure 3, do not appear to fit into the MCT picture. The chemically realistic version (CRC) of the model has the same intrachain structure factor and collective structure factor as the model without a torsional potential (FRC). However, the dynamics of the two models are different, the FRC model relaxing faster than the CRC model. It is challenging to see whether this apparent contradiction to the structure–dynamics correlation proposed from MCT could be reconciled (or not) with the theory.

Here, we will present first results of such an '*ab initio*' comparison between the simulated $\phi_q(t)$ and the full solution of a recently proposed extension of MCT to nonentangled polymer melts [176]. Before turning to this comparison we sketch the theory and the numerical tests of some of its assumptions.

Theory. The MCT for nonentangled melts [176] rests on the conceptual framework developed for simple liquids [23, 24, 139]. It also deploys collective density fluctuations to describe the structural relaxation. However, the core variables are not the average density fluctuations (i.e., $\phi_q(t)$), but their (non-normalized) site-resolved counterparts ($a, b = 1, \ldots, N$),

$$\begin{aligned} F_{ab}(q,t) &= \frac{1}{n}\big\langle \rho_a(\boldsymbol{q},t)^* \rho_b(\boldsymbol{q},t)\big\rangle \qquad (n = \text{total number of chains}) \\ &= \frac{1}{n}\left\langle \sum_{i,j=1}^{n} \exp\big\{-\mathrm{i}\boldsymbol{q}\cdot[\boldsymbol{r}_i^a(t) - \boldsymbol{r}_j^b(0)]\big\}\right\rangle. \end{aligned} \tag{54}$$

Appealing back to the notation employed in section 3.2 we denote by $\boldsymbol{r}_i^a(t)$ the position of monomer a in chain i at time t. Furthermore, we see from equation (8) that the initial value of $F_{ab}(q,t)$ is given by $F_{ab}(q,0) = S_{ab}(q) = w_{ab}(q) + \rho h_{ab}(q)$. $F_{ab}(q,t)$ thus comprises intrachain ($w_{ab}(q,t)$) and interchain ($h_{ab}(q,t)$) contributions.

The function $F_{ab}(q,t)$ may be identified as the (a,b) element of the $N \times N$ matrix $\mathbf{F}(q,t)$. By means of the Zwanzig–Mori formalism [119] an exact equation of motion for $\mathbf{F}(q,t)$ may be derived [182]. Specified to the element $F_{ab}(q,t)$ it reads

$$\partial_t^2 F_{ab}(q,t) + \sum_{x=1}^{N} \Omega_{ax}^2(q) F_{xb}(q,t) + \sum_{x=1}^{N} \int_0^t \mathrm{d}t'\, M_{ax}(q,t-t')\partial_{t'} F_{xb}(q,t') = 0, \tag{55}$$

where

$$\Omega_{ax}^2(q) = q^2 v^2\, S_{ax}^{-1}(q) \qquad \text{with } v^2 = k_{\mathrm{B}}T/m (= T \text{ in our units}); \tag{56}$$

here $S_{ax}^{-1}(q)$ denotes the (a,x) element of the inverse of the structure factor matrix $\mathbf{S}(q)$. Equation (55) corresponds to the equation of motion of a damped harmonic oscillator whose 'friction coefficient' $M_{ax}(q,t)$ depends on the full history of the motion of all monomer pairs (a,x). The matrix $\mathbf{M}(q,t)$ is hence referred to as the 'memory kernel'.

The remaining task is to derive an expression for $\mathbf{M}(q,t)$. It is that bit which cannot be handled without approximations [23, 24, 139]. In the framework of MCT the memory kernel is commonly split into a regular contribution and a 'slow' contribution: $\mathbf{M}(q,t) = \mathbf{M}^{\mathrm{reg}}(q,t) + \mathbf{M}^{\mathrm{slow}}(q,t)$ [162].

The regular contribution is supposed to embody memory effects present in the normal high-T state of the liquid (where $\mathbf{M}^{\mathrm{slow}}$ is negligible). $\mathbf{M}^{\mathrm{reg}}$ is assumed to condition the dynamics beyond the (deterministic) short time regime (equation (42)), to lead to a fast decay of density fluctuations and to vary only weakly with T upon cooling. In this sense, it is 'regular'. At all T, $\mathbf{M}^{\mathrm{reg}}$ aggregates only contributions from rapidly fluctuating forces. Because no slow relaxation can result from it, we may pose $\mathbf{M}^{\mathrm{reg}}(q,t) = \mathbf{0}$ (see however the recent study [149] in which the regular kernel was not dropped).

There must also be slow contributions to the fluctuating forces, which ultimately lead to the kinetic arrest in a glassy structure. $\mathbf{M}^{\mathrm{slow}}$ is supposed to contain them. We may regard the memory kernel $\mathbf{M}(q,t)$ as a force–force correlation function [23, 24, 139]. Interaction forces involve pairs of particles (for pair potentials) or—transcribing this idea to the level of collective variables—pairs of densities. So $\mathbf{M}^{\mathrm{slow}}$ should be expressible in terms of the average of the product of four density fluctuations, schematically

$\langle \rho(\boldsymbol{q}_1, t)^* \rho(\boldsymbol{q}_2, t)^* \rho(\boldsymbol{q}_3, 0) \rho(\boldsymbol{q}_4, 0) \rangle$. The core approximation of MCT is now to replace this four-point correlation function with a product of two-point correlation functions. Schematically again, $\langle \rho(\boldsymbol{q}_1, t)^* \rho(\boldsymbol{q}_2, t)^* \rho(\boldsymbol{q}_3, 0) \rho(\boldsymbol{q}_4, 0) \rangle \sim \langle \rho(\boldsymbol{q}_1, t)^* \rho(\boldsymbol{q}_3, 0) \rangle \langle \rho(\boldsymbol{q}_2, t)^* \rho(\boldsymbol{q}_4, 0) \rangle + (3 \leftrightarrow 4)$ [23, 24, 139].

More precisely, the memory kernel is approximated by $M_{ab}(q, t) \approx M^{\text{slow}}_{ab}(q, t) \approx M^{\text{MC}}_{ab}(q, t)$ with [182]

$$M^{\text{MC}}_{ab}(q, t) = \frac{\rho v^2}{(2\pi)^3} \sum_{x,y=1}^{N} \int \mathrm{d}^3\boldsymbol{k} \, \big[k_z^2 c_{ax}(k) c_{by}(k) F_{xy}(k, t) F_{ab}(p, t) + k_z p_z c_{ax}(k) c_{by}(p) F_{xb}(k, t) F_{ay}(p, t) \big], \tag{57}$$

where $\boldsymbol{p} = \boldsymbol{q} - \boldsymbol{k}$ and $\rho = n/V$ is the chain density (equation (7)). The memory kernel (57) is formally identical to the MCT expression obtained for a N-component mixture containing n particles of each component. The intramolecular constraints due to chain connectivity enter this equation only via the Ornstein–Zernike relation for the direct correlation functions $c_{ab}(q)$ (equation (14)).

Equations (55)–(57) furnish a system of closed equations for $\mathbf{F}(q, t)$, provided that the matrices $\mathbf{S}(q)$ and $\mathbf{c}(q)$ are known. From a computational point of view, the solution is, however, demanding; the equations are still of order N^2, and N may become large. It is at this point where the analysis of the static structure, presented in section 3.2, will help us to develop further approximations.

(i) *First approximation*. Figure 6 showed that the equivalent-site approximation (equation (15)) is well justified for the Bennemann model. So we insert $c_{ab}(q) = c(q)$ in equation (57) and obtain

$$M^{\text{MC}}_{ab}(q, t) = \frac{\rho v^2}{(2\pi)^3} \int \mathrm{d}^3\boldsymbol{k} \, \bigg\{ k_z^2 c(k)^2 \bigg[\sum_{x,y=1}^{N} F_{xy}(k, t) \bigg] F_{ab}(p, t) + k_z p_z c(k) c(p) \bigg[\sum_{x=1}^{N} F_{xb}(k, t) \bigg] \bigg[\sum_{y=1}^{N} F_{ay}(p, t) \bigg] \bigg\}. \tag{58}$$

(ii) *Second approximation*. Equation (58) reveals that the equivalent-site approximation does not suffice to simplify the problem. It is still of order N^2. Progress is made if we invoke a further approximation, motivated by PRISM theory. PRISM theory predicts that the site dependent structure factor $S_a(q)$ can be expressed as

$$S_a(q) = \sum_{b=1}^{N} S_{ab}(q) \overset{\text{PRISM}}{=} \left[\frac{\sum_{b=1}^{N} w_{ab}(q)}{w(q)} \right] S(q), \tag{59}$$

and our simulation furthermore suggests that the factor $[\,\cdot\,]$ is almost independent of a. That is, $S_a(q) \simeq S(q)$ (cf figure 16). Assuming that this static property also holds for the dynamics, we may write

$$F_a(q, t) = \sum_{b=1}^{N} F_{ab}(q, t) \approx F(q, t). \tag{60}$$

Equation (60) is an important intermediate result. It allows us to derive a closed MCT equation for the average collective density fluctuations $F(q, t)$, i.e., for

$$F(q, t) = \frac{1}{N} \sum_{a,b=1}^{N} F_{ab}(q, t), \tag{61}$$

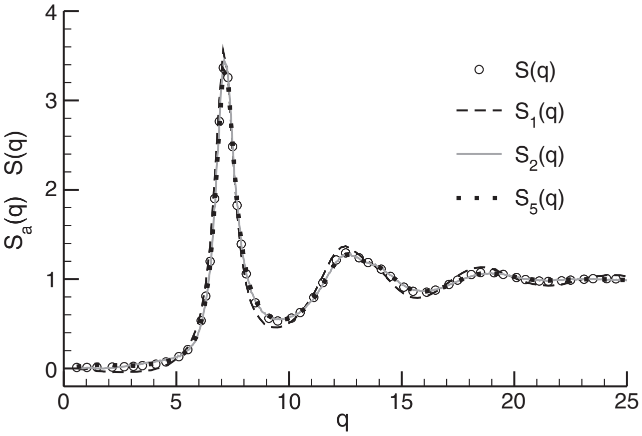

Figure 16. Comparison of the static structure factor $S(q)$ (circles) and the site dependent static structure factor $S_a(q)$ for $a = 1$ (dashed line), $a = 2$ (solid line) and $a = 5$ (dotted line). $S_a(q)$ is defined by the first equality of equation (59). The simulation data for both $S(q)$ and $S_a(q)$ were obtained at $T = 0.47$.

whose initial value is $F(q, 0) = S(q)$ (cf equations (54) and (11)). To this end, we sum equation (55) over a and b and divide by N. Then, we insert equations (58) and (60). This gives the following equation of motion for $\phi_q(t) = F(q, t)/S(q)$:

$$\partial_t^2\phi_q(t) + \Omega_q^2\phi_q(t) + \Omega_q^2\int_0^t \mathrm{d}t'\, m_q^{\mathrm{MC}}(t-t')\partial_{t'}\phi_q(t') = 0, \tag{62}$$

where $\Omega_q^2 = q^2v^2/S(q)$ (cf equation (42)) and

$$m_q^{\mathrm{MC}}(t) \approx \frac{1}{2}\int \mathrm{d}^3\boldsymbol{k}\left[\frac{\rho_{\mathrm{m}}}{(2\pi)^3q^4}S(q)S(k)S(p)\big\{\boldsymbol{q}\cdot\big[\boldsymbol{k}c(k)+\boldsymbol{p}c(p)\big]\big\}^2\right]\phi_k(t)\phi_p(t) \tag{63}$$

with $\boldsymbol{p} = \boldsymbol{q} - \boldsymbol{k}$ and $\rho_{\mathrm{m}} = nN/V$ (equation (7)).

Equations (62) and (63) merit some comments:

(i) For large times, the inertia term, $\partial_t^2\phi_q(t)$, can be neglected. Then, Ω_q^2 drops out and so the relaxation of $\phi_q(t)$ at long times does not depend on the underlying microscopic dynamics. For instance, it should be the same irrespective of whether the system evolves according to Newtonian or Brownian dynamics and it should not depend on inertia parameters. These predictions have been verified in recent simulations on simple glass formers [106, 107, 183].

(ii) Equations (62) and (63) are formally identical to those for monatomic liquids [142]. Polymer-specific effects, such as local stiffness of the chain backbone or chain length N, enter the relaxation only via the direct correlation function, the structure factor and the monomer density. These static equilibrium features fully determine the long time dynamics of the melt.

(iii) Equation (63) shows that the memory kernel contains the factor $S(q)S(k)S(p)$. So, the slow dynamics close to T_{c} should be mainly driven by wavevectors close to q^* [182], because there, $S(q)$ is largest and the strongest dependence on T occurs (cf figure 5).

Comparison with the simulation: first results. The analysis [184] begins with the determination of the critical temperature from equations (62) and (63). We refer to this

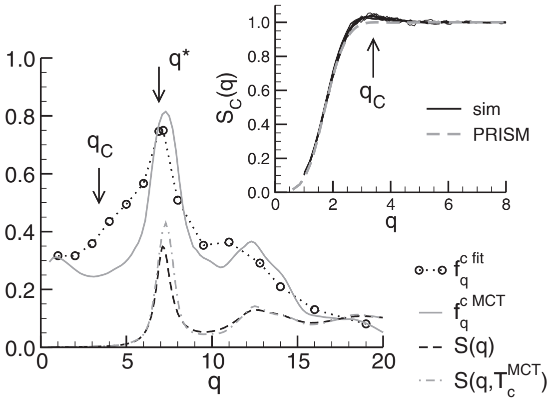

Figure 17. Main figure: wavevector dependence of the nonergodicity parameter (NEP) f_q^{c} determined from $\phi_q(t)$ by means of fits of equation (46) to the simulation data (circles) and by MCT calculations based on structural input from the simulation (solid line). $S(q)$ obtained from simulation at $T = 0.47$ (dashed line) and the extrapolated $S(q)$ at $T_{\mathrm{c}}^{\mathrm{MCT}} \approx 0.277$ (dash–dotted line) are shown for comparison (the structure factors are multiplied by 0.1). The vertical arrows indicate $q_{\mathrm{C}} = 3.4$ (maximum of $S_{\mathrm{C}}(q)$; see inset), and $q^* = 6.9$ ($\approx$ maximum of $S(q)$; see figure 5). Inset: plot of the collective structure factor of the centres of mass of the chains $S_{\mathrm{C}}(q)$ (equation (65)) versus q for all temperatures simulated (solid lines). The dashed line shows the approximation to $S_{\mathrm{C}}(q)$ according to PRISM theory [67]. The arrow indicates the position of a weak maximum occurring in the simulated $S_{\mathrm{C}}(q)$ at $q_{\mathrm{C}} \simeq 3.4$.

temperature as $T_{\mathrm{c}}^{\mathrm{MCT}}$ to discriminate it from the critical temperature $T_{\mathrm{c}}^{\mathrm{MD}} \simeq 0.45$ derived through fits of the asymptotic MCT formulae (section 3.3.4). $T_{\mathrm{c}}^{\mathrm{MCT}}$ may be deduced from the long time limit $\phi_q(t \to \infty) = f_q$ which satisfies the relation

$$\frac{f_q}{1 - f_q} = \mathcal{F}_q(\{f_k\}) \qquad \text{with } m_q(t) = \mathcal{F}_q[\phi_q(t)]. \tag{64}$$

The solution to this equation bifurcates at $T_{\mathrm{c}}^{\mathrm{MCT}}$. For $T > T_{\mathrm{c}}^{\mathrm{MCT}}$, it is $f_q = 0$, while $f_q(T) > 0$ for $T \leqslant T_{\mathrm{c}}^{\mathrm{MCT}}$ (cf equation (20)). From this feature, we obtain the critical nonergodicity parameter via $f_q(T_{\mathrm{c}}^{\mathrm{MCT}}) = f_q^{\mathrm{c}}$.

The technical procedure for turning this general strategy into a practical method is described in [23, 24, 142] and has been applied to simulation results e.g. in [161, 169]. It involves an iterative solution of equation (64) which proceeds from the ‘glass side’ ($T < T_{\mathrm{c}}^{\mathrm{MCT}}$) toward $T_{\mathrm{c}}^{\mathrm{MCT}}$. The analysis is of course predicated upon having the corresponding static input at hand. As long as $T_{\mathrm{c}}^{\mathrm{MCT}}$ lies in the range of temperatures for which equilibrated simulation data are available, the required static input can be determined accurately. However, what if $T_{\mathrm{c}}^{\mathrm{MCT}}$ turns out to be below the lowest equilibrated temperature? This problem occurred in our analysis. In this case, one is inevitably faced with the task of determining the static input by extrapolation from the liquid side. We utilized the simulated $S(q)$ at $T = 0.47$ and 0.48 to carry out the extrapolation. (Due to its very weak dependence on T it was not necessary to include the intrachain structure factor in the extrapolation; cf section 3.2.) The extrapolation provides $S(q)$ at lower T which is inserted in equation (64) to compute $T_{\mathrm{c}}^{\mathrm{MCT}}$. The result is $T_{\mathrm{c}}^{\mathrm{MCT}} \approx 0.277$.

The need to resort to extrapolations is certainly less than ideal. The resulting $S(q)$ may be qualitatively wrong. Fortunately, this concern can be dispelled. Figure 17 depicts $S(q)$ from the simulations at $T = 0.47$ and the extrapolated $S(q)$ at $T_{\mathrm{c}}^{\mathrm{MCT}}$. The latter exhibits the following features: comparing to $S(q)$ at $T = 0.47$, the peak position q^* is shifted to larger wavevectors, the amplitude $S(q^*)$ is higher and the subsequent oscillations for $q > q^*$ are more pronounced. These features agree with the trends observed at $T \geqslant 0.47$ (cf figure 5). One can see this as testimony that the extrapolation was carefully carried out. No qualitative error appears to be introduced. On the other hand, quantitative differences between the extrapolated $S(q)$ and the real $S(q)$—resulting from an analysis of equilibrated configurations at $T_\mathrm{c}^\mathrm{MCT}$—cannot be excluded. To what extent are these uncertainties problematic? No definite answer can be given at present for the polymer model studied. Related work on hard sphere systems suggests that quantitative differences in $S(q)$ may alter the theoretical value of the critical point and the precision of the predicted $f_q^{\mathrm{c\,MCT}}$ [107, 162]. But they appear to have only a weak influence on the exponent parameter λ (cf equation (24)) [107]. So we should expect the uncertainties for $T_\mathrm{c}^\mathrm{MCT}$ and $f_q^{\mathrm{c\,MCT}}$ to be larger than those to be attached to λ^MCT.

Figure 17 compares the theoretical prediction for $f_q(T_\mathrm{c}^\mathrm{MCT}) = f_q^{\mathrm{c\,MCT}}$ with the simulation results from [63] (cf figure 13). For $q \gtrsim q^* = 6.9$ we find a high degree of accord between theory and simulation. This agreement, particularly for q^*, is an important argument in favour of the theoretical approach because it is the intermolecular packing at wavelengths $\sim 1/q^*$ which mainly drives the slowing down of the structural relaxation as the melt is cooled toward T_c. On the other hand, the agreement between theory and simulation is not good for $q \approx 4$. The theory underestimates f_q^c and does not reproduce the shoulder present in the simulation data.

This disagreement is a possible cause of the finding $T_\mathrm{c}^\mathrm{MCT} < T_\mathrm{c}^\mathrm{MD}$. Apparently, there are slow modes around $q \approx 4$ which are not captured by the theory. These modes may couple to the dynamics of other wavevectors, leading to a slowing down of the structural relaxation in the simulation. The only way in which the theory can cope with this additional coupling is to strengthen the cage effect. That is, to increase the first peak of $S(q)$. This requires cooling to lower T and, thence, a smaller critical temperature[19].

If this is so, how could one then introduce the missing coupling into the theory? The inset of figure 17 suggests an avenue. It could be related to the packing of the centres of mass (COMs) of the chains. The shoulder in f_q^c occurs close to a weak peak present in the static structure factor $S_\mathrm{C}(q)$ of the COMs at $q_\mathrm{C} = 3.4$. By analogy to section 3.2, we define $S_\mathrm{C}(q)$ as

$$S_\mathrm{C}(q) = \frac{1}{n}\left\langle \sum_{i,j=1}^{n} \exp\left[-\mathrm{i}\boldsymbol{q}\cdot(\boldsymbol{R}_i - \boldsymbol{R}_j)\right]\right\rangle, \tag{65}$$

where $\boldsymbol{R}_i$ denotes the COM position of the ith chain in the melt. One possibility for improving the theory could thus consist in including the COM as a further interaction site (see [160] for an implementation of this idea in related work).

However, no improvement was found in our case. The reason may be that, unlike $S(q)$, $S_\mathrm{C}(q)$ is practically independent of T and already close to 1 for q_C (cf figure 17 and [67]). Viewed from the perspective of MCT, where the T dependence of the static structure triggers the glassy slowing down on cooling, one is led to conclude that $S_\mathrm{C}(q)$ is not a pertinent variable. The static coupling between the COMs is too weak to make an impact on the glassy dynamics

---

[19] The underestimation of $T_\mathrm{c}^\mathrm{MCT}$ can have yet another origin. The theory utilized the (commonly employed) 'convolution approximation' [24]. This approximation replaces the structure factor $S_3(q, k, p)$ for triplets of monomers by the product $S(q)S(k)S(p)$. The replacement appears to be well justified for simple glass formers [181, 383], but not for structurally more complicated ones, such as *ortho*-terphenyl [161] and silica [181]. In our model we find, analogously to the simple liquids case, that the convolution approximation works quite well, except at intermediate q—that is, just in the interesting region close to q^* [67]. Unfortunately, it is hard to obtain statistically sufficiently accurate results for S_3 in order to estimate to what extent these deviations could be important in a mode-coupling calculation.

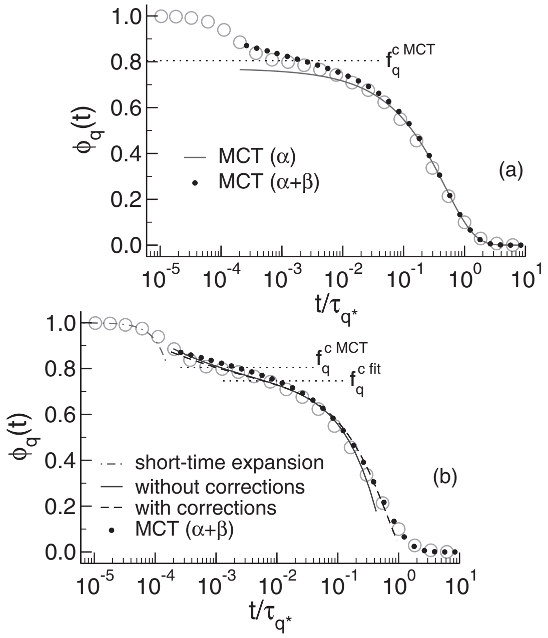

Figure 18. Comparison of the simulation data for $\phi_q(t)$ at $q = 6.9$ and $T = 0.47$ (circles) with various MCT predictions. (a) The solid line is the α master curve; the filled circles depict the solution including both the α and β processes for $\epsilon = (T_c^{MD} - T)/T_c^{MD} = -0.046$ ($T_c^{MD} \simeq 0.45$). The horizontal dotted line shows the MCT prediction for the nonergodicity parameter $f_q^{c\,MCT}$. All theoretical results are based on the static input from the simulation. (b) The exact short time expansion from figure 12 is included (dash–dotted line). For longer times the simulation data are compared with an MCT fit using only the factorization theorem (solid line) [63], an MCT fit including also the next-to-leading order correction to the factorization theorem with short time coefficients calculated from the long time coefficients (dashed line) [63] and the MCT '$\alpha + \beta$' prediction from panel (a) (filled dots). The nonergodicity parameters from the MCT fit, $f_q^{c\,fit}$, and $f_q^{c\,MCT}$ from panel (a) are shown as horizontal dotted lines.

(see also [161] for a related discussion). At present, how to improve the theory around $q \approx 4$ remains elusive.

On the other hand, MCT and simulation closely agree with one another for $q \gtrsim q^*$. In the following, we therefore focus on q^* for analysing the decay of $\phi_q(t)$ in more detail.

Figure 18(a) compares the simulation results for $\phi_q(t)$ at $q^* = 6.9$ and $T = 0.47$ with MCT predictions in the β and α regimes. The static input at T_c^{MCT} suffices for computing the shape of the α master curve (equation (26)). The master curve depends on the scaled time $\tilde{t} = t/t'_\sigma = (t/t_0)\,|\sigma|^\gamma$. As the MCT calculations yield σ and γ (equations (21) and (23)), the only unknown is the matching time t_0. To eliminate t_0 we plot in figure 18(a) the α master curve and the simulation data versus t/τ_q^*. Here, τ_q^* denotes the relaxation time defined independently from the α master curve and the simulation data via the condition $\phi_q(\tau_{q^*}) = 0.1$. Figure 18(a) reveals that, matching theory and simulation at one point—for $\phi_q = 0.1$—suffices for describing the α decay of the simulation data over about two decades in time.

To extend the description to shorter times we also have to take the β process into account. This implies solving the MCT equations at a finite distance, $\epsilon = (T_c - T)/T_c$, from the critical point [24]. In figure 18(a) we utilized the distance corresponding to the simulation data, $\epsilon = -0.046$. The inclusion of the β process extends the description for about one decade to shorter times. For still shorter times, eventually belonging to the microscopic regime ($t/\tau_{q^*} \lesssim 10^{-4}$), deviations are expected because the theory neglects the regular kernel (see the discussion under the heading 'Theory' in section 3.3.5). By the same token, it is also not fully adequate in the regime of crossover between the microscopic transient and the β process. The dynamics in the crossover regime ($10^{-4} \lesssim t/\tau_{q^*} \lesssim 10^{-3}$) is affected by the simulation method; it depends e.g. on whether MD or a stochastic dynamics is employed (cf figure 3 of [106, 107]) and also on inertia parameters [183].

Figure 18(b) recapitulates the results from the comparisons between simulation and MCT presented so far. The figure depicts the β fits to the simulation data, with and without corrections to the factorization theorem (cf section 3.3.4), and the just discussed analysis based on the static input. One clearly sees that in the β regime the two analyses yield descriptions of comparable quality, especially if corrections to the factorization theorem are taken into account. There is, however, one argument which pleads for the analysis based on the static input. It predicts a nonergodicity parameter $f_q^{\mathrm{c\,MCT}}$ that is larger than the fit result $f_q^{\mathrm{c\,fit}}$. If we go back to figure 11, we now find that $f_q^{\mathrm{c\,MCT}}$ lies above the α master curve, no longer violating the TTSP in contrast to $f_q^{\mathrm{c\,fit}}$. Figure 18(b) thus reveals the intricacies of the β analysis via the asymptotic formulae. For distances ϵ, typical of simulations, the choice of a too small value for $f_q^{\mathrm{c\,fit}}$ may be compensated by weaker stretching, i.e., by a larger von Schweidler exponent b (cf table 1). A similar conclusion was also drawn in [178], stressing the importance of including features from the α relaxation to guide the β fits (cf appendix A).

3.3.6. Influence of the thermodynamic path: a case study. A key prediction of MCT is that the low T dynamics is conditioned by the equilibrium properties at the critical point. The critical point is the thermodynamic state of the liquid at T_{c}. For the Bennemann model this state is fully specified—as for any one-component, one-phase system—by two intensive variables. We may choose temperature and pressure. For $p = 1$ the critical point is located at $p = p_{\mathrm{c}} = 1, T_{\mathrm{c}} \simeq 0.45$. This corresponds to the monomer density $\rho_{\mathrm{m}}(p_{\mathrm{c}}, T_{\mathrm{c}}) = \rho_{\mathrm{mc}} \simeq 1.042$.[20] We may invert the last equation, $T_{\mathrm{c}} = T_{\mathrm{c}}(p_{\mathrm{c}}, \rho_{\mathrm{mc}})$. This relation suggests the following interpretation: performing a constant-pressure simulation at p_{c} or a constant-volume simulation at ρ_{mc} should yield the same critical temperature and so, according to section 3.3.1, also the same dynamic features, in particular the same value for λ (equation (24)).

We tested this idea in [60] by comparing simulation results at constant pressure ($p = 1$) with those at constant volume ($\rho_{\mathrm{m}} = 1.042$). Within the numerical uncertainties, we do indeed find the same T_{c} and λ. Figure 19 provides an example. Its main part depicts the T dependence of the relaxation times associated with $\phi_q^{\mathrm{s}}(t)$ and the second Legendre polynomial of the orientational correlations of the end-to-end vector $\boldsymbol{R}_{\mathrm{e}}(t)$:

$$\phi_{\mathrm{E2}}(t) = \tfrac{3}{2}\left[\left\langle\left[\boldsymbol{e}(t)\cdot\boldsymbol{e}(0)\right]^2\right\rangle - \tfrac{1}{3}\right], \qquad \boldsymbol{e}(t) = \frac{\boldsymbol{R}_{\mathrm{e}}(t)}{|\boldsymbol{R}_{\mathrm{e}}(t)|}. \tag{66}$$

Figure 19 reveals that there is a T interval where the relaxation times increase as

$$\tau(T) \propto (T - T_{\mathrm{c}})^{-\gamma}, \tag{67}$$

---

[20] At $p = 1$, $T_{\mathrm{c}} \simeq 0.45$ and $\rho_{\mathrm{mc}} \simeq 1.042$. For other pressures different values for the critical temperature and density are obtained. Nevertheless, we found that $\Gamma_{\mathrm{c}} = \rho_{\mathrm{mc}} T_{\mathrm{c}}{}^{-1/4}$ is, to a good approximation, constant for all pressures studied ($\Gamma_{\mathrm{c}} = 1.27 \pm 0.02$) [60]. $\Gamma \propto \rho_{\mathrm{m}} T^{-1/4}$ is the only relevant parameter needed to fully specify the thermodynamic state of a 3D soft sphere system whose repulsive interaction is proportional to r^{-12} [119]. This finding illustrates the important role that excluded volume interactions play close to the MCT critical point. The same observation has not only been made for glass-forming soft sphere [384] or LJ systems [169], but also e.g. in experiments [385] and simulations [160] of *ortho*-terphenyl.

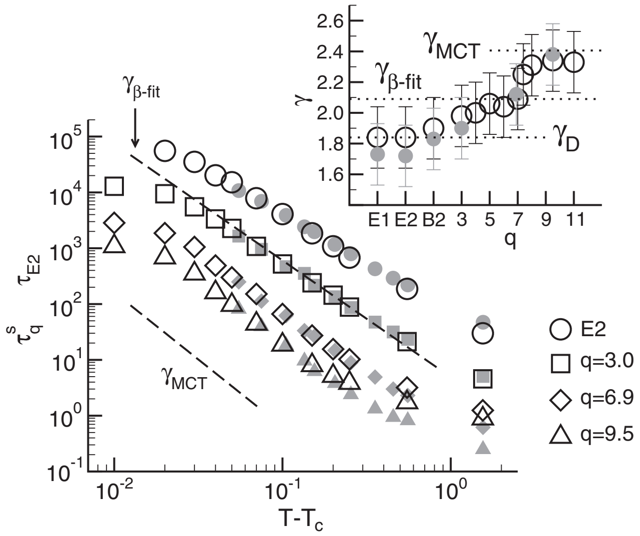

Figure 19. Temperature dependences of different relaxation times, obtained from simulations at constant pressure (open symbols) and at constant volume (filled symbols). The constant-pressure simulations were performed at $p = 1$, leading to the density $\rho_m = 1.042$ at $T_c = 0.45$. We utilized this density in the constant-volume simulations. τ_q^s and τ_{E2} are the relaxation times of the incoherent scattering function $\phi_q^s(t)$ (equation (40)) and of the second Legendre polynomial of the normalized end-to-end vector $\phi_{E2}(t)$ (equation (66)), respectively. The relaxation times are defined by the condition $\phi_x(\tau_x) = 0.3$. The constant-pressure data are multiplied by an arbitrary factor so as to optimize the superposition with the constant-volume results. (The factors are: 14.3 (E2), 16.5 ($q = 3$), 18.7 ($q = 6.9$) and 19.8 ($q = 9.5$).) The dashed lines indicate the γ values obtained from the MCT fit to the β regime ($\gamma_{\beta\text{ fit}} = 2.09$; section 3.3.4) and from the '*ab initio*' MCT analysis ($\gamma_{\text{MCT}} = 2.406$; section 3.3.5). Inset: values of γ determined from the simulations at $p = 1$ (open symbols) and at $\rho_m = 1.042$ (filled symbols) via fits to equation (67). On the abscissa, we quote the quantities from which γ was calculated (E1 and E2 = the first and second Legendre polynomials of the normalized end-to-end vector, B2 = the second Legendre polynomial of the normalized bond vector, $3 \leqslant q < 12 = \tau_q^s$ for these q values). The horizontal dotted lines indicate γ_{MCT}, $\gamma_{\beta\text{ fit}}$ and the value obtained from a fit to the temperature dependence of the diffusion coefficient of a chain ($\gamma_D = 1.84$). This figure is adapted from [60].

with T_c and γ being the same for the two thermodynamic paths. This agrees with the expectation from ideal MCT (cf equations (23) and (27)). However, the figure also reveals two points of disagreement, the first expected, the second problematic.

First, the power law (67) does not apply for all T. Both at low and at high temperature deviations occur. These deviations from the ideal behaviour are expected (see the discussion at the end of section 3.3.1): at high T the asymptotic formulae are no longer valid; very close to T_c ergodicity restoring processes, missing in the ideal theory, become dominant.

Second, if we fix T_c—as is done in figure 19—and determine γ by including in the fit the maximum number of temperatures compatible with equation (67), we find that γ depends on the quantity under consideration (inset of the figure). This dependence is unexpected within MCT and poses a problem. More precisely, the inset of figure 19 shows that γ decreases with increasing length scale, eventually converging toward γ_D, the exponent obtained for the diffusion coefficient of a chain [64]. The observation that relaxation processes on large length scales appear to present a weaker slowing down than those on scales $q \gtrsim q^*$ is not particular to the polymer model studied. It is also found in simulations of simple glass-forming liquids [107, 162, 185].

A feature that is particular to polymers is the correlation functions associated with reorientations (of parts) of the chain backbone. Figure 19 provides examples in terms of the first or second Legendre polynomials of the bond or end-to-end vectors. When analysing the corresponding relaxation times via equation (67) we find γ values that agree, within the error bars, with γ_D. How can we understand that the orientational dynamics of a chain is related to density fluctuations in the small wavenumber limit (cf equation (49))?

Polymer physics suggests a clue to the answer. The dynamics of nonentangled chains is usually discussed in terms of the Rouse model (see the heading 'Interpretation via the Rouse model' in section 3.3.4 or [2]). The basic variables of the model are the 'Rouse modes', the cosine transforms of the position vectors to the monomers of a (tagged) chain s, $\{\boldsymbol{r}_s^a\}_{a=1,\ldots,N}$ [186],

$$\boldsymbol{X}_p(t) = \frac{1}{N}\sum_{a=1}^{N} \boldsymbol{r}_s^a(t)\cos\frac{(a-\frac{1}{2})p\pi}{N} \qquad (p = 0,\ldots,N-1). \tag{68}$$

In the framework of the Rouse model the modes obey $\langle \boldsymbol{X}_p(t)\cdot\boldsymbol{X}_{p'}(0)\rangle \propto \delta_{pp'}$. We verified this orthogonality for the Bennemann model [61]. This feature suffices to show that orientational correlation functions, such as the first Legendre polynomial of the bond and end-to-end vectors, may be expressed as a superposition of $C_p(t) = \langle \boldsymbol{X}_p(t)\cdot\boldsymbol{X}_p(0)\rangle$ for $p > 0$ [2]. On the other hand, $C_p(t)$ is related to the density correlator of a single chain,

$$F_{ab}^{\mathrm{s}}(q,t) = \left\langle \exp\left\{-\mathrm{i}\boldsymbol{q}\cdot\left[\boldsymbol{r}_s^a(t)-\boldsymbol{r}_s^b(0)\right]\right\}\right\rangle, \tag{69}$$

through

$$\begin{aligned} C_p(t) &= \frac{1}{N^2}\sum_{a,b=1}^{N}\left\langle \boldsymbol{r}_s^a(t)\cdot\boldsymbol{r}_s^b(0)\right\rangle \cos\frac{(a-\frac{1}{2})p\pi}{N}\cos\frac{(b-\frac{1}{2})p\pi}{N} \\ &= \lim_{q\to 0}\left[\frac{1}{N^2}\sum_{a,b=1}^{N}\left[\frac{3}{q^2}F_{ab}^{\mathrm{s}}(q,t)\right]\cos\frac{(a-\frac{1}{2})p\pi}{N}\cos\frac{(b-\frac{1}{2})p\pi}{N}\right]. \end{aligned} \tag{70}$$

This completes our line of reasoning. As the relaxation of the Rouse modes is determined by the small q limit of single-chain density fluctuations, we expect related orientational correlation functions to be so too.

3.4. Spatially correlated dynamics: analysis of clustering phenomena

The differences between the simulation and MCT, discussed in connection with figure 19, may be interpreted in another way. MCT predicts that all relaxation times—as well as the self-diffusion coefficient D and the viscosity η—have close to T_{c} the same temperature dependence as t'_σ (equation (27)). Figure 19 indicates a violation of this coupling to one underlying timescale t'_σ. The problem is recapitulated in figure 20. While incoherent and coherent relaxation times are proportional to one another on the local scale q^*, the proportionality breaks down on cooling toward T_{c} as q decreases; the corresponding relaxation times prove to be smaller than expected. Figure 20 bears a conspicuous resemblance—albeit for $T > T_{\mathrm{c}}$—to the breakdown of the Stokes–Einstein relation $D \sim T/\eta$ often found in experiments near T_{g} [188, 189] (for a comparative discussion of experimental results see e.g. [18]; for recent results on nonentangled polystyrene melts see [187]).

A popular explanation of the different T dependences of D and T/η invokes the existence of spatially heterogeneous dynamics ('dynamic heterogeneity'; for general reviews see [190–193]; for a discussion in the context of chemically realistic polymer models see [32]). The term 'dynamic heterogeneity' circumscribes the idea that a glass former near T_{g} contains

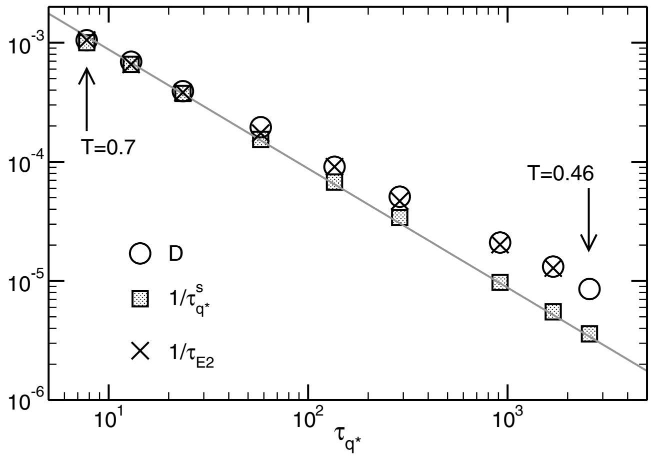

Figure 20. Plot of D (circles), $1/\tau^{s}_{q*}$ (squares) and $1/\tau_{E2}$ (crosses) versus the collective α relaxation time τ_{q^*}. τ^{s}_{q*} and τ_{E2} are taken from figure 19; τ_{q^*} is taken from [64]. The highest ($T = 0.7$) and lowest ($T = 0.46$) temperatures are shown by arrows (remember that $T_c \simeq 0.45$; the other temperatures are (from left to right): $T = 0.65, 0.6, 0.55, 0.52, 0.5, 0.48, 0.47$). The data for $1/\tau^{s}_{q*}$ and $1/\tau_{E2}$ are divided by some factor (= 494 for τ^{s}_{q*}, = 4.85 for τ_{E2}) so that they agree with D (=0.001 05) at $T = 0.7$. The solid line indicates the slope -1. If one assumes $\tau_{q^*}(T) \sim \eta(T)$, the results presented here are strikingly similar to those obtained near T_g for nonentangled polymer melts (cf figure 9 of [187]).

aggregates (‘subensembles’) of particles possessing an enhanced or a reduced mobility relative to the average. One should not envisage these aggregates as static objects; they fluctuate throughout the system with a finite lifetime. Particles that are ‘fast’ at some time will eventually become ‘slow’ and vice versa. This must be so because the liquid is ergodic above T_g: if a particle that was initially in a ‘fast region’ always stayed there, the time average over its trajectory would not agree with the ensemble average over all particles, thus violating ergodicity.

Viewed from the perspective of dynamic heterogeneity the breakdown of the Stokes–Einstein relation is interpreted in terms of the different manner in which the mean square displacement (and so D) and the stress correlation function (and so η) sample the relaxation time distribution associated with spatially heterogeneous dynamics. The mean square displacement should be dominated by the more mobile particles, while the slow regions should mainly determine the relaxation of the stress correlations. Since the width of the relaxation time distribution is expected to increase on cooling, so does the disparity between fast and slow regions. This may lead to different T dependences of D and T/η.[21]

The similarity between plots of the violation of the Stokes–Einstein relation and figure 20 suggests looking for spatially heterogeneous dynamics in our polymer model. The method used to broach this problem computationally has been inspired by experiments. In the research on dynamic heterogeneity, experimental techniques have been developed which allow one to select subensembles of fast or slow particles and to monitor their time evolution [190, 191, 193]. We employ a similar filtering technique here, focusing on spatial correlations of highly mobile monomers [66, 194]. The analysis closely follows the work of [195–197].

---

[21] Whether a broad relaxation time distribution must necessarily lead to a decoupling of the temperature dependences of D and T/η is still a matter of debate (see e.g. [191]). As an aside, MCT also predicts a significant broadening of the relaxation time distribution for $T \to T_c^+$ [177] without entailing a violation of the Stokes–Einstein relation.

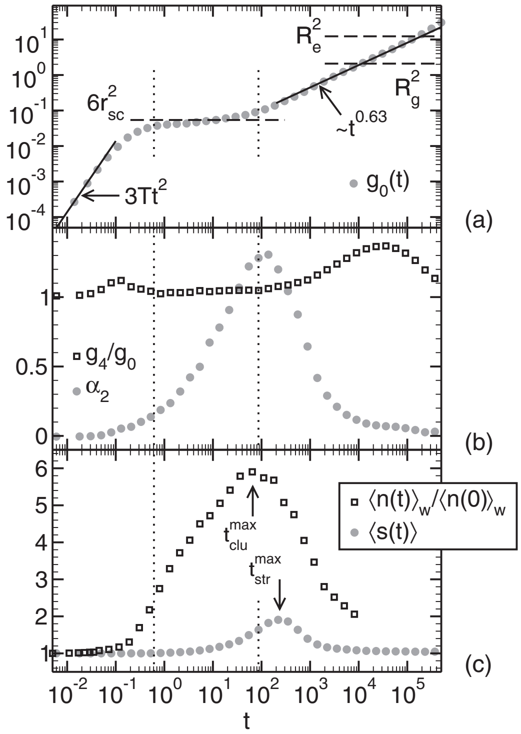

Figure 21. Various dynamic quantities for the Bennemann model at $T = 0.46$. In panels (a)–(c), the vertical dotted lines at $t = 0.61$ and 86.43 roughly indicate the time window of the MCT β process. They are taken from figure 9. (a) Mean square displacement (MSD) of all monomers $g_0(t)$ versus t. The behaviour in the ballistic ($\sim t^2$) and the polymer-specific regimes ($\sim t^{0.63}$; cf equation (52)) are shown by solid lines. The horizontal dashed lines depict $6r_{\mathrm{sc}}^2$ (the Lindemann localization length $r_{\mathrm{sc}} \simeq 0.095$), the radius of gyration R_{g}^2 (=2.09), and the end-to-end distance R_{e}^2 (=12.3). (b) Non-Gaussian parameter of the monomers $\alpha_2(t)$ (equation (73)) and $g_4(t)/g_0(t)$ versus t. $g_4(t)$ is the MSD of the end monomers. (c) Number-averaged string length $\langle s(t)\rangle$ and weight-averaged cluster size $\langle n(t)\rangle_{\mathrm{w}}$ versus t. $\langle n(t)\rangle_{\mathrm{w}}$ is normalized by its initial value $\langle n(0)\rangle_{\mathrm{w}}$ (data reproduced with permission from [194]). The arrows indicate the peak times of $\langle n(t)\rangle_{\mathrm{w}}$ ($t_{\mathrm{clu}}^{\max} = 65.85$) and $\langle s(t)\rangle$ ($t_{\mathrm{str}}^{\max} = 236.26$). This figure is adapted from [66].

Selecting mobile monomers: motivation. Studies of spatially heterogeneous dynamics in a supercooled binary LJ mixture [195–197] identified the 'mobile subensemble' as the set of all particles that move further than distance r^* in time t^*. More formally, the fraction ϕ_{m} of mobile particles is defined by

$$\phi_{\mathrm{m}} = \int_{r^*}^{\infty} \mathrm{d}r\, 4\pi r^2 G_{\mathrm{s}}(r, t^*), \tag{71}$$

where $G_{\mathrm{s}}(r, t)$ is the self-part of the van Hove correlation function (equation (33)).

To choose the parameters r^* and t^* the following criterion was employed: t^* was taken as the time where the non-Gaussian parameter $\alpha_2(t)$ is maximum, and r^* as the distance beyond which the tail of $G_{\mathrm{s}}(r, t^*)$ is larger than that of the Gaussian approximation [119]

$$G_{\mathrm{s}}^{\mathrm{G}}(r, t^*) = \left[\frac{3}{2\pi g_0(t^*)}\right]^{3/2} \exp\left[-\frac{3r^2}{2g_0(t^*)}\right]; \tag{72}$$

$g_0(t) = \langle [\boldsymbol{r}_i(t) - \boldsymbol{r}_i(0)]^2\rangle$ is the mean square displacement (MSD) of a particle. Why are these choices for r^* and t^* expedient?

The non-Gaussian parameter $\alpha_2(t)$ compares the mean quartic displacement of a monomer to the square of $g_0(t)$. It is defined by [119]

$$\alpha_2(t) = \frac{3\left\langle [\boldsymbol{r}_i(t) - \boldsymbol{r}_i(0)]^4 \right\rangle}{5\, g_0(t)^2} - 1. \tag{73}$$

This quantity has a lower bound $\alpha_2(t) \geqslant -2/5$ because $\langle [\boldsymbol{r}_i(t) - \boldsymbol{r}_i(0)]^4 \rangle \geqslant g_0(t)^2$, and vanishes if the displacements are Gaussian distributed. A negative value of $\alpha_2(t)$ implies that a monomer moves on average less far than expected e.g. from diffusive Brownian motion. A positive value, on the other hand, indicates that the monomer moves further than a Brownian particle in the same time. A large value of $\alpha_2(t)$ is thus a good indicator of enhanced mobility relative to ordinary diffusion.

Figure 21 depicts $\alpha_2(t)$ and $g_0(t)$ for the Bennemann model at $T = 0.46$ [66]. At short times, the monomers move 'ballistically': $g_0(t) \propto t^2$ (equation (43)), $G_\mathrm{s}(r, t)$ is Gaussian [119] and so $\alpha_2(t) = 0$. The regime of ballistic motion is succeeded by a 'plateau regime'. There $g_0(t)$ increases only slowly with time; the MSD is of the order of 10% of the monomer diameter. This reflects the temporary caging of a monomer by its neighbours. The plateau regime may thus be identified with the MCT β process (see section 3.3.2). In this regime, $\alpha_2(t)$ continuously increases toward a maximum. The maximum occurs at time t^* which is located in a time interval where the monomers, on average, begin to leave their cages (late β/early α process). For longer times, $\alpha_2(t)$ decreases again and $g_0(t) \sim t^{0.63}$ (equation (52)). This subdiffusive behaviour can be attributed to chain connectivity (see the discussion in the paragraph starting at the heading 'Interpretation via the Rouse model' in section 3.3.4). Chain connectivity dominates the monomer dynamics until the MSD becomes comparable to the chain size, $g_0 \sim R_\mathrm{e}^2$. Then, final diffusion sets in: $g_0(t) \propto t$ (equation (50)), $G_\mathrm{s}(r, t)$ is again Gaussian [119] and so $\alpha_2(t) = 0$.

Figure 21 demonstrates that $\alpha_2(t)$ is positive—this feature may be predicted theoretically [143] and is often observed in simulations [47, 155, 170, 173, 174, 198] and experiments [199–201] of glass-forming liquids. The monomers in the cold melt close to T_c thus move substantially further than expected from purely diffusive dynamics, particularly at the peak time t^*. This suggests choosing t^* as the time to select mobile monomers.

The enhanced monomer mobility near t^* cannot be attributed to chain ends. In the time interval where $\alpha_2(t)$ is large, the mean square displacement $g_4(t)$ of the end monomers closely agrees with $g_0(t)$ (figure 21(b)). Only for $t > t^*$, where $\alpha_2(t)$ is small again and $g_0(t)$ is dominated by chain connectivity, do we find $g_4(t) > g_0(t)$. In this time regime, the inequality '$g_4 > g_0$' is predicted by the Rouse model [2] and expected to persist up to the diffusive regime (see [66, 194] for a fuller discussion).

The criterion for selecting t^* rests upon a comparison with Gaussian behaviour. The same procedure should be employed to define r^*, whence the idea of comparing $G_\mathrm{s}(r, t^*)$ to the Gaussian approximation $G_\mathrm{s}^\mathrm{G}(r, t^*)$ (figure 22) and defining r^* as the crossing point of $G_\mathrm{s}(r, t^*)$ and $G_\mathrm{s}^\mathrm{G}(r, t^*)$ for large r.

Selecting mobile monomers: final definition. If these choices for t^* and r^* are inserted in equation (71), the fraction of mobile monomers is found to be $6.2\% \leqslant \phi_\mathrm{m} \leqslant 6.8\%$, depending on temperature [194]. Apparently, ϕ_m varies only weakly with T. So, it appears appropriate to fix an intermediate value $\phi_\mathrm{m} = 6.5\%$ for all temperatures.

However, once we decide to fix ϕ_m, we can not only do this for all T, but also for all times. That is, we 'select a dynamically distinguishable subensemble' [190] of mobile particles by ranking the scalar displacements $\mu_i(t) = |\boldsymbol{r}_i(t) - \boldsymbol{r}_i(0)|$ of all monomers i at time t and choosing the 6.5% with the largest μ_i.

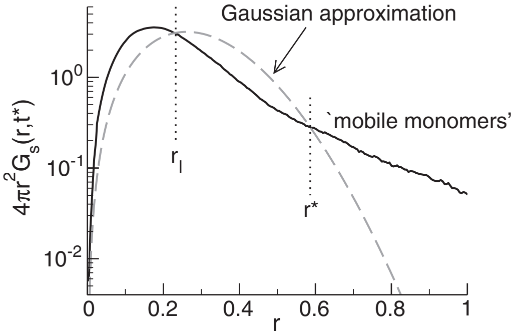

Figure 22. Comparison of the self-part of the van Hove correlation function $G_s(r, t^*)$ with the Gaussian approximation $G_s^G(r, t^*)$ (equation (72)) at $T = 0.46$. $t^* = 109$ is the time at which α_2 is maximum (figure 21). Two vertical dotted lines at $r_l = \sqrt{6} r_{sc} = 0.2337$ and $r^* \approx 0.6$ are shown. Compared to $G_s^G(r, t^*)$, the real dynamics of the cold melt favours displacements that are either smaller than r_l or larger than r^*. While r^* serves as a threshold for choosing mobile monomers (having $r \geqslant r^*$), the enhanced probability, relative to $G_s^G(r, t^*)$, of finding $r < r_l$ illustrates the difficulty a monomer has in exceeding the distance r_l (see the discussion under the heading 'Theory' in section 3.3.5). The latter feature was also nicely demonstrated for a binary LJ mixture by means of an analysis of mean first passage times [202].

String-like motion and clusters of mobile particles. Figure 22 reveals that, even at t^*, the majority of the monomers has moved less than 10% of their diameter—they are effectively jammed. In a melt, whose density is ~1 (no free space) and in which most monomers move very little, large displacements, comparable to the monomer size, can only occur if these mobile particles are close in space and assist their neighbours when they attempt to move ('dynamic facilitation' [203–205]). We thus expect to find clustering and spatially correlated motion of mobile monomers in the late β/early α regime. This expectation is borne out. Here we provide a brief survey of these dynamic features, focusing on 'string-like' displacements and clusters of mobile particles. Further details may be found in [62, 66, 194] (see also [192] for a comparative review of dynamic heterogeneities in model glass-forming liquids and polymer melts).

'Clusters' are defined as aggregates of mobile monomers that reside in each other's first-neighbour shells—the first-neighbour shell comprises all monomers within the distance of the first minimum of the pair distribution function ($r = 1.5$; figure 10) [194]. Work on glass-forming binary LJ mixtures [196, 197] further reveals that the clusters are composed of smaller objects called 'strings'. The strings are quasi-one-dimensional paths formed by mobile particles that replace one another as they move. To decide whether monomer i forms a string with monomer j we employ the following criterion [66]:

$$i = \arg \min_{\{i \mid |\boldsymbol{r}_j(t) - \boldsymbol{r}_i(0)| < \delta\}} \big[|\boldsymbol{r}_j(t) - \boldsymbol{r}_i(0)| \big]. \tag{74}$$

That is, i forms a string with j if the position of j at time t ($\boldsymbol{r}_j(t)$) is within a radius δ of the initial position of i ($\boldsymbol{r}_i(0)$) and furthermore if $|\boldsymbol{r}_j(t) - \boldsymbol{r}_i(0)|$ is the shortest of the distances of all monomers i which also satisfy the δ criterion. In practical applications, we mostly choose $\delta = 0.55$; all results to be presented employ this choice (see [66] for a fuller discussion).

It may be evident that neither the strings nor the clusters are monodisperse. At any time and temperature one should expect a distribution of string and cluster sizes. Let $P_{\text{str}}(s(t))$ denote the probability of finding a string of s monomers ('string length') at time t. Similarly, $P_{\text{clu}}(n(t))$ denotes the probability of finding a cluster comprising n monomers at time t. From these probability distributions different averages may be calculated. For the strings, it was mainly the number-averaged string length $\langle s(t)\rangle$ that was studied [66], for the clusters, the weight-averaged cluster size $\langle n(t)\rangle_{\mathrm{w}}$ [194]. These averages are defined by

$$\big\langle s(t)\big\rangle = \sum_{s=1}^{\infty} s(t) P_{\mathrm{str}}(s(t)) \qquad \text{and} \qquad \big\langle n(t)\big\rangle_{\mathrm{w}} = \frac{\sum_{n=1}^{\infty} n(t)^2 P_{\mathrm{clu}}(n(t))}{\sum_{n=1}^{\infty} n(t) P_{\mathrm{clu}}(n(t))}. \tag{75}$$

These quantities serve to characterize the transient nature of the strings or clusters at temperature T.

Figure 21(c) depicts $\langle s(t)\rangle$ and $\langle n(t)\rangle_{\mathrm{w}}$ at $T = 0.46$. Qualitatively, the two quantities behave in the same way. They 'grow' and 'shrink' as t increases, exhibiting a maximum for times close to t^*. This demonstrates that temporary clustering and string-like processes of replacement of mobile monomers develop in the β regime and are most prominent when the monomers begin, on average, to leave their cages.

The possibility of string-like motion was suggested at the end of section 3.3.2; its extent, however, could not be quantified there. Here we see that the average string length is small. At $t_{\mathrm{str}}^{\mathrm{max}}$ when the strings reach their maximum size (figure 21), we find $\langle s(t_{\mathrm{str}}^{\mathrm{max}})\rangle \approx 1.9$; the corresponding weight average is $\langle s(t_{\mathrm{str}}^{\mathrm{max}})\rangle_{\mathrm{w}} \approx 3$ [66]. Typically, one monomer thus replaces one of its mobile neighbours.

A major contribution to this correlated motion results from chain connectivity. Figure 23(a) illustrates this point. The figure shows the temperature dependence of the ratio $\langle s_{\mathrm{seg}}(t_{\mathrm{str}}^{\mathrm{max}})\rangle / \langle s(t_{\mathrm{str}}^{\mathrm{max}})\rangle$, where $\langle s_{\mathrm{seg}}(t_{\mathrm{str}}^{\mathrm{max}})\rangle$ is the number-averaged string length of contiguous segments of mobile monomers in a chain at time $t_{\mathrm{str}}^{\mathrm{max}}$. Although this ratio decreases on cooling, suggesting that replacements by nonbonded neighbours become more frequent, we find that near T_{c} still about 70% of all strings consist of contiguous segments of mobile monomers along the backbone of a chain. Clearly, a monomer tends to replace one of its bonded neighbours. But this does not imply that mobility is localized on a few chains. If this was the case, $\langle s_{\mathrm{seg}}\rangle$ should be of the order of N; yet, it is much smaller. We find $\langle s_{\mathrm{seg}}(t_{\mathrm{str}}^{\mathrm{max}})\rangle \approx 1.3$. This excludes a relaxation scenario in which mobile monomers are connected to each other and slide along the chain backbone.

The aforementioned difference between the number average $\langle s(t_{\mathrm{str}}^{\mathrm{max}})\rangle$ and the weight average $\langle s(t_{\mathrm{str}}^{\mathrm{max}})\rangle_{\mathrm{w}}$ points to a polydispersity of the strings; we expect to find a (broad) distribution of string lengths. Figure 23(a) depicts the probability distribution $P_{\mathrm{str}}(s)$ of finding strings of length s at time $t_{\mathrm{str}}^{\mathrm{max}}(T)$ for different temperatures. While most strings are of modest size, irrespective of T, large strings become more frequent as T approaches T_{c} from above. The large s behaviour of $P_{\mathrm{str}}(s)$ is well approximated by an exponential

$$P_{\mathrm{str}}(s) \sim \frac{1}{\langle s\rangle} \exp\left(-\frac{s}{\langle s\rangle}\right). \tag{76}$$

This exponential form suggests an analogy, first proposed in [196], between strings and equilibrium polymers (for a discussion of equilibrium polymers see e.g. [206, 207]). Equilibrium polymers are systems in which the bonds between monomers are not stable. At any instant, they may cleave and reform reversibly, allowing the polymers to self-assemble into chains of different length. In chemical equilibrium, a melt of these self-assembling polymers has an exponential distribution of chain lengths (provided that the chains are large) [206, 207]. Coming back to our case, the mobile monomers also self-assemble into (small) chains and the dynamically created bonds can break and recombine at any instant. This similarity to equilibrium polymers may rationalize our finding that $P_{\mathrm{str}}(s)$ is close to an exponential [66].

In contrast to $P_{\mathrm{str}}(s)$, the probability $P_{\mathrm{clu}}(n)$ of finding a cluster of n mobile monomers is not exponential. Figure 23 shows $P_{\mathrm{clu}}(n)$ at time $t_{\mathrm{clu}}^{\mathrm{max}}$ when $\langle n(t)\rangle_{\mathrm{w}}$ is maximum (cf figure 21).

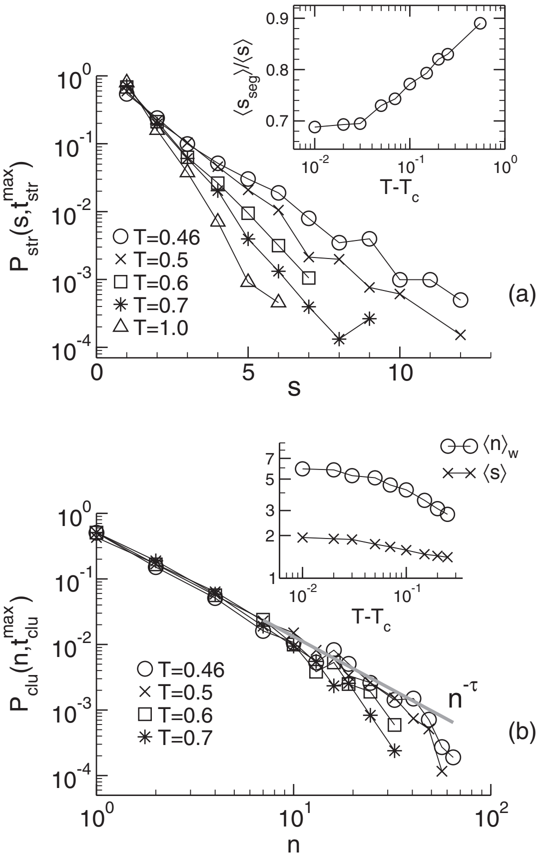

Figure 23. Probability distributions of the string length $P_{\mathrm{str}}(s)$ (a) and of the cluster size $P_{\mathrm{clu}}(n)$ for different T. $P_{\mathrm{str}}(s)$ and $P_{\mathrm{clu}}(n)$ are calculated at the times $t_{\mathrm{str}}^{\mathrm{max}}$ and $t_{\mathrm{clu}}^{\mathrm{max}}$ where $\langle s\rangle$ and $\langle n\rangle_{\mathrm{w}}$ respectively are maximum (cf figure 21). In panel (b), the solid (grey) line shows a power law fit $P_{\mathrm{clu}}(n) \sim n^{-\tau}$ with $\tau = 1.62$. The inset of panel (a) shows the ratio $\langle s_{\mathrm{seg}}(t_{\mathrm{str}}^{\mathrm{max}})\rangle/\langle s(t_{\mathrm{str}}^{\mathrm{max}})\rangle$ versus $T - T_{\mathrm{c}}$. ($\langle s_{\mathrm{seg}}\rangle$ is the mean string length of contiguous segments of mobile monomers in a chain.) The inset of panel (b) compares the T dependences of $\langle s(t_{\mathrm{str}}^{\mathrm{max}})\rangle$ and $\langle n(t_{\mathrm{clu}}^{\mathrm{max}})\rangle_{\mathrm{w}}$. The data for $P_{\mathrm{clu}}(n)$ and $\langle n\rangle_{\mathrm{w}}$ are taken from [194] (reproduced with permission). Part (a) is adapted from [66].

On cooling toward T_{c} large clusters appear more frequently, and the cluster size distribution is apparently well described by a power law, possibly supplemented by an exponential cut-off [194]

$$P_{\mathrm{clu}}(n) \sim \frac{1}{n^{\tau}} \exp\left(-\frac{n}{n_0(T)}\right) \qquad (\text{with } \tau \approx 1.62). \tag{77}$$

The exponential cut-off may be due to finite size effects; the largest clusters comprise $n \approx 65$ monomers, i.e., roughly 6.5% of the total number of monomers in the simulation box (see [194] for further discussion of this issue).

Summary and discussion. The analysis presented above deploys a filtering technique to select at any time and temperature the most mobile monomers and explores their spatial correlations. In the temperature regime above T_{c}, where the two-step relaxation clearly emerges ($0.46 \leqslant T \lesssim 0.7$; cf section 3.3), we find the following results:

(i) Mobile monomers form clusters and tend to follow each other in quasi-one-dimensional paths ('strings').

(ii) Different monomers can be mobile at different times [66]; there is thus no permanent 'phase separation' between regions of high and low mobility.

(iii) Thus, spatial correlations between mobile monomers are a dynamic phenomenon. They develop in the β regime, are most pronounced for times when the monomers, on average, leave their nearest neighbour cages and disappear again on approaching the diffusive regime. In the late β/early α regime the clustering of mobile monomers and string-like motion is not dominated by an enhanced mobility of the chain ends [66, 194].

(iv) The average cluster and string sizes are small, not exceeding a few monomers. On the other hand, these dynamically formed aggregates are fairly polydisperse; large clusters or strings appear, albeit with low probability[22]. Because the largest clusters observed are comparable in size to the total number of mobile monomers, finite size effects cannot be excluded [194]. Whether the truncation of the largest clusters by the system size really perturbs the structural relaxation of the glass-forming melt is not clear. Work on binary LJ mixtures suggests that a system of about 65 particles already exhibits bulk-like diffusion [208]. The truncation in such a small system will be much more pronounced (for further discussion of this issue see [209]). Furthermore, a study of a one-component glass-forming liquid employing a simulation box which is about three times larger than our system confirms the results found here [210].

(v) Mobile monomers tend to replace their bonded mobile neighbours. Chain connectivity in our model thus provides a pathway, not present in simple glass-forming liquids, for string-like motion. However, this polymer-specific spatial correlation is of short range. It does not lead to a 'mobilization' of whole chains, i.e., to a sliding of the monomers along the chain backbone, at least for $T \gtrsim T_c$.

Critique of the analysis. There is much to commend an analysis of spatially heterogeneous dynamics in focusing on highly mobile particles: it is conceptually simple; it is versatile—it may be implemented for any (simulated) structural glass former; and it is instructive. In addition to our polymer model, this analysis and variants thereof have been applied to binary LJ mixtures [195–197, 209], a glass-forming one-component liquid [210] and a model silica melt [211, 212]. Nevertheless the analysis appears less than ideal in at least two respects. We discuss them in turn.

First, it focuses on the most mobile particles. These particles only represent a small fraction, typically about 6%, of the total number of particles present. What are the features of the remaining 'slow' particles? This question was addressed through different approaches for several model glass-forming liquids above T_c [197, 213–215]. We do not attempt to be exhaustive here in presenting the results of these studies. We rather discuss one example.

For a binary LJ mixture, Donati *et al* explored spatial correlations between the 5% least mobile particles—those with the smallest displacement in time t—in a manner analogous to the analysis described above [192, 197]. The least mobile particles also cluster. The structure

---

[22] A detailed analysis of the mechanism of string-like motion was performed for a one-component glass-forming liquid in which the particles interact via the Dzugutov potential [210]. The main finding of this work is that it would be oversimplified to visualize every string-like motion as a coherent replacement process in which all particles move simultaneously. Such a coherent replacement typically occurs only in small strings or in subunits ('microstrings') of large strings. This cooperative motion is thus limited to small length scales. For these large, noncoherent strings, individual mobile particles or microstrings trigger the motion of other parts of the string. However, for most of these noncoherent strings, this 'dynamic facilitation' does not occur in a sequential, but rather in a random fashion: an ordered sequence of replacements is disrupted by one or more particles.

of these clusters is more compact compared to that of the mobile ones, their size is essentially T independent and the probability of finding an immobile particle close to a mobile one is depressed with respect to static pair distribution function ('correlation hole'). No obvious correlation between these slow particles and the local density was found. There appears, however, to be a correlation between the mobility of the particles and their potential energy, large potential energy being associated with higher mobility.

The connection between the structural relaxation and the potential energy—more precisely the potential energy landscape (PEL)—was investigated also for a binary LJ mixture by Büchner and Heuer [213]. At low T the system may temporarily reside in the basin of attraction of a few, adjacent minima of the PEL (cf appendix B). While visiting these minima over and over again, relaxation is slow; it becomes fast if the system is not restricted to such a valley of adjacent minima. The macroscopically observed dynamics of the system results from the time average along this trajectory through configuration space.

There is a second issue of our analysis, which may appear problematic. The analysis hinges on the identification of a suitable fraction of mobile particles. There is some latitude in the definitions of what a 'suitable fraction' (typically 5%–8% [194]), a 'mobile particle' (see e.g. [197]) and a 'string' [66] really are. This freedom may be undesirable. It would thus be advantageous to avoid the filtering of kinetic subensemble and to look for an alternative, ensemble-averaged diagnostic of dynamic heterogeneities. Experiments suggest that higher order correlation functions should be employed for this purpose [190, 193, 217]. An example is provided by the following 'displacement–displacement' correlation function:

$$g_u(\boldsymbol{r},t) = \frac{1}{\langle \mu_i(t)\rangle^2 \rho_{\mathrm{m}} M} \left\langle \sum_{i=1}^{M} \sum_{i\neq j}^{M} \mu_i(t)\,\mu_j(t)\,\delta\big(\boldsymbol{r} - [\boldsymbol{r}_j(0) - \boldsymbol{r}_i(0)]\big)\right\rangle, \tag{78}$$

where $\mu_i(t) = |\boldsymbol{r}_i(t) - \boldsymbol{r}_i(0)|$ is the scalar displacement of monomer i in time t and $\rho_{\mathrm{m}} = M/V$ $(M = nN)$ the monomer density (equation (7)). This function depends on four 'points' of information—the initial positions of monomers i and j, and their locations at time t; $g_u(\boldsymbol{r},t)$ measures spatial correlations between the displacements of two particles which are initially a distance r apart. Such displacement correlations were studied in binary LJ mixtures [216, 218], in hard sphere and hard disk systems [219] and in our polymer melt [62] (for related work see also [220]). At early and late times the displacements of monomers i and j should decouple. One then expects $g_u(r,t)$ to agree with the pair distribution function $g(r)$. However, it would be consistent with the previous results if a pronounced coupling of displacements occurred when the monomers break out of their cages. This is indeed observed [62]. As T_{c} is approached on cooling, a growing range of correlation can be detected in the monomer motion. The extent of these correlations depends strongly on time; it is most pronounced in the late β/early α regime where $g_u(\boldsymbol{r},t)$ is distinctly larger than $g(r)$ for distances up to several monomer diameters (cf figure 24).

Functions similar to $g_u(\boldsymbol{r},t)$, replacing the particle displacements by particle overlap [215] or density fluctuations [205], have recently been discussed.

4. Modelling the glass transition of polymer films

4.1. Introduction

A long-standing conjecture of the research on glasses is that the vitrification process is caused by the growth of a correlation length ξ_{g}. ξ_{g} is supposed to measure—according to Adam and Gibbs [221]—the average size of a subensemble whose constituent particles can rearrange into

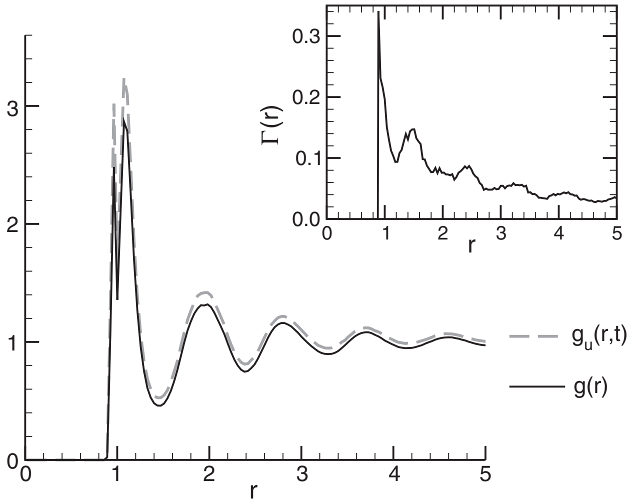

Figure 24. Displacement–displacement correlation function $g_u(r, t)$ and pair distribution function $g(r)$ versus r at $T = 0.47$ and $t = 277.76$. This time corresponds to the late β/early α regime (see e.g. [66]). The inset shows the excess correlation $\Gamma(r) = [g_u(r, t)/g(r)] - 1$ versus r. Apparently, $\Gamma(r)$ does not tend to 0 if r approaches half of the box size ($r \to 5$); it does so, however, for the larger system (binary LJ mixture) studied in [216]. Thus, finite size effects cannot be excluded in the present case [194]. This figure is adapted from [62].

a new configuration independently of the other particles surrounding them. Adam and Gibbs referred to this subensemble as a 'cooperatively rearranging region (CRR)'.

In modern terms, this conjecture may be supported as follows [19]: at low T, most particles are 'caged' and mobility is sparse. A substantial rearrangement of particles—prerequisite to the α relaxation—can only occur if a particle that moves at some time due to a thermal fluctuation assists its neighbours to become mobile; the neighbours assist their neighbours in their motion; and so on until particles are encountered whose motion cannot be (fully) excited. This 'dynamic facilitation' [203–205] naturally leads to the concept of a CRR. A CRR may be viewed as a subensemble of particles over which mobility spreads on the timescale of the α process. As the α timescale increases on cooling toward T_g, the average size ξ_g of the CRR should grow along with that, attaining a few nanometres at T_g (cf e.g. figure 2.15g of [19]).

Study of glass formers in spatial confinement: expectations and complications. An appealing approach to evidencing the existence of the CRRs and estimating their size appears to lie in the study of the glass transition in spatial confinement. If there really is a correlation length which grows on approaching T_g from above, it should be truncated by the finite dimension of the confinement; and this should entail a faster dynamics compared to that of the bulk [19].

This perspective—in addition to the increasing technological interest in nanoscale materials—can account for much of the recent activity in the research on geometrically confined glass-forming systems [222, 223]. Numerous experiments [103, 104, 126, 224–252], computer simulations [70–73, 94, 253–272] and theoretical approaches [273–281] have been deployed to reveal the phenomenology and the underlying mechanism of the glass transition in spatially confined liquids. The systems investigated range from simple liquids [94, 230, 266–268, 270, 272], over molecular and hydrogen-bonded liquids [126, 224–229, 269, 271] to silica [265] and polymers

[70–73, 103, 104, 231–264, 273, 274, 277, 279–281]. The geometries considered involve three-dimensional cavities [228], pores [126, 224–229, 244, 245, 266, 269, 271, 281], nanosized fillers embedded in glass-forming liquids [254, 255, 268] and thin films [70–73, 94, 103, 104, 230–243, 246–253, 256–265, 267, 270, 272–281]. These results have been the subject of recent topical reviews, either with a particular focus on polymer films [104, 282] or providing a comprehensive overview of the field [283].

The broad-brush picture emerging from these studies is that the state of affairs is more complicated than expected (or hoped). Glass formers confined to nanoscopic dimensions display features which differ from the corresponding bulk behaviour not only due to spatial restrictions, but also—and very often mostly—due to interfacial effects. These interfacial effects may have different contributions. We mention three of them (for a fuller discussion see e.g. [19, 283]):

- *Interaction effects.* It is natural to expect strong attractive particle–substrate interactions to temporarily trap particles close to the confining walls. These particles may partly slow down their neighbours which in turn obstruct the motion of their neighbours and so on. This enables the wall-induced retardation to propagate into the core of the system. As a result T_g should increase, particularly in strong confinement (narrow pores, ultrathin films). Conversely, a vanishing attraction—that is, only repulsive interactions are at play, as is e.g. the case at the polymer–air interface—should lead to a decrease of T_g. The importance of the particle–substrate interaction was recognized early; this has led to a number of studies which aimed at directly exploring this effect, e.g. for thin polymer films (cf the reviews [104, 282, 283]).
- *Impact on structure.* The presence of an interface creates environments for nearby particles, which differ from the local structure present in the bulk. For instance, we may expect monomers located at a polymer–air interface to be more mobile because they feel less steric constraints than a monomer in the bulk. This suggests that not only interfacial interactions, but also structural aspects—modifications of the monomer packing, changes of the local chain conformations [241] etc—may play an important role for the understanding of the (glassy) dynamics in confinement.
- *Density variations.* The density of spatially confined glass formers need not necessarily agree with that of the bulk. For instance, if the density steadily decreased with increasing confinement (and this was the sole effect of the confinement [224, 225]), one would expect to find a depression of T_g. Confinement-induced changes of the density do not seem to be an issue for thin polymer films [103, 283]; the glass transition in pores, however, provides an example where such concerns may arise (see e.g. the careful study of molecular liquids confined in highly regular mesopores [224, 225]).

Our contribution: computer simulations of polymer films. We attempt to contribute to this research by means of simulations of model polymer films. Unlike our earlier Monte Carlo studies of the bond fluctuation lattice model [28], reviewed in [33, 284], our more recent work deployed MD simulations to explore the features of a continuum model, the Bennemann model, spatially confined to a thin film geometry by smooth [70, 71, 73] or rough walls [72] (cf sections 2.2 and 2.3).

This shift in the choice of the model—from the lattice to the spatial continuum—is motivated by two aims: first, to avoid the discretization of space, the fingerprint of which leaks out, especially for local interfacial properties and small film thicknesses; second, to enable simulations at constant (normal) pressure [68, 69] (cf section 2.4) of a model that is well characterized in the bulk (cf section 3).

In the following, we shall be mainly concerned with equilibrium properties of polymer films. For our simulations this limits the temperature regime to $T > T_{\mathrm{c}}(h)$, $T_{\mathrm{c}}(h)$ being the critical temperature of MCT for a film of thickness h. The most extensive body of the data to be presented will deal with the Bennemann model confined between two completely smooth, purely repulsive walls (cf sections 2.2 and 2.3). We will explore film thicknesses ($5 \leqslant h \leqslant 20$) that are larger than the bulk radius of gyration ($R_{\mathrm{g}} \simeq 1.45$). Results for other wall types—crystalline and amorphous (cf section 2.3)—will be briefly discussed and compared with those obtained for the smooth walls at the end of this section.

4.2. Polymer films between smooth walls: static properties

The discussion of section 3 suggests that a thorough knowledge of structural features provides helpful information for analysing the dynamics of polymer melts. Close to a solid interface the structure of the melt can markedly deviate from the behaviour found in the bulk [285]. This is pointed out from analytical approaches (see e.g. [286–293]) and computer simulations of model systems (see e.g. [286, 287, 291–296]; for a survey of older work see e.g. [297]). In this section, we describe the influence of purely repulsive walls (equation (4)) on structural features of the Bennemann model. The presence of a wall breaks the translational symmetry of the system. Two directions may be distinguished: the z direction perpendicular to the wall and the directions parallel to it. We divide our discussion accordingly.

4.2.1. Structure perpendicular to the wall. In contrast to that for the bulk, the monomer density in a film is not constant; it depends on the position $\boldsymbol{r}$ in space. The occurrence of the spatial dependence results from the interplay of the monomer–wall and monomer–monomer interactions (see e.g. [286, 287]).

We may obtain a qualitative understanding of the effect if we appeal to a simpler system: a liquid of identical, pairwise interacting particles in contact with a wall (see e.g. [298] for a detailed analysis of hard sphere systems). For such a system the (exact) first equation of the Yvon–Born–Green (YBG) hierarchy relates the particle density $\rho(\boldsymbol{r})$ at position $\boldsymbol{r}$ to the wall potential $U_{\mathrm{w}}(\boldsymbol{r})$ and the pair interaction $U(|\boldsymbol{r}-\boldsymbol{r}'|)$ via [100, 119]

$$-k_{\mathrm{B}}T\,\nabla_{\boldsymbol{r}}\ln\rho(\boldsymbol{r}) = \nabla_{\boldsymbol{r}}U_{\mathrm{w}}(\boldsymbol{r}) + \int \mathrm{d}^3\boldsymbol{r}'\,\rho(\boldsymbol{r}')g(\boldsymbol{r},\boldsymbol{r}')\,\nabla_{\boldsymbol{r}}U(|\boldsymbol{r}-\boldsymbol{r}'|). \tag{79}$$

This equation expresses the force balance at point $\boldsymbol{r}$ between the thermodynamic force $-k_{\mathrm{B}}T\,\nabla_{\boldsymbol{r}}\ln\rho(\boldsymbol{r})$, the external force due to the wall and the force resulting from the interaction of the tagged particle at $\boldsymbol{r}$ with all other particles in the system. The latter contribution depends on the spatial structure of the inhomogeneous fluid, which is embodied by the pair distribution function $g(\boldsymbol{r},\boldsymbol{r}')$. The term $\rho(\boldsymbol{r}')g(\boldsymbol{r},\boldsymbol{r}')$ is proportional to the probability of finding another particle at $\boldsymbol{r}'$ provided that the tagged particle is at position $\boldsymbol{r}$.

In a homogeneous fluid, $U_{\mathrm{w}}(\boldsymbol{r}) = 0$, and the density is constant. Then, the second term on the rhs of equation (79) vanishes because the interaction forces that the particle at $\boldsymbol{r}$ experiences are radially symmetric and thus compensate one another. However, a full compensation at any $\boldsymbol{r}$ is not possible in a spatially inhomogeneous system; for instance, in a film. Near the wall, there are fewer particles to the left than to the right, implying an imbalance of the interaction forces. An equilibrium of all forces can only be achieved by a spatial variation of the density.

Density profile averaged over all monomers. This mechanism also operates in our polymer model. Figure 25 illustrates the effect for the thickest film ($h = 20$) at various temperatures, ranging from the high T, normal liquid state to the supercooled state of the melt. The figure

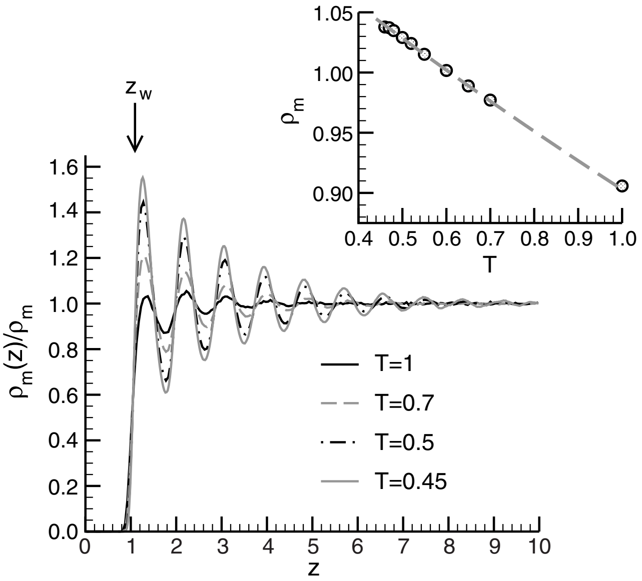

Figure 25. Temperature dependence of the monomer density profile $\rho_m(z)$ for $h = 20$ ($\approx 14R_g$); z is the distance of a monomer from the (left) wall. Since the profile is symmetric with respect to the middle of the film, only one half is shown. z_w denotes the effective position of the wall at $T = 0.45$ (equation (80)). The density profile is normalized by the bulk density $\rho_m(T)$. The T dependence of $\rho_m(T)$ is depicted in the inset for $0.46 \leqslant T \leqslant 1$ ($T_c \simeq 0.45$; cf table 1); the dashed line in the inset indicates the result $\rho_m(T) = 1.1714\exp(-0.2603\,T)$ from [65]. All simulation results refer to the pressure $p = 1$.

depicts the monomer density profile $\rho_m(z)$, i.e., the variation of the monomer density with distance z from the wall. $\rho_m(z)$ vanishes for $z < 1$. The closest distance to which a monomer may approach the wall slightly increases on cooling. We may understand this observation from equation (79). A rough estimate of the distance of closest approach—that is, of the effective wall position z_w—can be obtained if we neglect the interaction term and suppose that $\rho_m(z)$ results only from $U_w(z) = 1/z^9$ (equation (4)). This gives

$$\rho_m(z) = \rho_m \exp\left[-\left(\frac{z_w}{z}\right)^9\right] \qquad \text{with } z_w = T^{-1/9}. \tag{80}$$

While the result for z_w closely agrees with more refined estimates of the wall position, incorporating the interactions between the monomers [68], the monotonically increasing monomer profile predicted by equation (80) is not in accord with the simulation data (see also figure 26). The full force balance leads to density oscillations: there is a high monomer concentration at the wall which, due to the mutual repulsion of the monomers, reduces the density in the adjacent layer; that in turn allows for an enhanced density in the following layer and so on, until the bulk density ρ_m is reached in the centre of the film. The bulk density increases on cooling (inset of figure 25), a consequence of the simulation being carried out at constant pressure. The increase of ρ_m reinforces the packing constraints in the film. This gives rise to an amplification of the oscillations of $\rho_m(z)$ and, along with that, the decay of $\rho_m(z)$ becomes more long ranged.

The qualitative features of $\rho_m(z)$ described are typical of liquids in contact with an impenetrable wall [101, 298]; they are also found in theoretical and computational studies of polymer films [286, 287, 289–291, 293, 296]. A convergence toward the bulk density in

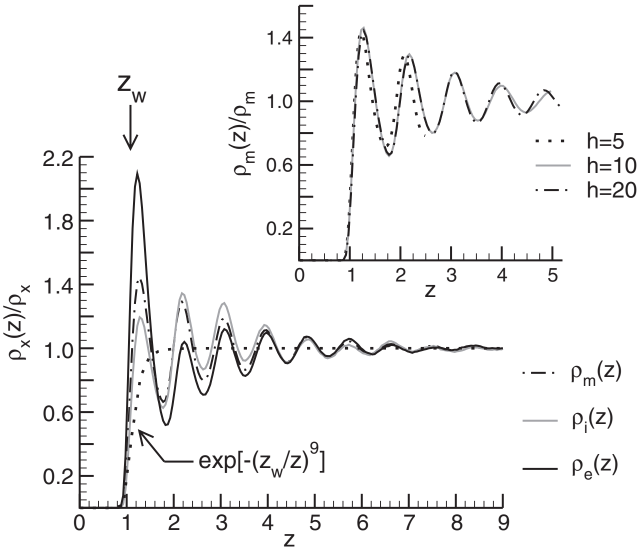

Figure 26. Main figure: various density profiles $\rho_x(z)$ for $h = 20$ at $T = 0.5$. $\rho_m(z)$ is the density profile averaged over all monomers of a chain, $\rho_i(z)$ the profile of the middle monomer and $\rho_e(z)$ the profile of the end monomers. All profiles are divided by the respective bulk density ρ_x ($\rho_m(T = 0.5) = 1.0291$, $\rho_i = \rho_m/N$, $\rho_e = 2\rho_m/N$; $N = 10$). The dotted line indicates equation (80); z_w denotes the effective position of the wall at $T = 0.5$ (equation (80)). Inset: dependence of $\rho_m(z)$ on film thickness h for $T = 0.5$.

the centre of the film can, however, only be observed if the film thickness is large enough [299–302]. Figure 26 illustrates this effect for our model. When $h \lesssim 20$ and $\rho_m \approx 1$, the density oscillations induced by the left and right walls propagate so deeply into the film that they interfere in the middle. No bulk-like region then exists. Despite this interference, the density oscillations close to the wall are only weakly—if at all—affected by the finite film thickness.

Density profiles of end and middle monomers. The density profile $\rho_m(z)$ aggregates contributions from all monomers, irrespective of their specific location along the chain. This averaging procedure levels site-specific differences. Apart from some dependence on chain length that appears to saturate quickly [291, 303], $\rho_m(z)$ essentially resembles the profile of simple liquids. A deeper insight into the conformational characteristics may be obtained by recording density profiles of particular monomers, such as the profile of the end monomers $\rho_e(z)$ or that of the middle monomer $\rho_i(z)$; or that of the centre of mass[23].

Figure 26 depicts $\rho_i(z)$ and $\rho_e(z)$ for $h = 20$ and compares the profiles to $\rho_m(z)$. The hallmarks of $\rho_i(z)$ and $\rho_e(z)$ are that the probability of finding the middle monomer at the wall is suppressed with respect to $\rho_m(z)$, whereas the concentration of end monomers is enhanced. The large value of $\rho_e(z)$ at the wall entails a depression of chain ends compared to $\rho_m(z)$ in the next layer. Conversely, the small value of $\rho_i(z)$ at the wall leads to an enhancement of middle monomers in this layer. The differences of the profiles still persist in the following

---

[23] Here, we do not discuss in detail the profile of the chain's centre of mass (COM). Qualitatively, one expects—and one finds; see e.g. [287] or [297] and references therein—that the COM density vanishes on approaching a repulsive wall. This is because, if a COM is located near the wall, many other monomers are also forced to lie close to it. This strongly restricts the number of configurations that a chain may adopt. The attendant loss of configurational entropy gives rise to a pronounced effective COM–wall repulsion. This idea has recently been substantiated by an analytical determination of the COM profile for an ideal chain [288].

layer, but then become negligible; the oscillations of $\rho_\mathrm{i}(z)$ and $\rho_\mathrm{e}(z)$ converge toward those of $\rho_\mathrm{m}(z)$. An enhancement of chain ends at the wall and a range of the oscillations of $\rho_\mathrm{e}(z)$ identical to that of $\rho_\mathrm{m}(z)$ are commonly found in simulation studies of model polymer films (see e.g. [287, 300, 303]).

4.2.2. Structure parallel to the wall. There are two ways of characterizing structural features parallel to the wall: either by a layerwise resolution of the structure or by determining averages over the film. We shall give examples for both approaches in the following.

Layer-resolved properties: pair distribution functions. Equation (79) suggests that a further key quantity characterizing the structure of the confined polymer melt is the pair distribution function $g(\boldsymbol{r}_1, \boldsymbol{r}_2)$. This function measures the probability of finding a monomer at $\boldsymbol{r}_2$ provided that another monomer is at $\boldsymbol{r}_1$. The planar geometry of the film naturally leads us to distinguish between the z direction perpendicular to the wall and the parallel direction $\boldsymbol{s} = (x, y)$. Parallel to the wall the system is bulk-like. So, only the distance $s = |\boldsymbol{s}_2 - \boldsymbol{s}_1|$ between the monomers is important. Appealing back to the notation of section 3.2 the pair distribution function may then be written as

$$g(s, z_1, z_2) = \frac{1}{A\rho_\mathrm{m}(z_1)\rho_\mathrm{m}(z_2)} \left\langle \sum_{i,j=1}^{n} \sum_{a\neq b}^{N} \delta\big(\boldsymbol{s} - [\boldsymbol{s}_i^a - \boldsymbol{s}_j^b]\big)\, \delta\big(z_1 - z_i^a\big)\delta\big(z_2 - z_j^b\big) \right\rangle, \tag{81}$$

where A denotes the area of the wall and $\boldsymbol{r}_i^a = (\boldsymbol{s}_i^a, z_i^a)$ is the position of monomer a in chain i ($a = 1, \ldots, N$; $i = 1, \ldots, n$). The prefactor in equation (81) guarantees that $g(s, z_1, z_2)$ approaches 1 as $s \to \infty$.[24]

Figure 27(a) presents the influence of the wall, for $h = 10$ and $T = 0.46$, on the pair distribution function for a layer at distance z. As $z_1 = z_2 = z$, we have $s = r$, and so $g(s, z_1, z_2) = g(r, z)$. The figure reveals that, despite the strong structuration in the perpendicular direction, the lateral structure of the melt is—at a qualitative level—only weakly perturbed, even for the layer next to the wall. The pair distribution function has the hallmarks of an amorphous structure: it displays a sequence of peaks whose amplitude rapidly decreases toward 1. This reflects the short range order of the monomers that spatially organize in nearest neighbour shells, as it is typical of the liquid state.

We thus find qualitative agreement between the layer-resolved $g(r, z)$ and the $g(r)$ of the bulk. The agreement can even be quantitative if the layers lie in the centre of the film (cf the inset of figure 27(a)). The layer in contact with the wall, however, displays differences at a quantitative level: the peak at $r = r_\mathrm{b}$ (bonded nearest neighbours) is sharper, that at $r = r_\mathrm{min}$ (nonbonded nearest neighbours) is weaker than in the bulk; and the amplitudes of the following oscillations diminish more rapidly. A further bit of information is provided by figure 27(b). Quite generally, the pair distribution function can be decomposed into intrachain and interchain parts (see e.g. equation (34) for such a decomposition). Figure 27(b) reveals that the peaks at $r = r_\mathrm{min}$ and $r \approx 2$ are largely and those at $r > 2$ fully determined by the interchain part. The depression of these peaks compared to those for the bulk is thus indicative of a weaker intermolecular packing of the monomers near the wall. The intramolecular packing, on the other hand, is enhanced close to the wall.

Averages over the film: static structure factors. The intermolecular packing—more precisely, its reinforcement with decreasing T—has been identified as a driving force for the slow, glass-

---

[24] A detailed analysis of the site-resolved pair distribution function and of related quantities has been presented for hard sphere systems in [298, 386].

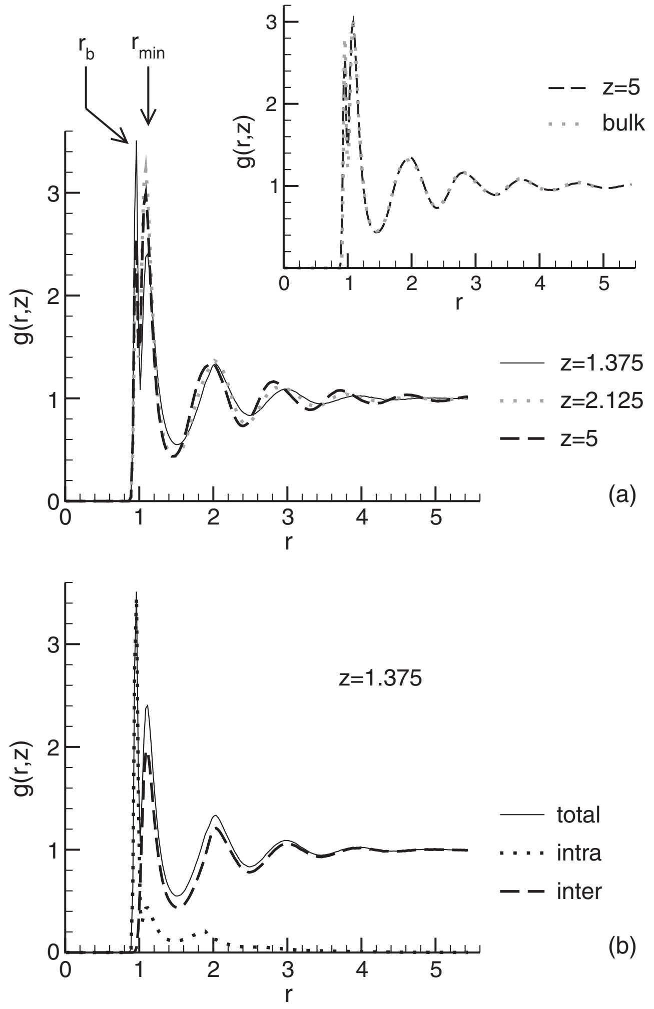

Figure 27. (a) The main figure shows for a film of thickness $h = 10$ at $T = 0.46$ the layer-resolved pair distribution function $g(r, z)$ (equation (81)). z denotes the distance of a monomer from the wall; r is the distance between two monomers in direction parallel to the wall (for $z_1 = z_2 = z$, $r = |\boldsymbol{r}_2 - \boldsymbol{r}_1| = s$ where $\boldsymbol{r}_1 = (\boldsymbol{s}_1, z_1)$ and $\boldsymbol{r}_2 = (\boldsymbol{s}_2, z_2)$; see the text for details). The perpendicular distances $z = 1.375$ and 2.125 are close to the first and second peaks of the monomer density profile $\rho_{\mathrm{m}}(z)$ (cf the inset of figure 26); $z = 5$ corresponds to the centre of the film. The positions of the bond length $r_{\mathrm{b}} \approx 0.97$ and of the minimum of the Lennard-Jones potential $r_{\mathrm{min}} \approx 1.12$ (cf section 2.2) are indicated by arrows. Inset: comparison of $g(r, z)$ for the film centre ($z = 5$) with the bulk $g(r)$ at $T = 0.46$. (b) Comparison for $z = 1.375$ of the total $g(r, z)$ with the intrachain contribution ('$i = j$' in equation (81)) and the interchain contribution ('$i \neq j$' in equation (81)). As in panel (a), $h = 10$ and $T = 0.46$.

like dynamics of our model in the bulk (cf e.g. section 3.3.5). It is thus important to understand how the presence of the walls affects key structural quantities, such as the intrachain structure factor $w(q)$ or the collective structure factor $S(q)$—both averaged over the film.

We exemplify this influence of the walls for $T = 0.46$ in figure 28. The figure compares the bulk results for $w(q)$ and $S(q)$ with the corresponding structure factors obtained in a film of thickness $h = 5$. (For the film, $w(q)$ and $S(q)$ are computed for wavevectors parallel to the wall, i.e., for $\{\boldsymbol{q} = (q_x, q_y, 0) \mid |\boldsymbol{q}| = q\}$.) Two general features, which can also be observed for other h and T, will be highlighted here:

(i) $w(q)$ remains essentially unaltered by the confinement, at least for $q \gtrsim q^*$.[25] On the other hand, the confinement has a pronounced effect on $S(q)$. This implies that it is mainly the intermonomer packing that is affected when moving from the bulk to the thin film geometry.

(ii) The most prominent effect of the confinement on $S(q)$ is that the amplitude of the amorphous halo $S(q^*)$ is depressed with respect to that of the bulk.

These observations are important. The inset of figure 28 reminds us of what is relevant for the glass-like dynamics in the bulk: it is the rise of $S(q)$ in the q range around q^*. This rise reflects the tightening of the intermolecular packing of the monomers with decreasing T (remember that $w(q)$ remains unchanged on cooling; cf section 3.2). The influence of the walls on $S(q)$ thus appears to correspond to the influence that an increase of T has in the bulk. If this correspondence—'decrease of $h \Leftrightarrow$ increase of T in the bulk'—carries over to the dynamics, we should expect the films, for a given temperature, to relax faster than the bulk[26]. We will pursue this idea in the next section.

4.3. Dynamic properties of polymer films

The task of exploring the dynamics of polymer films can be accomplished in the same way as the analysis of the structure. We may introduce quantities which measure the dynamics perpendicular or parallel to the walls. Here, we have chosen to focus on the parallel direction, mainly for the following reason. Motion in the perpendicular direction is restricted by the finite film thickness—its asymptotic long time behaviour can be related to the structure of the film in this direction [71]. By contrast, motion in the parallel direction is not bound, thus allowing for a comparison of the long time dynamics in the film with the corresponding bulk system.

As for the structural features, we organize our presentation by discussing film-averaged and layer-resolved quantities. We begin with the former.

4.3.1. Dynamic properties averaged over the film. Among the convenient quantities for characterizing the dynamics are mean square displacements (MSDs)—for example, the MSD of the middle monomer of a chain:

$$g_1(t) = \left\langle \left[\boldsymbol{r}_{N/2}(t) - \boldsymbol{r}_{N/2}(0)\right]^2 \right\rangle. \tag{82}$$

---

[25] The extent to which confinement influences the intrachain structure factor on larger scales ($q \ll q^*$) and the chain dimension of long polymers has recently attracted a lot of interest (see e.g. [387] (theory), [294, 295] (simulations), [388] (review)). Theory [387] and simulations [294, 295] suggest that there are residual excluded volume interactions in confined melts, which affect the conformational features of the chains, while these interactions only have a (very) weak influence on the radius of gyration measured parallel to the wall—except for ultrathin films ($h \ll R_g$), they lead to deviations from the classical 'Kratky behaviour' for $w(q)$ already in the bulk.

[26] There is a conspicuous qualitative similarity between the influence of confinement in our system and the effect of short range attractions in colloidal suspensions. Hard sphere-like colloidal suspensions can undergo a glass transition if the volume fraction of the particles φ exceeds a critical threshold φ_c. Addition of a weak short range attraction between the particles can shift φ_c to larger values. The counterintuitive finding—attraction impedes instead of favouring glass formation—is interpreted in the following way [364]: compared to the hard sphere case a weak attraction entails a more inhomogeneous cage structure; the average distance between the particles decreases, and concomitantly, the average size of the 'holes' increases. These inhomogeneities are reflected by changes of $S(q)$ close to q^*. The amplitude of the first sharp diffraction peak decreases and the peak becomes broader [120, 366]. From the perspective of MCT these changes are responsible for the shift of φ_c to larger values. The inhomogeneities induced by the walls in our system appear to have a similar effect on $S(q)$ and the dynamics.

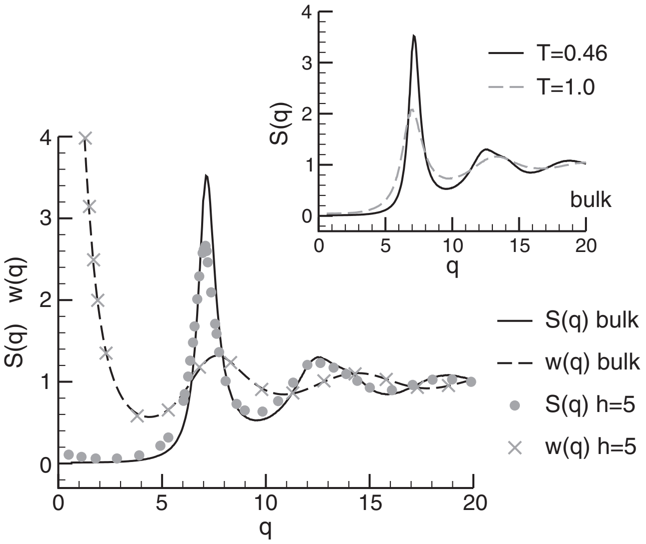

Figure 28. Main figure: collective structure factor $S(q)$ and intrachain structure factor $w(q)$ versus q at $T = 0.46$ for the bulk and a film of thickness $h = 5$. For the film only wavevectors with direction parallel to walls are utilized to calculate $w(q)$ and $S(q)$ (i.e., $\boldsymbol{q} = (q_x, q_y, 0)$). Inset: bulk $S(q)$ for $T = 0.46$ and $T = 1$ (cf figure 5).

In figure 29 we compare $g_1(t)$ for various film thicknesses with the corresponding MSD of the bulk. The temperature $T = 0.46$ is close to the bulk critical temperature of MCT ($T_c \simeq 0.45$; cf table 1). The bulk MSD thus increases in two steps (cf section 3.4): after the short time regime of ballistic motion ($g_1(t) \sim t^2$), there appears first the β relaxation, where $g_1(t)$ is close to the Lindemann localization length r_{sc}, and then the α relaxation in which the monomer escapes from its nearest neighbour cage and eventually crosses over to diffusive motion, $g_1 = 6Dt$ (D is the diffusion coefficient). Final diffusion is preceded by a subdiffusive regime, originating from chain connectivity, where $g_1(t) \sim t^{0.63}$ (cf equation (52)).

This scenario is altered in the films as regards the occurrence of the two-step relaxation. The thinner the film, the more the two-step relaxation disappears and the faster $g_1(t)$ increases. Apparently, a reduction of h at constant temperature has a comparable effect to an increase of T in the bulk (cf the inset of figure 29).

Thus, we arrive again at the conclusion drawn before in the discussion of the static structure factors (cf figure 28). There appears to be the correspondence: 'decrease of $h \Leftrightarrow$ increase of T in the bulk'. If this is really so, how can we then turn this qualitative correspondence into a workable analysis method for quantifying the effect?

One possibility is as follows. We presume that a film of thickness h at temperature T corresponds to a bulk system at a higher temperature T^*. T^* must be higher because the dynamics of the film is faster than that of the bulk at the same temperature T. We can determine T^* by requiring that the film $S(q)$ at T should agree with the bulk $S(q)$ at T^*. The bulk temperature T^* helps us to estimate the critical temperature $T_c(h)$ of the film: T^* is at distance $\Delta T = T^* - T_c$ from the bulk T_c; so we impose $T_c(h) = T - \Delta T$. This determination of $T_c(h)$ amounts to the assumption that the features of the film change in the same way on cooling as those of the bulk; all that the confinement does is delay the building up of the intermolecular packing—and the attendant slowing down of the dynamics—to lower temperatures.

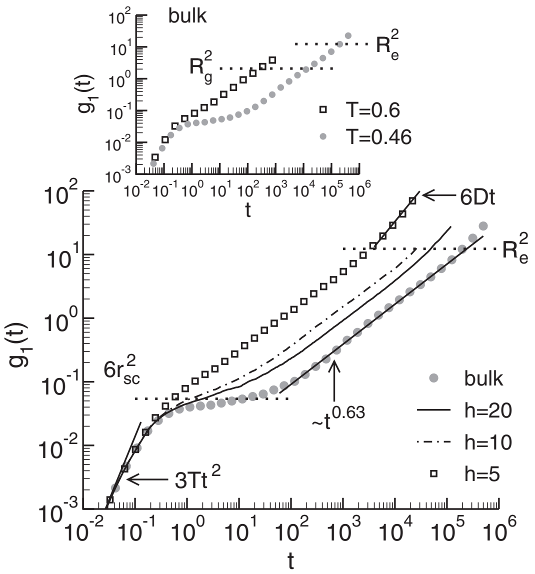

Figure 29. Main figure: mean square displacement $g_1(t)$ of the middle monomer of a chain versus t for the bulk and different film thicknesses h as indicated. The MSDs of the film are measured in the direction parallel to the wall. The film data are multiplied by 3/2 to account for the different numbers of spatial dimensions used in the calculation of $g_1(t)$ (three for the bulk, two for the films). For both the film and the bulk the temperature is $T = 0.46$. The behaviour in the ballistic ($\sim t^2$), the polymer-specific ($\sim t^{0.63}$; cf equation (52)) and the diffusive regimes ($\sim t$) are shown by solid lines. The dotted horizontal lines depict $6r_{sc}^2$ (Lindemann localization length $r_{sc} \simeq 0.095$) and the end-to-end distance R_e^2 (=12.3). Inset: bulk $g_1(t)$ versus t for $T = 0.6$ and $T = 0.46$. The dotted horizontal lines indicate the bulk radius of gyration R_g^2 (= 2.09) and the end-to-end distance R_e^2 (=12.3).

Figure 30 tests this conjecture for two films of thickness $h = 10$ and 20. The analysis presupposes that we can find temperatures for which the structure factor of a film and of the bulk coincide. Figure 30(a) provides an example: the bulk data for $S(q)$ at $T = 0.5$ superimpose on the film results at $T = 0.44$ ($h = 10$) and $T = 0.46$ ($h = 20$).[27] This agreement occurs, according to the argument of the preceding paragraph, because the films and the bulk are at the same distance ΔT from the respective critical temperature. With the bulk values $T^* = 0.5$ and $T_c \simeq 0.45$ we find $\Delta T \simeq 0.05$, and so $T_c(h = 10) \simeq 0.39$ and $T_c(h = 20) \simeq 0.41$.

These estimates for $T_c(h)$ provide important reference points for the analysis of the dynamics. For the same ΔT ($\simeq$0.05, 0.03) figure 30(b) compares $g_1(t)$ of the bulk with $g_1(t)$ of the films so as to test whether the agreement found for the structure also entails agreement of the dynamics. Certainly, measuring temperature relative to $T_c(h)$ is a viable approach. The main differences observed in figure 29 when comparing bulk and film dynamics at the same T are removed and finer details of the time evaluation become apparent. We find good agreement between the bulk and the films in the β regime, particularly in the time window around $g_1(t) \approx 6r_{sc}^2$. In the α regime, however, differences emerge and grow with time. The MSD of the bulk increases faster than $g_1(t)$ for the films. Thus, the time dependence of the film MSDs is more stretched than that of the bulk. Since the film data closely agree with one

---

[27] For the temperatures studied the influence of confinement on the collective structure of the polymer films appears to be weak as long as the film thickness is not too small. Differences between $S(q)$ for the bulk and that for a film occur, for instance, for the smallest film thickness $h = 5$ at low T ($T = 0.35$, i.e., $T - T_c(h) = 0.05$) [71].

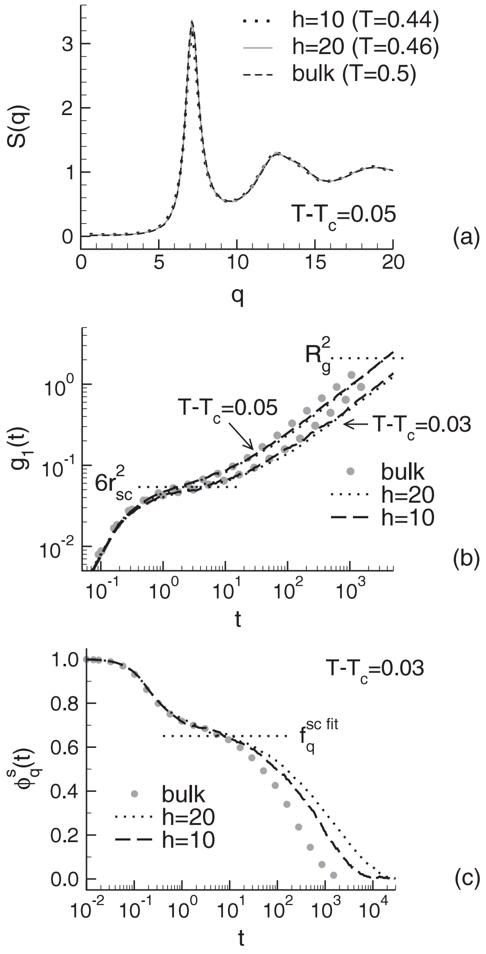

Figure 30. (a) Collective static structure factor $S(q)$ versus q for the bulk and two films of thickness $h = 10$ and 20. The calculation of $S(q)$ for the films only employed wavevectors which are oriented parallel to the walls (cf figure 28). The temperatures for $h = 10$, $h = 20$ and the bulk are different; they are chosen such that the structure factors coincide. The agreement of $S(q)$ establishes a correspondence of the temperature in the bulk and that of the film. Since we know the distance from T_c in the bulk ($T - T_c \simeq 0.5 - 0.45 = 0.05$), this suggests estimating $T_c(h)$ as $T_c(h) \simeq T$ of the film $- 0.05$. This gives $T_c(h = 10) \simeq 0.39$ and $T_c(h = 20) \simeq 0.41$. (b) Log–log plot of $g_1(t)$ versus t for the bulk and the two film thicknesses of (a). The MSDs of the films are measured in the direction parallel to the wall and multiplied by 3/2 (cf figure 29). The MSDs are compared for $T - T_c \simeq 0.05$ and 0.03. In the latter case, $T = 0.48$ (bulk), $T = 0.44$ ($h = 20$) and $T = 0.42$ ($h = 10$). The dotted horizontal lines depict $6r_{sc}^2$ (Lindemann localization length $r_{sc} \simeq 0.095$) and the bulk radius of gyration R_g^2 ($= 2.09$). (c) Incoherent intermediate scattering function $\phi_q^s(t)$ at $q = 6.9$ and $T - T_c = 0.03$ for the bulk and $h = 10$, 20. $f_q^{\text{sc fit}}$ indicates the bulk nonergodicity parameter taken from figure 13. This figure is adapted from [70, 71].

another for all times simulated, the stretching appears to be only weakly affected, if at all, by film thickness.

From what we have said it would seem that confinement has almost no influence on the β relaxation. Differences mainly occur in the late α, connectivity dominated regime before final diffusion sets in. But this conclusion drawn from the MSD does not carry over to the relaxation at larger wavevectors (note that $g_1(t)$ is related to the small q limit of the density correlator $F^{\mathrm{s}}_{ab}(q,t)$ of a single chain; cf equation (69)). Figure 30(c) provides a case in point. It depicts the incoherent intermediate scattering function $\phi^{\mathrm{s}}_q(t)$ (equation (40)) at $q = 6.9$ for the bulk and the same film thicknesses, $h = 10, 20$, as before. Now, differences already emerge in the late β regime between the bulk and the films, and also between films of different thickness, although the data are compared at (about) the same ΔT ($\simeq$0.03). Clearly, the α relaxation in the films is more stretched than in the bulk. But the stretching does not evolve monotonically; the shape of the α relaxation for $h = 10$ is closer to the bulk behaviour than that observed for $h = 20$.

Commentary on the analysis of the results. The previous analysis employed ideas from mode-coupling theory for the bulk. Such an interpretation is motivated by the observation that structural and dynamic properties, averaged over the film, closely resemble the corresponding bulk results. In this sense, the influence of the walls may be considered as 'weak', at least if h is not too small (see footnote 27).

Probably this feature is not specific to our polymer model. Other simulations of glass-forming systems confined by 'weakly' interacting walls also find the dynamic properties of the confined and bulk liquids to be close to one another [254, 255, 267, 268]. On the other hand, if the interaction of the liquid with the walls is strong due to surface roughness or preferential attractions, a qualitatively different relaxation of bulk and confined systems may be expected and is observed [94, 254, 255, 266, 267]; we return to this point in section 4.4.

The overall picture emerging from these simulations is that confinement alters, to a variable extent, the relaxation behaviour of the liquid. It would thus be surprising if it was possible, in our model, to obtain full quantitative agreement between bulk and film dynamics by simply rescaling the temperature axis. Mode-coupling theory—as it was introduced for the bulk in section 3.3.5—would however suggest such an agreement for the following reason. On the T scale relative to $T_{\mathrm{c}}(h)$ the film and the bulk have the same $S(q)$ and $c(q)$—remember that $\rho_{\mathrm{m}}c(q) = w(q)^{-1} - S(q)^{-1}$ (equation (18)) and that $w(q)$ is independent of h in the q regime relevant to MCT (cf figure 28). Two systems with identical structure should display the same relaxation behaviour. Thus, the deviations presented in figures 29(b) and (c) are unexpected.

Perhaps this failure is a reflection of two (naive) assumptions. Firstly, it is not clear whether averaging over the monomer indices is still permissible in the films (cf equations (15) and (60)). The enrichment of chain ends at the wall might lead to pronounced differences between the site-resolved direct correlation function $c_{1a}(q)$ and the averaged $c(q)$, thus invalidating the equivalent-site approximation (equation (15)). Secondly, the dependence of the film properties on the distance from the wall should be accounted for explicitly. More complicated structural quantities, such as the Fourier transform of $g(s, z_1, z_2)$ and the density profile $\rho_{\mathrm{m}}(z)$, could appear in a mode-coupling approach for polymer films.

4.3.2. Thickness dependence of the glass transition temperature. The determination of $T_{\mathrm{c}}(h)$ in the preceding section is appealing in two respects: it is conceptually simple, and it works directly with the simulation data—no fit procedure is involved. Nevertheless, the analysis has a drawback. It is predicated on having simulation data at finely spaced T intervals at hand so as to allow for a precise location of $T_{\mathrm{c}}(h)$. In general, this condition was not fulfilled in our study, not even for the cases $h = 10$ and 20 studied before.

We thus employed another method for refining the estimates of $T_{\mathrm{c}}(h)$ for $h = 10, 20$ or for determining $T_{\mathrm{c}}(h)$ for other thicknesses. We define two relaxation times reflecting the dynamics on two different length scales—more precisely, the dynamics for $q \to 0$ and for the

Table 2. Mode-coupling critical temperature $T_c(h)$ and exponents $\gamma_1(h)$ and $\gamma_{q^*}(h)$ for different film thicknesses h and for the bulk [70, 71]. For the films, $T_c(h)$ and $\gamma_1(h)$ were obtained by fits of the relaxation times τ_1 and $\tau^s_{q^*}$ to equation (84). τ_1 and $\tau^s_{q^*}$ are defined by equation (83). The bulk results are taken from table 1 and [58] (the value for γ_1). The numbers in parentheses give the error bars (i.e. (x) = error in the last digit, (xx) = error in the last two digits). The values for λ are derived from γ_{q^*} by using equation (23) and (24).

h	5	7	10	15	20	Bulk
T_c	0.305(6)	0.365(7)	0.390(5)	0.405(8)	0.415(5)	0.450(5)
γ_1	2.5(2)	2.4(2)	2.1(1)	2.2(1)	2.1(1)	1.95(10)
γ_{q^*}	3.24(8)	3.15(10)	2.68(8)	2.76(10)	2.74(10)	2.09(7)
λ	0.845	0.836	0.776	0.788	0.785	0.635

maximum q^* of $S(q)$: τ_1 is the time it takes the middle monomer of a chain to cover a distance of its own size and $\tau^s_{q^*}$ is the time that $\phi^s_{q^*}(t)$ needs to decay to 0.3. That is,

$$g_1(t = \tau_1) = 1 \qquad \text{and} \qquad \phi^s_{q^*}(t = \tau^s_{q^*}) = 0.3. \tag{83}$$

These times clearly belong to the α regime. Following the analysis performed for the bulk (cf section 3.3.6) we thus attempt a fit to

$$\tau_A(T, h) \propto \left[T - T_c(h)\right]^{-\gamma_A(h)}. \tag{84}$$

This equation needs some comments. (i) It delivers, in addition to $T_c(h)$, the exponent $\gamma_A(h)$. The discussion of figure 30 suggests that both quantities depend on h. (ii) The subscript 'A' on $\gamma_A(h)$ will remind us that the fit result may vary with the quantity A from which the exponent is extracted (see the discussion of section 3.3.6). In particular, we expect $\gamma_1 < \gamma_{q^*}$ (cf figure 19); and this is what we find (cf table 2). (iii) Furthermore, we expect [178]—and find [71]—that the value of $T_c(h)$ is fairly robust. We thus presume the critical temperature to be independent of the analysed quantity A. (iv) Empirically, equation (84) is found to be applicable only in a restricted T interval. Both very close to and far away from T_c, deviations should occur. In practice, we worked with the largest T interval where equation (84) can be applied (cf section 3.3.6).

Table 2 compiles the results of the analysis. It shows that $T_c(h)$ decreases with h and is smaller than the bulk T_c for all film thicknesses studied. This clearly reflects that the average dynamics of the cold melt is speeded up by the imposed confinement.

Moreover, figure 31 suggests that $T_c(h)$ is an important reference point, thereby supporting the observation made before for figure 30(b). Measuring temperature with respect to $T_c(h)$ allows us to superimpose bulk and film data for $T - T_c(h) \gtrsim 0.1$. This facilitates the further comparison between bulk and film. For smaller $T - T_c(h)$, bulk and film dynamics deviate from one another. The relaxation times τ_1 and $\tau^s_{q^*}$ increase less in the bulk than in the film. Appealing back to equation (84), we deduce $\gamma(h) > \gamma(\text{bulk})$. If we then assume that γ is still associated with a von Schweidler exponent b via equation (23), an increase of γ implies a decrease of b, and thus a stronger stretching of the α relaxation when passing from the bulk to the films. This is in qualitative accord with the results of figure 30.

Interpolation: film dynamics and mode-coupling theory. While qualitatively correct, the interpretation based on the MCT prediction (23) appears to fail at a quantitative level. As pointed out above, the results of table 2 suggest that the stretching of the α relaxation increases on decreasing h. Figure 30(c) challenges this prediction. From the figure one would rather conclude that the stretching increases with film thickness. (This qualitative impression is supported by a KWW analysis [71].)

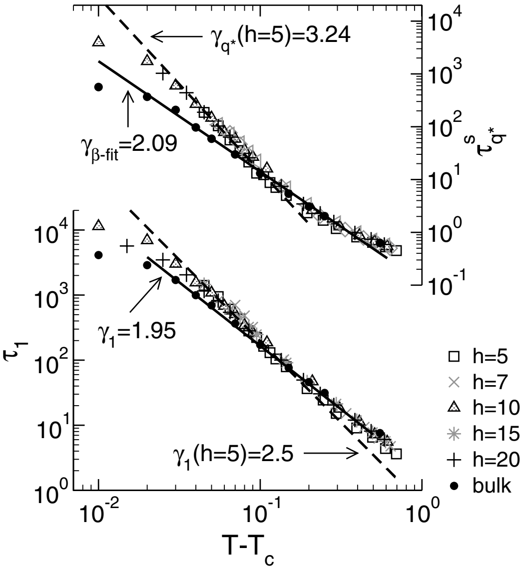

Figure 31. Relaxation times $\tau_1(h)$ (left axis) and $\tau^{\mathrm{s}}_{q^*}(h)$ (right axis) versus $T - T_{\mathrm{c}}(h)$ for all film thicknesses studied and for the bulk. The relaxation times are defined by equation (83). The dashed and the solid lines indicate the exponents $\gamma_A(h)$ for $h = 5$ and for the bulk, respectively. The values of $\gamma_A(h)$ and of $T_{\mathrm{c}}(h)$ are taken from table 2. This figure is adapted from [70, 71].

Should one thus infer that a consistent application of MCT is not possible for our model polymer films? Not necessarily. On the one hand, we have not attempted to carry out a quantitative MCT analysis. This would require extensions of the theory to a film geometry in order to have information on how confinement affects the known bulk results. This information is not available at present. On the other hand, the conclusion from table 2 that the stretching increases with decreasing h is mainly supported by the fit results for $h \leqslant 7$. These results have supposedly the largest systematic errors because the lowest temperatures simulated for $h \leqslant 7$ are much further away from $T_{\mathrm{c}}(h)$ than those for $h \geqslant 10$ (e.g. $T - T_{\mathrm{c}}(h = 5) \simeq 0.045$ while $T - T_{\mathrm{c}}(h = 20) \simeq 0.025$). For $h \leqslant 7$ the simulations should certainly be extended to lower T so as to scrutinize the h dependence of the stretching of the α relaxation close to $T_{\mathrm{c}}(h)$.

The previous discussion dealt with the possibility of a quantitative comparison between MCT and film dynamics. But—as advocated in appendix A—a qualitative analysis should first be carried out to decide whether such an approach can be worthwhile at all. This analysis comprises tests of the factorization theorem for the β process via equation (32) and of the time–temperature superposition principle (TTSP) for the α process via equation (26). We applied these tests to $\phi^{\mathrm{s}}_q(t)$ and found that both the factorization theorem and the TTSP also hold for all film thicknesses studied [71]. This justifies attempting a more quantitative approach within the framework of MCT.

Thickness dependence of $T_{\mathrm{c}}(h)$ *and* $T_{\mathrm{g}}(h)$. We have seen that $T_{\mathrm{c}}(h)$ decreases with film thickness. This simulation result has a laboratory counterpart. In experiments on polystyrene (PS) films, either supported on weakly interacting substrates or freely standing, a depression of the glass transition temperature $T_g(h)$ with film thickness is commonly observed[28]. To a very good approximation, the depression does not depend on the chain length for the supported films, and also for the freely standing films, provided that N is not too large[29].

Furthermore, the experiments hint at an interesting link between the depression of T_g for supported and freely standing films. The glass transition temperature of a freely standing film of thickness h agrees, within the error bars, with the T_g of a supported film of thickness $h/2$ [233–235]. It appears as if the substrate could be introduced in the mid-plane of the freely standing film with negligible perturbation of its properties—at least of those pertinent to the glass transition; all that the substrate does is to cut the film in halves. While there may be concerns about the generality of this result, it still suggests that the T_g reduction of PS films is related to the presence of the free surface which possibly allows for an enhanced mobility of the monomers[30].

This intuitive idea guided the first attempt at modelling the thickness dependence of T_g. In their seminal study, Keddie *et al* [231] proposed

$$T_g(h) = T_g\left[1 - \left(\frac{\overline{h}_0}{h}\right)^{\delta}\right], \tag{85}$$

based on the assumption of the existence of a liquid-like layer at the free surface of supported PS films. The best fit to the measured T_g values was obtained by $\overline{h}_0 = 32$ Å and $\delta = 1.8$. Recently, Long and Lequeux derived equation (85) from a percolation model for the glass transition (see [278] and below).

An alternative parametrization of $T_g(h)$ is given by

$$T_g(h) = \frac{T_g}{1 + h_0/h}. \tag{86}$$

The idea for this ansatz is probably correctly attributed to Kim *et al* [246, 304]. The attractiveness of equation (86) resides in the fact that it depends on one parameter only, h_0. The bulk glass transition temperature T_g can be determined independently. Kim *et al* showed that equation (86) provides a good description of the T_g data for supported films of different homopolymers [246, 304] and may be extended to the glass transition of random copolymer

---

[28] A compilation of results obtained by numerous experimental techniques for PS films of different molecular weight—$1000 < N < 30\,000$—on a variety of substrates—mainly SiO_x wafers—may be found in [104, 282]. The comparison of the data reveals two qualitative trends: T_g decreases with film thickness if $h \lesssim 40$ nm; the decrease depends very weakly, if at all, on N. (Note that there are also accounts in the literature which challenge the generality of these qualitative trends. For example, [389] reports no depression of T_g for PS films on a platinum surface.) While they are qualitatively in agreement—this suggests that the PS films interact only weakly with the underlying substrate—there are quantitative differences between the results. Perhaps these differences are related to the details of the polymer–substrate interaction. An attractive way to remove this influence appears to be the study of freely standing films [104, 282]; but there other complications occur (see footnote 30).

[29] For freely standing PS films, two regimes can be distinguished, a high molecular weight regime and a low molecular weight regime [104, 282]. For low molecular weight ($N \lesssim 3500$), T_g reductions are reported that are qualitatively similar to but stronger than those obtained for supported PS films (see footnote 28). In particular, the reductions are independent of chain length. By contrast, a strong N dependence is found in the high molecular weight regime, i.e. for $N \gtrsim 5750$. This effect is unexpected from the results of the supported PS films. Even if one argues that the findings for PS are specific to this polymer—because a much weaker, though qualitatively similar depression of T_g is found for high molecular weight poly(methyl methacrylate) films [324]—the behaviour of the freely standing PS films appears to be hard to reconcile with the general conception of the glass transition as a phenomenon associated with motion on small length scales.

[30] The presence of the surface certainly engenders a local environment for the monomers which differs from that in the bulk. It appears natural to assume—and there is evidence from simulations [253, 257, 260, 261]—that monomers or chain segments are more mobile when they are in contact with the free surface. One may thus hypothesize that the observed T_g reductions are caused by a liquid-like surface layer [231]. This idea has spurred a variety of recent attempts at exploring experimentally the properties of the free surface and its impact on the T_g of the thin films (see e.g. [232, 233, 237, 250], [390] for another interpretation of the results of [232], and [282, 283] for recent reviews).

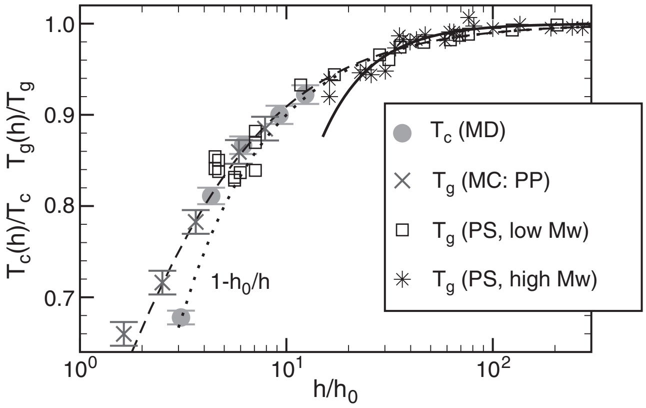

Figure 32. Scaling plot of $T_c(h)$ and $T_g(h)$ according to equation (86). $T_c(h)$ is the critical temperature of MCT for various film thicknesses h (filled circles; $h = 5, 7, 10, 15, 20$; $N = 10$; bulk $T_c = 0.45$ (cf table 1), $h_0 = 1.62$). The data are MD results for the Bennemann model confined between two smooth walls (cf table 2). They are compared to the glass transition temperatures $T_g(h)$ of three studies: (i) Monte Carlo simulations of a lattice model for freely standing atactic polypropylene (PP) films [253] (crosses; $N = 50$; $T_g = 391$ K, $h_0 = 6.1$ Å; 9.95 Å $\leqslant h/2 \leqslant$ 48.1 Å). Both T_g and h_0 are results of a fit to equation (86). (ii) Experiments on supported atactic polystyrene (PS) films (spin cast from toluene solution onto silicon wafers) [235] (open squares; $N \simeq 20$; $T_g = 327$ K = bulk T_g for $N = 20$, $h_0 = 8.2$ Å; 38.5 Å $\leqslant h \leqslant$ 1678 Å). (iii) Experiments on supported, high molecular weight PS films [231] (stars; $N \simeq 290\,00$; $T_g = 375$ K, $h_0 = 6.8$ Å [304]; 110 Å $\leqslant h \leqslant$ 3100 Å). The data of [235, 253] are reproduced with permission. The high molecular weight PS data are reproduced from [104] by courtesy of Forrest. The solid line indicates equation (85) with the parameters mentioned in the text, the dashed line equation (86) and the dotted line the approximation $1 - h_0/h$ to equation (86), valid for small h_0/h.

films [305]. For homopolymers it was found that the parameter h_0 depends on the nature of the polymer (and perhaps also on the monomer–substrate interaction), but is only weakly affected by molecular weight [246, 304].

The latter finding prompted us to apply equation (86) to our simulation results. Except for $h = 5$ (see footnote 26), we find that the thickness dependence of T_c is well described by equation (86) (cf figure 32). The same observation was also made in other studies of short chain polymer films, for instance, in Monte Carlo simulations of freely standing polypropylene (PP) films [253] and in experiments on supported, low molecular weight PS films [235]—the latter work proposes a theoretical derivation of equation (86); we return to it later.

In addition to depending on only one adjustable parameter, equation (86) has a further appealing feature. It suggests a superposition principle. Scaling temperature by the bulk T_g (or T_c) and film thickness by h_0 should allow one to collapse results from experiments and simulations onto a common curve. Figure 32 exemplifies this superposition property. It may be considered as a variant of figure 3 in [304] which includes, besides our $T_c(h)$ data, the simulation results for the PP films from [253] and the glass transition temperatures for nonentangled PS films from the experiments of [235].

The compilation of the data in figure 32 is instructive in several respects. First, it reveals that the simulations typically deal with thicknesses $h \lesssim 10$ nm; the numerical results thus overlap only barely with those of experiments. If one is to realize the goal of obtaining simulation data pertinent to real systems, the study of thicker films would certainly be desirable—but this is a computational challenge at present. Second, the results for the low molecular weight ($R_g = 13$ Å [235]) and high molecular weight ($R_g \simeq 453$ Å [306]) PS films closely agree with one another. Therefore, it seems unlikely that a possible modification of the entanglement density [247, 248] or of the chain conformations [294, 295] in the thin films represents the main cause for the observed T_g depression. Third, for film thicknesses $15 \lesssim h/h_0 \lesssim 300$—a typical range in experiments—one cannot decide whether equation (85) or (86) or the approximation to equation (86), $T_g(h) - T_g \propto 1/h$, provides the more accurate description of the $T_g(h)$ data. On the basis of the T_g shift alone it thus appears hard to validate or rule out theoretical explanations.

It is tempting to add a fourth point. The superposition of different results from experiment and simulation might be seen as evidence that the same microscopic mechanism causes the T_g or T_c reductions. Even if one argues that the polymer–air interface resembles a 'hard wall' and the PS–substrate interaction is weak so that simulations and experiments have qualitatively similar boundary conditions, we feel that the evidence for one mechanism is not sufficient.

The superposition in figure 32 camouflages a crucial difference. The simulation results for T_c are obtained from configurations which are in thermal equilibrium. By contrast, the state of the PS films is a delicate issue (see e.g. [307, 308] and the reviews [282, 283]). These films are commonly produced by a spin coating technique. During spin coating the solvent—typically toluene—quickly evaporates, entailing a freezing in of the polymers when there is still about 14% by mass of toluene left. The film must thus shrink in the glassy state as the remaining solvent is removed. Annealing above the bulk T_g is supposed to achieve this task and to allow the film to attain equilibrium. The extent to which annealing is efficient in eliminating strains and chain distortions, possibly engendered by the spin coating process, is a matter of debate. Therefore, one may wonder whether the T_g reductions are a consequence of the film preparation technique rather than a reflection of the effect of confinement on the glass transition. Such concerns do not seem to have been wholly dispelled [233, 283].

Theoretical approaches to the thickness dependence of T_g. The shift of T_g in polymer films has stimulated attempts to model this phenomenon theoretically [235, 236, 273–281]. We do not set out to be exhaustive here—a more complete overview may be found e.g. in [283]. We focus rather on a few approaches which derive equation (85) or (86), or variants thereof. We explain the underlying assumptions and briefly comment on these theories as we go.

T_g reduction from viscoelastic capillary waves. A continuum model for the shift of T_g in low molecular weight freely standing films or supported films on structureless substrates (slip boundary condition) was proposed by Herminghaus *et al* [235, 236]. The model is based on four assumptions:

- The polymer film is incompressible: density fluctuations can thus be neglected. The important collective variables are strain fluctuations.
- Coupling of capillary waves at the free surfaces to the bulk of the film, which is modelled as a viscoelastic continuum, is suggested as the dominant mechanism for strain relaxation. The strain relaxation is first treated by a linear continuum theory. Two relaxation rates enter here, one for the capillary waves, the other for the film. The rate ω_c associated with the capillary waves is the product of the wavevector q of the (harmonic) surface fluctuations and of the 'capillary speed' γ/η; γ and η are respectively the surface tension and the viscosity of the melt. So we have $\omega_c = \gamma q/\eta$. The relaxation rate ω_f of the viscoelastic film is given by the classical Maxwell expression E/η (E being Young's modulus of the film). Adding the two results gives a q dependent relaxation rate of the film

$$\omega(q) \approx \frac{E}{\eta} + \frac{\gamma q}{\eta}. \tag{87}$$

- Fluctuations of the capillary waves extend into the film up to a distance of order $1/q$. Since the glass transition should reflect the response of the entire film, only one mode, $q = 1/h$, is considered. So we have from equation (87)
$$\omega(h) \approx \frac{E}{\eta}\left[1 + \frac{h_0}{h}\right] \qquad \text{with } h_0 = \frac{\gamma}{E}. \tag{88}$$
- The sketched linear theory does not involve memory effects, an important feature of glass-forming liquids. In the framework of the present model, memory effects should be associated with the strain relaxation. To incorporate them it is argued that a polymer chain is strained, that the chain memorizes its initial state when the strain is released, that the memory kernel scales with temperature as $1/T$ and that this gives rise to the relation $\omega(h)T_\mathrm{g}(h) = \text{constant}$.
  Accepting this line of reasoning we are led to $\omega(h)/\omega_\mathrm{bulk} = T_\mathrm{g}/T_\mathrm{g}(h)$, and so we find, with $\omega_\mathrm{bulk} \approx \omega_\mathrm{f} = E/\eta$,
$$T_\mathrm{g}(h) = \frac{T_\mathrm{g}}{1 + h_0/h} \qquad \text{with } h_0 = \frac{\gamma}{E}, \tag{89}$$
  that is, equation (86).

This derivation of equation (86) certainly raises questions as regards the pertinence of the assumptions made. For instance, the work of [309–312] indicates that the q dependence of the relaxation rate might be more complicated than expected from equation (87). Perhaps a merit of equation (89) is that the weak N dependence discussed in connection with figure 32 naturally appears from the theory. However, such a weak dependence on chain length is also obtained by the other approaches sketched below. It might also emerge e.g. from a liquid state approach, such as mode-coupling theory (here we assume that the resulting predictions for T_c could be qualitatively transferred to the h and N dependence of T_g). This approach would establish a link between the dynamics and the local structure of the polymer films; and the local structure should only depend weakly on N. This and other issues are further discussed in the commentaries [313, 314].

T_g shifts as a consequence of inhomogeneous density profiles. We have seen that an impenetrable wall can lead to an inhomogeneous distribution of the density (cf section 4.2.1). This distinctive feature represents the starting point of a suggestion by McCoy and Curro [274] that the T_g shift of polymer films—and of geometrically confined liquids in general—might be attributed to the impact of confinement on the average density of the glass former.

The line of thought for turning this idea into a prediction for the T_g shift runs as follows. For a film of thickness h we can express the average density $\overline{\rho}_\mathrm{m}(h, T)$ as a sum of two parts: the bulk density $\rho_\mathrm{m}(T)$ and the surface excess $\Gamma(h, T)$. More precisely,
$$\overline{\rho}_\mathrm{m}(h, T) = \rho_\mathrm{m}(T) + \frac{\Gamma(h, T)}{h} \qquad \text{with } \Gamma(h, T) = \int_0^h \mathrm{d}z\,\left[\rho_\mathrm{m}(z) - \rho_\mathrm{m}\right]. \tag{90}$$
The definition of $\Gamma(h, T)$ reveals that the surface excess quantifies deviations of the film density from the bulk value due to the nonuniform density profile of the film. The surface excess can be positive or negative. A positive value reflects the propensity of the liquid to 'wet' the wall, a negative value that to avoid it. Thus, $\overline{\rho}_\mathrm{m}(h, T)$ may be larger or smaller than ρ_m at the same T.

This observation is the basis of the theory of McCoy and Curro. They hypothesize that the difference of density between bulk and film induces a shift of T_g. For large h, i.e. for small differences $T_\mathrm{g}(h) - T_\mathrm{g}$, one may write
$$T_\mathrm{g}(h) = T_\mathrm{g} + \left.\frac{\mathrm{d}T_\mathrm{g}}{\mathrm{d}\rho_\mathrm{m}}\right|_p \left[\overline{\rho}_\mathrm{m}(h, T_\mathrm{g}) - \rho_\mathrm{m}(T_\mathrm{g})\right] \simeq T_\mathrm{g}\left[1 + \frac{\tilde{h}_0}{h}\right], \tag{91}$$

where

$$\tilde{h}_0 = \frac{1}{T_\mathrm{g}} \frac{\mathrm{d}T_\mathrm{g}}{\mathrm{d}\rho_\mathrm{m}}\bigg|_p \Gamma(T_\mathrm{g}) \qquad \text{with } \Gamma(T_\mathrm{g}) = \Gamma(h \to \infty, T_\mathrm{g}). \tag{92}$$

Depending on the sign of the surface excess, the characteristic thickness $\tilde{h}_0$—and along with that, the shift of T_g—can be positive or negative.

An alternative derivation of equations (91) and (92) has recently been obtained by exploring the potential energy landscape (PEL) of a soft sphere/mean field (SSMF) model for confined simple glass formers [275, 276]. This model consists of a fluid containing N spherical particles that are embedded between two parallel substrates. The particles interact through a soft sphere potential ($\sim 1/r^n$) in addition to attractions that are treated at a mean field level. Through an analysis of the configurational entropy associated with the number of potential energy minima of a given depth (inherent structures; cf appendix B) an ideal glass transition is identified with the temperature $T_\mathrm{g}^\mathrm{IG}(h)$ at which the configurational entropy vanishes. The ideal glass transition is a consequence of the repulsive interactions in this model; it is related to the density of the confined liquid by

$$\overline{\rho}_\mathrm{m}(h) T_\mathrm{g}^\mathrm{IG}(h)^{-3/n} = \mathrm{const}(h). \tag{93}$$

From this relation a T_g shift consistent with equations (91) and (92) can be derived via a perturbation approach that is valid to first order in $1/h$ (see [275, 276] for a comparative discussion of the PEL approach and the theory of McCoy and Curro, and [276] for a detailed interpretation of properties of thin films from a PEL perspective).

Density may be a factor contributing to the shift of T_g in thin films [315]. But a one–one mapping between changes in density and T_g appears too simplified. This explanation requires that the average density in the film is different from the bulk value (equation (90)), a situation not necessarily encountered in experiments on thin PS films where T_g shifts are observed (see e.g. [103]). Furthermore, recent simulation results obtained by Scheidler *et al* [94, 267] also raise reservations. In this work, a binary LJ liquid is confined between two rough amorphous walls whose features are adapted to those of the liquid. Scheidler *et al* report that the structural properties of the confined liquid—in particular the density—are identical to those of the bulk system. Nevertheless, the confinement strongly affects the dynamics. The walls slow the relaxation, which should ultimately entail an increase of T_g (see [94] for a fuller discussion).

T_g shift and a model for spatially heterogeneous dynamics. The existence of spatially heterogeneous dynamics near T_g has been invoked to explain striking dynamic features of glass-forming liquids and polymer melts (for reviews see [190–193]; cf also section 3.4). For example, the stretched nonexponential relaxation of dynamic correlation functions or the decoupling of transport coefficients could result from this heterogeneity which implies that the dynamics in one region of the supercooled liquid is considerably different (faster or slower) from that in another region. NMR experiments reveal that the size of a (slow) region in polymeric and nonpolymeric glass formers near T_g is typically a few nanometres (1–4 nm; see e.g. [316] and references in [187]).

These experimental observations are the starting point of a mesoscopic model given by Long and co-workers for the glass transition in general [278, 317] and for the glass transition of polymer films in particular [278, 279]. The model is based on four suggestions:

- Dynamic heterogeneity occurs due to the existence of slow domains. Slow domains will result from thermal density fluctuations. It is proposed that these (static) density fluctuations obey a Gaussian distribution $P(\rho, T)$.

It appears plausible to assume that $P(\rho, T)$ is Gaussian because the domains are supposed to be mesoscopic[31]. They should comprise a few tens of monomers. Here, the term 'monomer' does not refer to a chemical monomer, but rather to a Kuhn segment. A domain is thus considered as a subsystem which is sufficiently large that thermodynamic variables, e.g. its density ρ, may be defined. ρ will fluctuate about the average monomer density $\rho_{\mathrm{m}}(T)$ because a domain is an open system exchanging particles with the reservoir provided by the rest of the sample.

- Although $P(\rho, T)$ is sharply peaked at ρ_{m}, there is a finite probability of finding $\rho > \rho_{\mathrm{m}}$. Invoking now a free volume model allows one to establish a link between the density and dynamics of a domain. Domains are assumed to be slow—i.e., they have a lifetime of the order of the timescale associated with the glass transition ($\sim 10^2$ s)—if their density exceeds a critical value ρ_{c}.
- ρ_{c} is defined as the density above which domains with $\rho \geqslant \rho_{\mathrm{c}} > \rho_{\mathrm{m}}(T)$ percolate at T_{g}. More formally,

$$\int_{\rho_{\mathrm{c}}}^{\infty} P(\rho, T_{\mathrm{g}})\, \mathrm{d}\rho = p_{\mathrm{c}}^{3\mathrm{D}}, \tag{94}$$

where $p_{\mathrm{c}}^{3\mathrm{D}}$ denotes the percolation threshold in the bulk.

- Identifying the glass transition with the percolation of mesoscopic, highly viscous domains allows one to predict the shift of T_{g} in a film. Three ingredients are needed. First, the percolation transition is a critical phenomenon. A critical phenomenon possesses universal features, such as the critical exponents. For percolation the critical exponents are independent of the microscopic details of the systems considered and of the type of percolation (site, bond or continuum); they only depend on the dimension of space [318]. One example is the exponent ν characterizing the size ξ of finite clusters (consisting of slow domains) close to $p_{\mathrm{c}}^{3\mathrm{D}}$. The size of the clusters diverges as the critical point is approached from above and below:

$$\xi \sim |p - p_{\mathrm{c}}^{3\mathrm{D}}|^{-\nu} \tag{95}$$

with $\nu \simeq 0.88$ in 3D [318].

Second, the threshold $p_{\mathrm{c}}(h)$ where percolation occurs in a film of thickness h should depend on the film boundary. One may distinguish two cases: (i) neutral or weakly interacting boundaries (e.g. PS films on silicon wafers, freely standing (low molecular weight) PS films [104, 282, 283]); and (ii) strongly interacting boundaries (e.g. PMMA films on silicon oxide [104, 282, 283]). For case (i) percolation of slow domains can only occur in the direction parallel to the film boundaries. The critical system is effectively a two-dimensional one. So one expects, quite generally from the theory of phase transitions in restricted geometry (see e.g. [319, 320]), $p_{\mathrm{c}}(h)$ to shift to larger values with respect to the bulk ones. For films of sufficiently large thickness h [321] the shift should assume the form

$$p_{\mathrm{c}}(h) - p_{\mathrm{c}}^{3\mathrm{D}} \propto \frac{1}{h^{1/\nu}} \qquad \text{(case (i))}. \tag{96}$$

For strongly interacting boundaries (case (ii)), however, it is suggested that the boundaries 'nucleate' percolation of slow domains, so the films should vitrify as soon as $\xi \approx h$. Via equation (95) this implies

$$p_{\mathrm{c}}^{3\mathrm{D}} - p_{\mathrm{c}}(h) \propto \frac{1}{h^{1/\nu}} \qquad \text{(case (ii))}. \tag{97}$$

---

[31] Note that simulations suggest that the distribution of the local volume around a monomer is not Gaussian. The distribution appears to be best fit by a log-normal distribution [323].

Third, equations (94), (96) and (97) provide an implicit expression of the T_g shift in terms of the density. To make the dependence of T_g on h explicit one needs a relation between temperature and density, that is, the equation of state of a polymer film. For this, a van der Waals-like theory is developed. Including this last bit of the model provides us with an expression for the T_g shift,

$$T_g(h) = T_g\left[1 \pm \left(\frac{\overline{h}_\pm}{h}\right)^\delta\right] \qquad (\delta = 1/\nu \simeq 1.13), \tag{98}$$

for both strong and weak interactions with the boundaries. The characteristic thicknesses $\overline{h}_\pm$ scale with the number of monomers N_c in the slow domains as $\overline{h}_\pm \sim N_c^{-(3\nu-2)/6\approx-0.11}$.

For the weakly interacting case, equation (98) agrees with the form proposed by Keddie *et al* (cf equation (85)). The derivation presented has a particular appeal. It predicts that the exponent δ is universal; δ should be the same for all systems and independent of the interaction with the substrate. In practice, this prediction may be hard to verify because δ is close to 1 and a T_g shift proportional to $1/h$ appears compatible with the experimental data (see e.g. the discussion of figure 32; for a recent test of equation (98) see e.g. [322]). From the point of view of simulations another concern may arise. To our knowledge, attempts to reveal correlations between the dynamics and density of clusters of slow particles have failed [192, 197, 323] or remained inconclusive [32]. This may be due to the high temperatures ($T \gtrsim T_c$) typically studied in simulations. Perhaps there is room for progress here if the analysis could be refined.

Final comparison and discussion. After having described in some detail three theoretical approaches for explaining the shift of T_g in confined (polymeric) liquids, it appears appropriate to briefly compare these theories with each other. In this respect, we want to mention three points:

- The T_g shifts derived (equations (89); (91), (92); and (98)) depend only weakly on the molecular weight. The theories should thus apply to the glass transition of supported polymer films and freely standing (PS) films of not too high molecular weight [104, 282, 283].

  The strong dependence of $T_g(h)$ on chain length, observed for freely standing high molecular weight PS films [104, 282] (which is hard to reconcile with the common perception of the glass transition as a local phenomenon), is at present not incorporated in the theories. If the effect is not specific to PS films [324], either additional relaxation mechanisms [273] or other approaches [277] must be considered.
- The main goal of the approaches of Herminghaus *et al* [235, 236] and McCoy and Curro [274] is to model the thickness dependence of T_g. On the other hand, the approach by Long *et al* has a larger scope. It first proposes a mechanism for the glass transition in the bulk [278, 317] and then extends the theory to the glass transition of confined (polymeric) liquids [278, 279]. Comparing to the former two approaches, one finds that the finite size effects in the theory of Long *et al* apparently have an altogether different flavour. They are associated with the truncation of the critical fluctuations of a percolation transition by the system size.

  In the theory of critical phenomena an extensive framework, the theory of finite size scaling (see e.g. [105, 325]), has been developed to deal with these system size dependences. There, finite size effects are not a nuisance, but provide us with a means to reveal the universal features of the phase transition. If we revert to the glass transition and the suggested link with a percolation phenomenon, the question arises of whether finite size effects could not be exploited similarly to test the validity of the theory. This might be an interesting direction for future research (see e.g. [326] and also the discussion at the end of section 4.4).

- The predictions for the shift of T_g depend on the choice of the boundary condition at the polymer–substrate or polymer–air interfaces. Here, (plausible) assumptions were made in the theories—e.g., the polymer–air interface is 'neutral', the polymer–substrate interactions may be 'weak' or 'strong'.
  Given the importance of these assumptions for the direction of the T_g shift it seems worthwhile to seek for a more molecular understanding of the boundary conditions. Such a microscopic approach would be in line with the view—mainly discussed in this article—that the local packing of the particles and its impact on the relaxation is an important ingredient for the description of the dynamics of glass-forming liquids. The goal of modelling the liquid and the boundary condition at the same microscopic level still appears distant, but not completely out of sight; microscopic treatments of the boundary conditions in confined simple liquids have been suggested in the literature (see e.g. [327, 328]). In this respect, the simulation can perhaps provide an element by scrutinizing the local dynamics in layers at different distances from the wall. We want to present such an analysis next.

4.3.3. Layer-resolved dynamics. When trying to extend the layer-resolved analysis of the structure (cf section 4.2) to the dynamics of polymer films the question arises of how local time-displaced correlation functions should be defined. Two prescriptions for such a definition are conceivable:

(i) Let $\boldsymbol{r}_i^a = (\boldsymbol{s}_i^a, z_i^a)$ denote the position of monomer a in a tagged chain i. The first prescription associates a monomer with a bin of width Δz centred at distance z from the wall if its initial z coordinate, $z_i(t_0)$, is located in this bin. Following this definition the layer-resolved mean square displacement, averaged over all monomers, assumes the form

$$g_0(t;z) = \left\langle \frac{\sum_{a=1}^{N} \delta(z - z_i^a(t_0)) \left[\boldsymbol{s}_i^a(t) - \boldsymbol{s}_i^a(t_0)\right]^2}{\sum_{a=1}^{N} \delta(z - z_i^a(t_0))} \right\rangle. \tag{99}$$

There are two main arguments in favour of equation (99): it is conceptually simple, and it can be implemented easily. These are probably the reasons that equation (99) has been utilized in several simulation studies (see e.g. [94, 254, 255, 260, 261, 265–267, 271, 272]). However, there is certainly one respect in which it is not so satisfying. A monomer will eventually leave the layer it was initially in. A prescription which catalogues the monomers only according to their starting point will mix at time t contributions from monomers which are still in the original layer and those that have already left it. Obviously, the probability of escaping from the original layer increases with t. The desired local character of the dynamics will thus be lost for large times. A rough estimate of the threshold beyond which the averaging over neighbouring layers is no longer negligible may be obtained as the time it takes a monomer to cover a distance of $\Delta z/2$ in the direction perpendicular to the wall.

(ii) The analysis can, however, be adapted to ensure locality. We have to impose the constraint that a monomer remains at all times $t_0 \leqslant t' \leqslant t$ in the same layer. For the monomer MSD $g_0(t;z)$ the definition then reads

$$g_0(t;z) = \left\langle \frac{\sum_{a=1}^{N} \prod_{t'=t_0}^{t} \delta(z - z_i^a(t')) \left[\boldsymbol{s}_i^a(t') - \boldsymbol{s}_i^a(t_0)\right]^2}{\sum_{a=1}^{N} \prod_{t'=t_0}^{t} \delta(z - z_i^a(t'))} \right\rangle. \tag{100}$$

> This second prescription also has strengths and weaknesses. It certainly delivers what we require: equation (100) filters out those monomers that persist in a given layer and thereby provides a true diagnostic of local mobility. However, this diagnostic is limited to 'short' times. Since a monomer that has left its initial layer may not be included in the computation of $g_0(t; z)$, and the number of such monomers increases with time, the accuracy of the data deteriorates at long t. This problem cannot be circumvented by increasing the number of independent configurations of the system because in the limit $t \to \infty$, any monomer will have left its initial layer.

A detailed comparison of equations (99) and (100) was carried out in [70] for our model polymer films between smooth walls. Here, we will focus on the second prescription, provide examples of this analysis and also discuss an extension of the simulations to polymer films confined by rough—crystalline or amorphous—walls.

Layer-resolved dynamics: smooth walls. The prescription of equations (99) and (100) for how to obtain information on the local dynamics in specific layers can be applied to any dynamic correlation function; e.g. to different mean square displacements (MSDs) [70], intermediate scattering functions and Rouse modes [71]. (In the latter case—and for other quantities related to the chain relaxation—the layerwise resolution is associated with the z position of the centre of mass of the chains.)

Figure 33 provides representative examples. It displays for $h = 20$ at $T = 0.46$ two layer-resolved dynamic quantities: the MSD $g_0(t, z)$ and the incoherent intermediate scattering function $\phi_q^{\mathrm{s}}(t, z)$ (equation (40)) at $q = 6.9$. Both correlation functions are calculated according to the more stringent condition of equation (100). The data presented in figure 33 confirm a result that one might have expected from the discussion of section 4.3.1. The monomer mobility increases as we go from the centre of the film toward the wall. While there is a clear two-step relaxation—characteristic of the cold melt close to T_{c}—in the centre, this feature is gradually lost on approaching the wall and is absent at the wall[32]. Seemingly, the forces acting on monomers at the wall (monomer–wall and monomer–monomer interactions) are very different from those in the bulk-like centre of the film, and this leads, in the present case, to faster relaxation.

It is tempting to relate this interpretation (about the 'forces') to the local structure of the films. In the centre, the film is homogeneous, as evidenced by the monomer density profile (see the inset of figure 33(a)), its structure is bulk-like (cf figure 27) and so both $g_0(t, z = 9.5)$ and $\phi_q^{\mathrm{s}}(t, z = 9.5)$ agree well with their bulk counterparts. By contrast, a quick look back at figure 27 reminds us that the monomer packing in the layer next to the wall differs from that in the bulk. Certainly the packing is there still liquid-like, but the probability of finding a nonbonded nearest neighbour is reduced relative to that for the bulk, and the pair distribution function is of shorter range. These structural features qualitatively agree with the bulk behaviour, not at $T = 0.46$, but at higher T [63]; and they find a counterpart in the dynamic properties. Both $g_0(t, z = 1.5)$ and $\phi_q^{\mathrm{s}}(t, z = 1.5)$ (figure 33) resemble the corresponding bulk results at temperatures higher than $T = 0.46$ (see e.g. figure 30).

---

[32] An intelligible concern is that the average density in a layer near the wall might be smaller than in the bulk. This could give rise to faster dynamics. This concern may, however, be dispelled. We tested that the results presented in figure 33 are not a consequence of our choice for the layer thickness, $\Delta z = 1$. Qualitatively the same behaviour is obtained for $\Delta z = 0.35$ (however, the statistical accuracy of the data deteriorates much faster than for $\Delta z = 1$). With this choice, for instance, only monomers close to the first peak of the monomer density profile contribute to the layer-resolved mean square displacement. In spite of the high density in that layer—it is larger than the bulk value—we find an accelerated dynamics relative to the bulk.

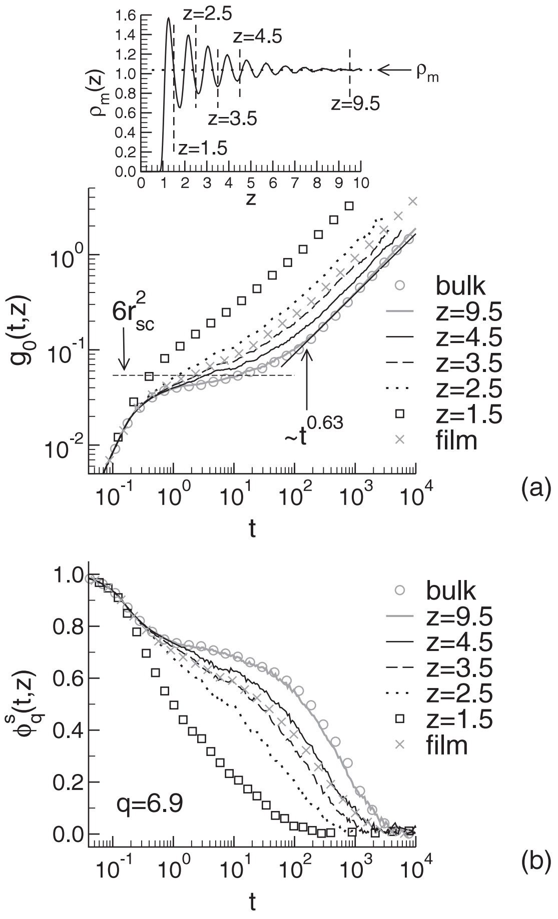

Figure 33. (a) Main figure: layer-resolved mean square displacement (MSD) $g_0(t, z)$, averaged over all monomers of a chain, versus time t for a film of thickness $h = 20$ at $T = 0.46$ ($T_c(h = 20) = 0.415$, $T_c = 0.45$; see table 2). z denotes the distance from the (left) wall. The MSDs are calculated parallel to the wall and multiplied by $3/2$ (to put them on the same scale as the bulk data (•) which are averaged over three spatial dimensions instead of over only two for the film). $g_0(t, z)$ is obtained as an average over all monomers which remain for all times shown in a layer of width $\Delta z = 1$ and centred at z (cf equation (100)). Eventually, monomers will leave the layer in which they were initially. This gives rise to a loss of statistical accuracy at long t; the data are thus sometimes truncated at late times where large statistical noise occurred. The average behaviour of the film (average over all layers) is indicated by crosses (×). The dashed horizontal line depicts $6r_{sc}^2$ ($\simeq 0.054$; the Lindemann localization length of the bulk). The subdiffusive polymer-specific behaviour ($\sim t^{0.63}$; cf equation (52)) is shown by a solid line. Inset: monomer density profile $\rho_m(z)$ versus z for $h = 20$ and $T = 0.46$. The centres of the layer for which $g_0(t, z)$ is shown in the main figure are indicated. The dotted horizontal line depicts the bulk density $\rho_m = 1.038$. This figure is adapted from [70]. (b) Layer-resolved incoherent intermediate scattering function $\phi_q^s(t, z)$ at $q = 6.9$ ($\approx$ maximum of $S(q)$; cf figure 30) and $T = 0.46$ for $h = 20$; the symbols and lines are the same as for the main part of (a).

This structure–dynamics correlation at the wall (the 'boundary condition') seems to fuel—in the present case of smooth walls—a form of continuous tempering: 'fast' monomers at the wall transfer part of their impetus to monomers in the adjacent layer, which in turn partly excite a high monomer mobility in the next deeper layer and so on until the wall-induced stimulus is

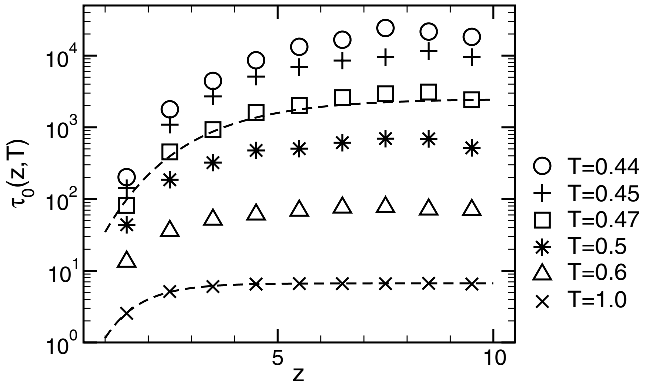

Figure 34. Layer-resolved relaxation time $\tau_0(z, T)$ versus distance z from the wall for a film of thickness $h = 20$. Here, z is defined as the distance of the centre of a layer from the (left) wall. The thickness of a layer is $\Delta z = 1$. $\tau_0(z, T)$ is computed from the local MSD $g_0(t, z)$ via equation (101). When calculating $g_0(t, z)$ only those monomers that remained in the layer at z for all times (equation (100)) were considered. The dashed lines for $T = 0.47$ and 1 indicate the results of a fit to equation (102). The fits depend on two parameters, $A(T)$ and $\xi_\tau(T)$. The prefactor τ_0 may be obtained independently from bulk simulations ($\tau_0(T = 1) = 6.67$, $\tau_0(T = 0.47) = 2500$). As no bulk data are available for $T < 0.46$, the analysis was restricted to $T \geqslant 0.46$. We find a weak temperature dependence for the prefactor ($A(T = 1) = 6.0$, $A(T = 0.47) = 7.5$). The dependence of ξ_τ on T is stronger: $\xi_\tau(T = 1) \simeq 0.81$, $\xi_\tau(T = 0.47) \simeq 1.78$ (cf figure 35). This figure is adapted from [70].

damped and bulk behaviour is recovered. This gradual damping could (or should) allow one to extract a length scale ξ characterizing the penetration of the wall effects into the inner part of the film.

One approach for determining ξ utilizes a local relaxation time as an intermediate step. Following equation (83) we may introduce such a relaxation time via

$$g_0(t = \tau_0(z, T), z) = 1. \tag{101}$$

Thus, $\tau_0(z, T)$ is the time it takes a monomer to move across its own size parallel to the wall in a layer at distance z from the wall.

Figure 34 depicts the results of this analysis for $h = 20$ and various temperatures. Not unexpectedly, we find that wall effects are small for high T. At $T = 1$, for example, $\tau_0(z)$ is independent of z in a large portion of the film. The corresponding constant value of $\tau_0(z)$ agrees with the relaxation time τ_0 obtained by applying equation (101) to the bulk data for $g_0(t)$. Upon cooling, however, wall effects become pronounced. They penetrate more and more into the film, the region of constant relaxation time shrinks and it should finally disappear when the perturbations emanating from the two walls overlap in the centre of the film. Such finite thickness effects seriously interfere with the desired determination of ξ. They should be avoided. For $h = 20$, the thickest film studied here, they become prominent if $T \lesssim 0.45$. We thus restricted the analysis to $T \geqslant 0.46$.

Quantifying the range of wall effects. In the following, we want to extract a length scale from the range over which a (static or dynamic) quantity deviates near the wall from bulk behaviour. When addressing this issue one is faced with the problem that there appears to be no theoretical concept to guide the analysis. One thus has to resort to an empirical parametrization of the data. Depending on the quantity under consideration different parametrization have been proposed (see e.g. [94, 267, 271, 272]).

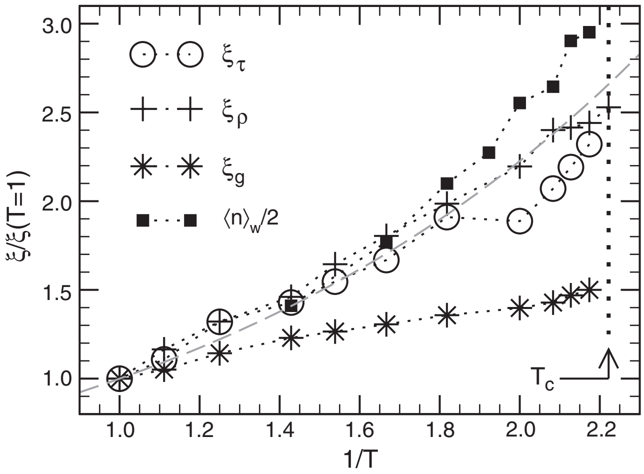

Figure 35. Various correlation lengths ξ versus $1/T$ for a film of thickness $h = 20$: ξ_τ = the decay length obtained from the local relaxation time $\tau_0(z, T)$ via equation (102), ξ_ρ = the decay length of the monomer density profile calculated from equation (105) and ξ_g = the decay length of the pair distribution function $g(r)$ determined via equation (103) ($g(r)$ is averaged over the film; r is the monomer distance measured parallel to the walls). All correlation lengths are divided by their value at $T = 1$ ($\xi_\tau = 0.814$, $\xi_\rho = 0.674$, $\xi_g = 0.980$). Furthermore, a bulk result is also shown: the weight-averaged cluster size $\langle n(t_{\text{clu}}^{\max})\rangle_{\text{w}}$ (divided by 2) at the time $t_{\text{clu}}^{\max}$ when the size of the clusters of mobile monomers peaks (cf figure 23(b)). The dotted vertical line indicates the MCT critical temperature in the bulk ($T_{\text{c}} = 0.45$); the grey dashed line represents an Arrhenius behaviour $\xi(T)/\xi(1) \propto \exp(0.8/T)$.

Simulations of a confined binary LJ liquid [94, 267] suggest the ansatz

$$\ln\left(\frac{\tau_0(z,T)}{\tau_0(T)}\right) = -A(T)\exp\left(-\frac{z}{\xi_\tau(T)}\right) \tag{102}$$

to model the z dependence of some local relaxation time, such as $\tau_0(z, T)$. Equation (102) introduces the length scale $\xi_\tau(T)$ to quantity the range of the deviations of $\tau_0(z, T)$ from the bulk value $\tau_0(T)$. In addition to $\xi_\tau(T)$, $A(T)$ is a further adjustable parameter which should, however, depend only weakly on temperature. The fact that this ansatz was found to provide an accurate description of various local relaxation times, not only for smooth walls, but also for rough amorphous walls [94, 267], prompted us to apply equation (102) to our simulation results for $\tau_0(z, T)$.

Representative examples of the analysis are included in figure 34. They illustrate that the data are compatible with equation (102), in accord with the results reported in [94, 267]. Also in agreement with [94, 267] we find that $\xi_\tau(T)$ increases only slightly—by a factor of ~2.5 (figure 35)—in the interval $0.47 \leqslant T \leqslant 1$ and, furthermore, that the numerical value of ξ_τ is small ($\xi_\tau \sim 1 \,\widehat{=}\,$ the monomer diameter).

A small length scale characterizing the range of the wall effects is not obtained only from $\tau_0(z, T)$; other quantities yield similar results. Figure 35 provides two examples, the length scales ξ_ρ and ξ_g. They are derived from static quantities, that is, from the monomer density profile (ξ_ρ) and from the film-averaged pair distribution function $g(r)$ (ξ_g). By analogy to the work of [267] we determined ξ_g by fitting the envelope of the pair distribution function via

$$g(r) - 1 \sim \exp\left(-\frac{r}{\xi_g}\right). \tag{103}$$

To extract a length scale from the density profile $\rho_\mathrm{m}(z)$, we followed a prescription proposed in [297]. We first subtracted from $\rho_\mathrm{m}(z)$ the bulk density ρ_m and then took the absolute value. This provides us with a quantity that decays from some value at the wall to 0 in the centre of the film. After normalization, this quantity may be interpreted as the probability density $p_\mathrm{m}(z)$ of finding a monomer at distance z,

$$p_\mathrm{m}(z) = \frac{|\rho_\mathrm{m}(z) - \rho_\mathrm{m}|}{\int_0^{h/2} \mathrm{d}z\, |\rho_\mathrm{m}(z) - \rho_\mathrm{m}|}. \tag{104}$$

The first moment of $p_\mathrm{m}(z)$ defines a decay length ξ_ρ for the density profile, i.e.,

$$\xi_\rho = \int_0^{h/2} \mathrm{d}z\, z p_\mathrm{m}(z). \tag{105}$$

Figure 35 shows that $\xi_g(T)$ increases only little on cooling (as it should for a glass-forming system), the increase being much weaker than that of $\xi_\tau(T)$. The situation is different for $\xi_\rho(T)$. One may recognize two features from figure 35.

First, ξ_τ is roughly proportional to ξ_ρ. The spatial inhomogeneities measured by $\rho_\mathrm{m}(z)$ apparently determine—for the present system—the range of the depression of $\tau_0(z, T)$ relative to the bulk relaxation time.

Second, the T dependence of ξ_τ and ξ_ρ is compatible with an Arrhenius law and close to that of a 'length scale' identified previously in the bulk, the weight-averaged cluster size $\langle n\rangle_\mathrm{w}$ of highly mobile monomers; cf section 3.4 (see [94, 267] for similar results for a confined binary LJ mixture). Whether the similarity of ξ_τ and $\langle n\rangle_\mathrm{w}$ is accidental or not is unclear at present; this certainly calls for further analysis. The weak Arrhenius-like dependence of the length scales on T is in stark contrast to the strong non-Arrhenius-like increase of structural relaxation times for the cold melt (figures 19 and 31). If there existed a correlation between the bulk relaxation time and these length scales, the previous argument suggests that it should be more complicated than a power law (i.e., $\tau \sim \xi^x$ with $x =$ constant; see e.g. [329] for such a 'more complicated' form suggested in simulations of a water model).

Layer-resolved dynamics: smooth walls versus crystalline and amorphous walls. A key point emerging from the discussion of the previous sections is that the smooth, structureless walls realized by equation (4) lead—for our model polymer films[33] —to a boundary condition which enhances monomer mobility and ultimately entails a depression of T_c (or of T_g).

It should be possible to reverse this trend by switching on sufficiently strong attractions between the monomers and the walls. This is evident e.g. from the work of references [259, 260, 263] (see also section 4.4).

Perhaps this effect of monomer–wall attractions is not too surprising. The situation becomes, however, more subtle if no or only weak preferential attractions are involved, but the wall exhibits some 'roughness' at the monomer level. This is suggested e.g. by the work of references [94, 263, 267, 330] (see also section 4.4).

---

[33] A caveat must be mentioned here. From the results presented one should not draw the general conclusion that smooth, structureless walls always lead to an acceleration of the dynamics in the supercooled state and, so, to a depression of T_g. Simulations of binary soft sphere mixtures confined between smooth walls provide counter-examples [270, 391]; they rather find the dynamics of the confined liquid to slow down relative to the bulk. A tentative explanation of this difference from our findings could be as follows. References [270, 391] also report that there are oscillations of the particle density close to the walls. The amplitude of these oscillations is, however, much more pronounced than in our case. This is a consequence of the model parameters employed in [270, 391]. For the mixtures there are densely filled layers of particles stacked on top of one another at low T—to some extent, similar (but stronger) to what we find for the crystalline walls (cf figure 36). Motion then has to occur in an environment of high density; it might therefore be slower than in the bulk.

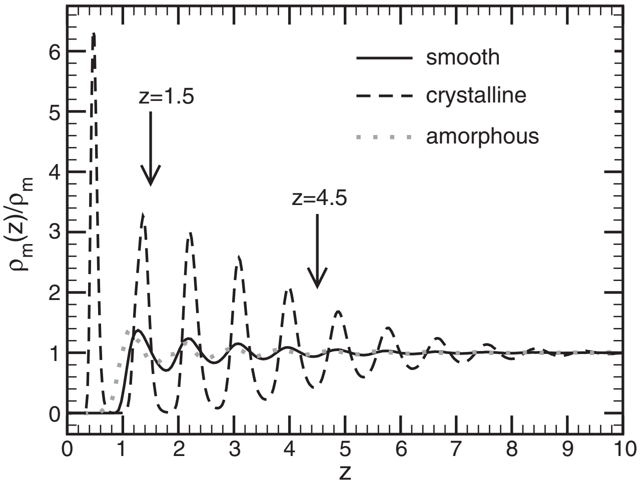

Figure 36. Monomer density profile $\rho_{\mathrm{m}}(z)$, normalized by the bulk density ρ_{m}, for different kinds of walls: smooth walls (equation (4); solid line), crystalline walls (equation (5); dashed line) and amorphous walls (see the end of section 2.3; dotted line). z denotes the distance from the (left) wall (cf the discussion of figure 25). The wall position, $z = 0$, in the case of crystalline walls is associated with the z coordinate of the crystalline layer of the wall atoms (arranged on the sites of a triangular lattice). For amorphous walls, it coincides by construction with the wall position which is realized in the case of smooth walls (cf section 2.3). The arrows at $z = 1.5$ and $z = 4.5$ indicate the centre of a layer (of width $\Delta z = 1$) for which the local dynamics is analysed in figure 37. All simulations were carried out with the Bennemann model for a glass-forming polymer melt (section 2.2) at temperature $T = 0.55$ and pressure $p = 1$. For these parameters the bulk density is $\rho_{\mathrm{m}} = 1.015$. In all cases the film thickness is $h = 20$.

We will focus on this latter situation here. We shall be concerned with the effect of crystalline and amorphous walls on the structure and dynamics of our model polymer films. The walls have an LJ interaction with the monomers, which is identical to that of the bulk (cf section 2.3); they thus merely represent a barrier with a roughness on the scale of the monomers.

The following discussion will be substantially briefer than it might be; we will concentrate on just two examples which illustrate the main qualitative changes with respect to smooth walls: the monomer density profile $\rho_{\mathrm{m}}(z)$ and the layer-resolved MSD $g_1(t, z)$ of the middle monomer of a chain (see equation (82) for the definition of this MSD in the bulk). The more restrictive prescription, equation (100), was employed to calculate $g_1(t, z)$.

Figure 36 depicts the density profile $\rho_{\mathrm{m}}(z)$ obtained from simulations at $T = 0.55$, $p = 1$ and $h = 20$ for smooth, crystalline and amorphous walls. The crystalline walls cause pronounced density oscillations in the polymer film. There are sharp maxima followed by deep minima, giving rise to an overall fairly long range decay of $\rho_{\mathrm{m}}(z)$ compared to those for the two other wall types—and this although the distance between atoms on the triangular lattice is incommensurable with the bond length of the chains. Apparently, monomers in contact with the wall (at $z \simeq 0.5$) still largely adapt their positions to the underlying crystalline structure.

We may expect this partial locking into registry of the monomers at $z \simeq 0.5$ to impose important constraints on the monomer mobility in subsequent layers. This expectation is indeed borne out, as revealed by figure 37. The figure shows that the MSD $g_1(t, z)$ for layers centred at $z = 1.5$ and 4.5 can be substantially less than in the bulk. At $z = 1.5$, for instance, we find an extended plateau symptomatic of the transient monomer localization (see section 3.3.2). The value of the plateau is smaller than the MSD corresponding to the Lindemann localization

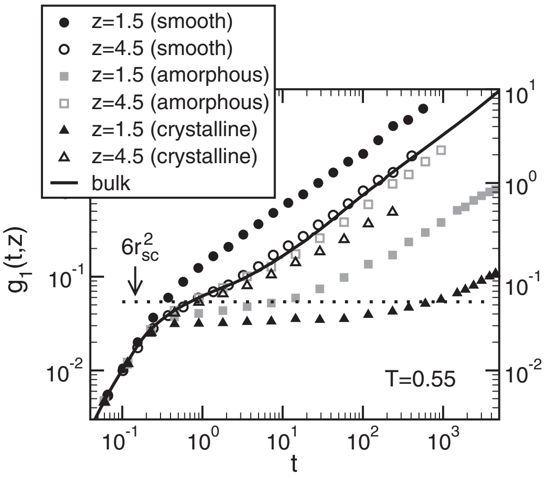

Figure 37. Layer-resolved mean square displacement (MSD) of the middle monomer of a chain, $g_1(t, z)$, versus time t for films of thickness $h = 20$ at $T = 0.55$ and different wall types as indicated. z denotes the distance from the (left) wall. The MSDs are calculated parallel to the wall and multiplied by 3/2 (to put them on the same scale as the bulk data (solid line) which are averaged over three spatial dimensions instead of over only two for the film). $g_1(t, z)$ is obtained as an average over all monomers which remain in their initial layer at z (cf equation (100); layer width $\Delta z = 1$). $g_1(t, z)$ is analysed for two layers, $z = 1.5$ and 4.5. The dotted horizontal line depicts $6r_{sc}^2$ ($\simeq$0.054; r_{sc} = the Lindemann localization length of the bulk).

length (for a definition see the discussion following equation (39)). If such a displacement was observed in the bulk, it would correspond to $T < T_c$.

The crystalline walls thus realize—without the need to exert specific attractions—a boundary condition that slows down, relative to the bulk, monomers in neighbouring layers. The same feature is also observed for the amorphous walls. They thus fall in the same category of boundary conditions as the crystalline walls, although the monomer density profile for the amorphous walls closely resembles the profile of the smooth walls (cf figure 36). The latter observation is important. It reveals that the density profile does not encapsulate all contributions necessary for understanding the dynamics and ultimately predicting the shift of T_g in confined liquids. This challenges the view described in the discussion of equation (91).

4.4. Brief survey of other simulation work

Over the past decade the glass transition of confined liquids has received considerable attention in simulation studies. Various systems—simple liquids [94, 266–268, 270, 272], hydrogen-bonded or molecular liquids [269, 271], silica [265], polymers [253–264] and confining geometries, pores [266, 269, 271], fillers in glass-forming matrices [254, 255, 268], thin films [94, 253, 256–265, 267, 270, 272]—have been considered.

Certainly, this list is not exhaustive; and certainly, all of the above-mentioned works would deserve a detailed presentation. Yet, our discussion will be substantially briefer than it might be. Instead of giving a comprehensive account we have chosen to describe a small number of results which we believe to be of particular interest.

Films—but also pores and filler particles in a glassy matrix. A thin film geometry is a popular choice for spatial confinement in many recent simulations. For glass-forming binary mixtures, freely standing films [272] and films between two smooth [94, 267, 270] or rough walls [94, 267] have been investigated. For polymer melts, simulations have explored properties of freely standing films (bead–spring and lattice models [256–260], lattice and continuum models of atactic polypropylene [253, 261]), supported films (bead–spring models [259, 260, 263, 264]) and films between flat or structured surfaces (bead–spring model [330], polystyrene between mica-type surfaces [262]).

The chain lengths employed in these simulations are in general smaller than or close to the entanglement length N_e ($15 \lesssim N \lesssim N_e \approx 32$ (see footnote 6) for bead–spring models). Since the typical range of film thicknesses is $10 \lesssim h \lesssim 25$ (although thinner [260, 262] and thicker films [259, 260] were also investigated), effects of confinement on polymer conformation should be small (because $h > R_g$ [295]). For simple liquids, a similar range of thicknesses ($10 \lesssim h \lesssim 20$) is commonly studied [94, 267, 270, 272].

These simulations provide numerous information on the equilibrium dynamics above T_g [94, 257, 267, 330], the freezing process during continuous cooling and the glass transition itself [253, 256, 260, 263, 264, 270], and mechanical or dynamical features in the glassy state [256, 261, 272]. Here we have chosen to mention the following results:

- For freely standing (polymer) films $T_g(h)$ generically decreases below the bulk value for small film thickness [253, 259, 260].
  If the glass former is in contact with a substrate (supported films, films between two walls), the shift of T_g depends on the 'particle–wall interaction'. Here, the term 'particle–wall interaction' has a twofold meaning: (i) Particle–wall attraction. Large enough attraction can lead to an increase of T_g [259, 260, 263]. (ii) Surface topography. Even without preferential attraction the dynamics may be strongly slowed down if particles become caged in cavities at the surface of the substrate (cf e.g. [94, 267, 330]; see also the discussion under the heading 'Layer-resolved dynamics: smooth walls versus crystalline and amorphous walls' in section 4.3.3). This steric effect may entail an increase of T_g.
- From the simulations [94, 256, 267, 330] it transpires that the density profile is not the sole factor determining the relaxation behaviour of confined glass formers and, so, their glass transition.
  The results of [267] provide a case in point. In this work, a model binary mixture is confined between two kinds of walls: rough walls and smooth walls. Rough walls are created in two steps: first, a bulk liquid is equilibrated at the desired temperature and then all particles in slices a distance h apart are frozen. As the structure of the walls is adapted to that of the liquid in between, the density profile is flat and has the bulk value. Confining the liquid by smooth walls, however, would produce density oscillations similar to those reported in section 4.2.1. To avoid these oscillations the authors of [267] added a term to the Hamiltonian which penalizes deviations from constant density. Thus, in this case too a flat profile having the bulk density is obtained.
  For both systems the layer-resolved incoherent intermediate scattering function $\phi_q^s(t, z)$—defined through the first prescription, equation (99)—was calculated and a relaxation time was determined via $\phi_q^s(\tau_q^s(z), z) = 1/e$. Figure 38 compares for both kinds of walls the z dependence of $\tau_q^s(z)$ obtained at the maximum of $S(q)$ of the A particles. Obviously, the α relaxation is slowed down on approaching the rough wall, but accelerated on approaching the smooth wall. So we find different dynamics, although the density profile is flat in both cases.
- The results of figure 38 suggest two further conclusions. (i) The film dynamics at low T is very heterogeneous; near the wall the relaxation times differ by orders of magnitude. (ii) The wall-induced fast or slow relaxation continuously turns into bulk-like relaxation

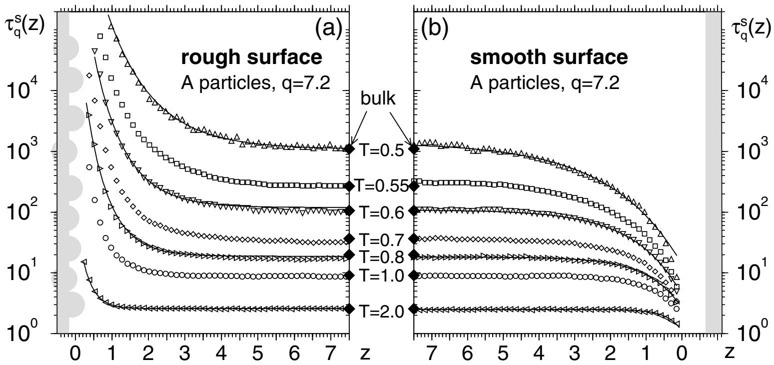

Figure 38. Structural relaxation time $\tau_q^{\mathrm{s}}(z)$ for the A particles of a binary LJ mixture at $q = 7.2$ (=the maximum of the A–A structure factor) as a function of particle distance z from a rough wall (a) and a smooth wall (b). The curves refer to different temperatures T (indicated in the middle of the figure). The MCT critical temperature of the bulk is $T_c \simeq 0.435$ [155, 168]. The filled diamonds indicate the bulk values of $\tau_q^{\mathrm{s}}(T)$. The solid lines represent fits to equation (102). (For rough walls, the rhs of equation (102) has to be adapted by making the change $A(T) \to -A(T)$.) The resulting dynamic length scales ξ_τ increase on cooling, roughly according to an Arrhenius law, but typically remain small ($\xi_\tau \lesssim 2$). This behaviour agrees with the results of figure 35 for our polymer model. The figure (adapted) is taken from [267] (reproduced with permission).

with increasing distance from the wall; this crossover remains continuous for all T; and its range grows on cooling[34].

The propagation of enhanced or reduced mobility from the boundary toward the interior of the film has also been observed in recent studies for freely standing [257] and supported polymer films [264]. These studies carried out a cluster analysis, of highly mobile monomers in the case of the freely standing film and of immobile monomers for the supported film. In both cases, it was found that clusters start at the interface and penetrate into the film.

- Figure 39(a) [94] shows the layer-resolved incoherent scattering function $\phi_q^{\mathrm{s}}(t, z)$ which corresponds to the relaxation time $\tau_q^{\mathrm{s}}(z)$ (figure 38(a)). The figure also depicts the scattering function of the bulk (circles) and the scattering function averaged over the film (crosses). Compared to the bulk correlator, that of the film has a peculiar shape. The α relaxation seems to occur in two steps. In fact, it is not possible to model the α relaxation by a single KWW function (equation (28)) [94]. Two KWW functions are required, one for the early α relaxation and another one to describe the slowly decaying tail for $t \gtrsim 5000$. The stretching exponent of this slow decay is very small, $\beta_{q=7.2}^{\mathrm{K}} \approx 0.3$. Thus, just on the basis of the data averaged over all layers of the film, one could suggest that there are two distinct processes, a fast one corresponding to a bulk-like phase in the film centre and a slow one associated with an interfacial phase. However, the layer-resolved analysis of figure 39(a) reveals that this interpretation may be misleading. The strongly stretched tail of the average correlator results from the smooth gradient in the relaxation of $\phi_q^{\mathrm{s}}(t, z)$ which slows down on approaching the wall (see [94] for a comprehensive discussion).

---

[34] The smoothness of this crossover seems hard to reconcile with a layer model, an often invoked interpretation for the relaxation of confined glass-forming liquids (see e.g. [392, 393]). This model assumes the coexistence of layers—typically one or two interfacial layers and an inner layer—with distinct mobilities (see e.g. [250] for a topical discussion of such models).

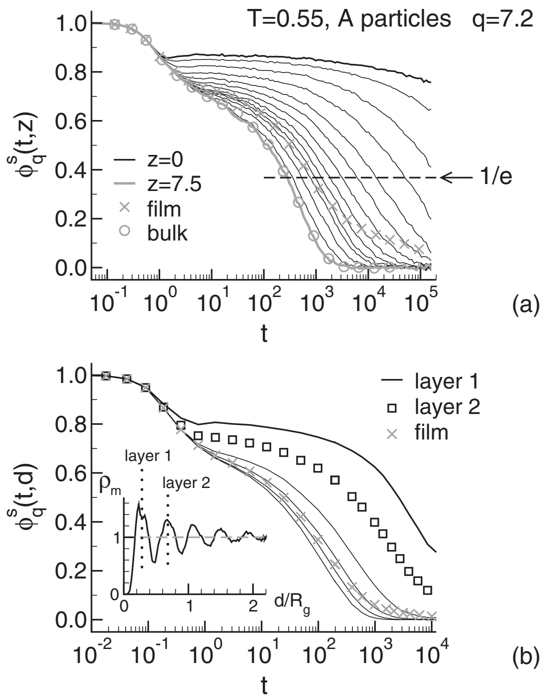

Figure 39. (a) Layer-resolved incoherent scattering function $\phi_q^{\mathrm{s}}(t,z)$ at $T = 0.55$ and $q = 7.2$ for the A particles of a binary LJ mixture (bulk $T_{\mathrm{c}} \simeq 0.435$; $q = 7.2 =$ the maximum of the A–A structure factor). The mixture is confined between two amorphous walls (film thickness $h = 15$). The solid lines depict $\phi_q^{\mathrm{s}}(t,z)$ for the following distances from the wall: $z = 0, 0.25, 0.5, \ldots, 2.5, 3, 4, 7.5$. The crosses indicate the average over all layers of the film, the circles the scattering function for the bulk. The dashed horizontal line indicates the criterion $1/e$ utilized to define the relaxation time $\tau_q^{\mathrm{s}}(z)$ shown in figure 38(a). The figure (adapted) is taken from [94] (reproduced with permission). (b) Layer-resolved incoherent scattering function $\phi_q^{\mathrm{s}}(t,d)$ at $T = 0.4$ and $q = 7.08$ (=the maximum of $S(q)$) for a polymer melt (Bennemann-like model) surrounding a filler particle. The chain length is $N = 20$, the melt density is $\rho_{\mathrm{m}} = 1$ (dashed horizontal line in the inset). The filler is of icosahedral shape and carries LJ sites at the surface. As the strength of the particle–monomer LJ potential is stronger than that between the monomers, monomers are attracted by the filler. The solid lines and the squares show $\phi_q^{\mathrm{s}}(t,d)$ for different distances d from the surface of the filler particle. The location of the first two layers is illustrated in the inset which depicts the monomer density profile $\rho_{\mathrm{m}}(d/R_{\mathrm{g}})$ ($R_{\mathrm{g}} \simeq 2.17$). The crosses indicate the average over all layers. The figure (adapted) is taken from [254] (reproduced with permission).

- The relaxation dynamics displayed in figure 39(a) is not limited to the system studied in [94]. Figure 39(b) provides a further example. It depicts the layer-resolved incoherent scattering function for a polymer melt (Bennemann-like model) surrounding a highly faceted, but nearly spherical filler particle [254, 255]. The filler has a structured surface and an attractive interaction with the monomers. Evidently, the data of figures 39(a) and (b) are qualitatively very similar, although the glass-forming liquids are different. Also for the polymer melt/filler particle system the late α process of the average dynamics exhibits a strongly stretched tail. The amplitude of this tail can be tuned by the monomer–filler interaction. Strong attraction leads to a more pronounced tail; vanishing attraction suppresses the tail [254, 255]. In the latter case, the scattering function resembles that of the bulk.

- One can gain additional insight into the slow relaxation of particles in contact with a structured wall by investigating the self-part of the van Hove correlation function—that is, the probability of finding a particle at time t at some distance from its initial position (cf equation (33)). For times in the α relaxation regime and temperatures well above T_c, the van Hove function displays features unfamiliar from the bulk. There is a clear two-peak structure. The first peak reflects particles that remain trapped in their cages, while the second peak, located on a length scale corresponding to the wall structure, reveals that particles have migrated to neighbouring wells. Evidence for this kind of 'hopping motion' is found e.g. for the binary LJ mixture discussed above [94], for a polymer melt adsorbed on a structured surface [330] and for model of liquid toluene confined in cylindrical mesopores [271]. This relaxation mechanism could be generic when a liquid may lock into registry with the surface topography.

In summary, we see that the features of dynamic correlation functions and related quantities can be fairly complex for confined glass-forming liquids. The simulations suggest that this complex behaviour has the following causes [94]: (i) the bulk-like slowing down of the dynamics on cooling; (ii) a smooth transition of enhanced or retarded relaxation relative to the bulk from the surface to the interior of the confined liquid; (iii) a growing range of this transition on cooling so that wall-induced perturbations of the dynamics may propagate across the entire liquid for sufficiently strong confinement and/or low T.

It seems that progress of our understanding hinges on whether it is possible to take into account the interplay of the three aforementioned points into a theoretical framework. We feel that such an approach will be promising if it treats the impact of boundary effects on the bulk dynamics at a microscopic level.

Comparison with experiments on supported PS films. Most experimental approaches to the glass transition in restricted geometry have been concerned with the average response of the confined liquid. A notable exception is the recent work of Ellison and Torkelson [250]. The authors employed a fluorescence/multilayer technique in which a thin fluorescent polystyrene (PS) layer is incorporated in an unlabelled PS film ($N \approx 4000$; $R_g \approx 17$ nm). This allowed them to measure the local T_g at different positions in the film.

Many interesting results are obtained from this approach. (i) The T_g of a fluorescent layer, placed on top of a bulk-like (∼270 nm thick) underlayer, decreases strongly with the thickness of the fluorescent layer. (ii) The T_g of a thin fluorescent layer (14 nm thick) at the surface of the film varies nonmonotonically with the overall film thickness. (iii) The T_g of a 14 nm thick fluorescent layer depends on its location in the film. When the layer is covered by an unlabelled PS layer whose thickness exceeds the range of 18–30 nm, it exhibits bulk T_g. For smaller thicknesses of the cover layer the T_g of the fluorescent layer is depressed relative to the bulk value; the depression increases with decreasing h of the cover layer.

From their analysis Ellison and Torkelson draw the following conclusions [250]: 'The results disallow the premises associated with simple two- and three-layer models that do not account for a smooth gradient in cooperative dynamics across the film thickness'. Furthermore, 'the most important length scale . . . is the distance over which a perturbation in cooperative dynamics at one location, for example, the free surface layer, affects the dynamics elsewhere in the film. Thus, if on average the cooperative dynamics in a layer are perturbed to be substantially enhanced relative to the bulk (as at a free surface), then, on average, adjoining layers must also have their dynamics perturbed, albeit to a lesser extent.'

These conclusions qualitatively agree with those drawn from the simulations.

Annex: a type of confinement special to computer simulations. Computer simulations are invariably conducted on systems whose size is small on the thermodynamic scale. Therefore, for a bulk system a special kind of confinement already exists due to the finite size of the system. The nature of possible finite size effects depends on the kinds of boundary conditions that are applied at the edges of the (cubic) simulation box. The prevailing choice in simulations is periodic boundary conditions. That is, if a particle leaves the box on one side, an identical image particle simultaneously enters the box on the opposite side. The simulation cell can thus be considered as a section of a macroscopic system. The fact that adjacent boxes are identical copies does not influence the features of the system provided that the box is large enough (and if there are no complications, like long range interactions, spontaneous ordering close to a critical point etc [105]). However, if the box size decreases, finite size effects may occur.

In recent years efforts have been made to explore finite size effects in the glassy state [331, 332], and as a liquid is cooled toward its glass transition [208, 333–336]. The systems studied comprise e.g. Lennard-Jones mixtures [208, 331–333], a soft sphere mixture [334], a hard sphere mixture [337] and a model for silica [335, 336]. The simulations above T_g demonstrate quite generally that the dynamics of a cold liquid slows down with decreasing system size. But the extent of these finite size effects appears to depend on the nature of the liquid. For instance, [208, 333] find that finite size effects on the structural relaxation—characterized by the incoherent scattering function at $q \approx q^*$ [333] or the diffusion coefficient [208]—become negligible for binary LJ mixtures if the system size exceeds 65 particles. On the other hand, finite size corrections on the relaxation of $\phi_q^\mathrm{s}(t)$ can still be detected for much larger systems—a few thousand particles—in the case of the soft sphere mixture [334] and silica [335, 336]. This difference is not fully understood (see e.g. [333] for a comparative discussion of the results from [333] and [334]; see [335] for a comparison of finite size effects in strong and fragile glass formers and [336] for an explanation of the finite size effects for $\phi_q^\mathrm{s}(t)$ in strong glass formers).

5. Summary and conclusions

In this review we were concerned with computer simulations of glass-forming polymer melts in the bulk and in a film geometry. This topic, albeit only one aspect of the research on glass-forming systems [18], has become so broad that it appears hard to write a comprehensive account of the many challenging questions and of the approaches applied to broach these issues computationally. Some selection is necessary.

We employed two criteria in this selection, one regarding the simulation model, the other regarding the temperature regime. We focused on what may arguably be considered as an archetypal model for polymer melts [29], a bead–spring model which takes into account only basic properties of (neutral homo)polymer chains, such as chain connectivity, excluded volume (cf section 2). For this model we explore structural, conformational and dynamic features in thermal equilibrium as the glass transition of the melt is approached on cooling. Simulations of chemically realistic polymer models [32], of driven (sheared) supercooled melts (see e.g. [72, 338, 339]) or phenomena pertaining to the glassy state, like physical ageing [18, 25, 340], mechanical properties of (polymeric) glasses (see e.g. [331, 332, 341]), the response of polymer glasses to strong deformations (see e.g. [26, 27]) etc are either touched upon only briefly (realistic models) or not discussed at all.

The requirement of thermal equilibrium limits the scope of our discussion—for both the bulk and the films—to temperatures larger than the critical glass temperature T_c of ideal mode-coupling theory (MCT). The application of MCT to the dynamics of the cold melt in the bulk represents a major part of this article. Here we attempted to be detailed and critical, assessing the strengths and weaknesses of the theory when compared to the simulation data (cf sections 3.3.2–3.3.4).

We feel that a particular strength of the theory is that it establishes a correlation between the structure and dynamics of a liquid. This correlation—more precisely, a distinctive dependence of the structural relaxation on the wavelength employed to probe the dynamics—is commonly observed in simulations of glass-forming systems, and also for our polymer model. MCT suggests a framework for interpreting these findings by providing detailed predictions for what to expect in the case of hard spheres. The comparison of the hard sphere results with those obtained for the simulated system helps to understand which aspects of the relaxation are 'simple liquid-like' and which are not. For our polymer model we identify—in agreement with the hard spheres case—local spatial correlations at the scale of the wavelength $1/q^*$ (the maximum of $S(q)$) as the origin for the slowing down of the dynamics as the melt is cooled toward T_c. On the other hand, density fluctuations on larger length scales ($q < q^*$) aggregate contributions from the chain relaxation; these cannot be understood within a theory for simple liquids. In this respect, a recent extension of MCT to nonentangled polymer melts [176] might prove to be helpful. Although the potential of this approach has not been fully explored here—section 3.3.5 only describes a first application—it might provide a clearer connection between the liquid dynamics and the relaxation of chain conformations. Such a connection is highly welcome. It offers the promise of obtaining a thorough understanding of the factors that control the range of validity of the Rouse model [2]—a classical model of polymer theory for chain transport and relaxation in nonentangled melts—and of corrections to it due to finite chain length, polymer structure etc.

The main weakness of the ideal MCT is known. The theory predicts vitrification at T_c while the expected divergence of the structural relaxation time is not observed in practice. Particles do eventually escape from their cages as T_c is approached from above. In simulations these deviations are often accompanied by a decoupling of the relaxation times on local ($q \approx q^*$) and large ($q \ll q^*$) length scales (cf section 3.3.6). This decoupling resembles the violation of the Stokes–Einstein relation found in experiments close to T_g. A popular explanation of this violation invokes the existence of spatially heterogeneous dynamics. This was one incentive to look for such dynamic heterogeneities in our polymer model, but here for $T > T_c$ (cf section 3.4). We tackle this problem by analysing spatio-temporal correlations of highly mobile monomers. We find that these monomers tend to cluster and to follow each other in (short) quasi-one-dimensional paths. These spatial correlations are temporary phenomena. They gradually develop throughout the β regime and are most prominent when the monomers begin to leave their cages in the late β/early α regime. These correlations are interesting on their own, putting our polymer model into perspective with simple liquids [192] or colloidal suspensions [200, 201] where similar results were obtained. Nonetheless the analysis still begs the question of whether these clustering phenomena hold the key to a better understanding of the relaxation channels missing in ideal MCT. There seems to be room for further progress here.

The second part of this review deals with the modelling of glass-forming polymer films. Those who read this part may share with the authors the impression expressed in [225]: boundary effects can have a crucial influence on the behaviour of the glass former. The simulations discussed in section 4 support this view. Confinement may alter structural features, and thereby the relaxation behaviour of the glass former—this was e.g. the case for our polymer model (sections 4.2 and 4.3)—or confinement may only affect the dynamics if special care is taken to avoid deviations from the bulk structure—as is the case e.g. in the work of [94] (cf section 4.4). These two examples reveal the important and complex impact that the boundary may exert on the properties of glass-forming liquids. We feel that theoretical approaches which are most likely to bring us forward should treat the interplay of boundary effects and glassy slowing down of the dynamics on the same (microscopic) footing. Folding in boundary effects is certainly a major challenge. We hope that simulations of ideal model systems—such as those reported here—will be helpful for developing such theories in the future.

Acknowledgments

This work was carried out in fruitful collaboration with M Aichele, C Bennemann, K Binder, J Buchholz, S-H Chong, C Donati, M Fuchs, Y Gebremichael, S C Glotzer, W Paul, M Mareschal and F W Starr. It is a great pleasure to thank all of them. At various passages in the text we presented results from the research of H Meyer, of W Paul, G D Smith and co-workers, of S C Glotzer, F W Starr and co-workers, of W L Mattice and co-workers, of S Herminghaus, K Jacobs and co-workers, of J A Forrest and co-workers, and of W Kob and co-workers. We are grateful that they quickly provided the figures requested. We are also indebted to M Fuchs for useful comments on the manuscript. Our simulations were made possible by generous grants of computer time at the computer centre of the Johannes Gutenberg-Universität Mainz and at the IDRIS in Orsay. Financial support by the Deutsche Forschungsgemeinschaft (VA 205/101), the ESF SUPERNET Programme, the DFG and MENRT (IGC 'Soft condensed matter'), and the IUF is gratefully acknowledged.

Appendix A. Fitting simulation data with the asymptotic MCT formulae: some suggestions

Tests of MCT utilizing the leading order predictions for the β relaxation (section 3.3.1) are hampered by a drawback. The range of validity of the asymptotic formulae—that is, the temperature and time intervals where they apply—is unknown. There is some freedom in the choice of these intervals, and this freedom will affect the numerical values of the fit parameters (see the discussion under the heading 'Critique of the quantitative analysis' in section 3.3.4). In doing the fit one must thus strike a suitable balance between the need to choose such intervals and the wish to obtain results free of internal inconsistencies.

Strategies for coping with this problem appear in the literature, but so scattered that it is difficult to quickly obtain the necessary overview to guide practical applications. The present appendix attempts to provide such guidance. It is mainly based on our own experience. We organize our discussion around the coherent scattering function $\phi_q(t)$. Of course, any other correlation function which couples to density fluctuations (e.g., the incoherent scattering function $\phi_q^{\mathrm{s}}(t)$) may be utilized.

To carry out the MCT analysis we suggest proceeding in the following way:

(i) We begin with the qualitative tests discussed in sections 3.3.2 and 3.3.3:

- Test of the factorization theorem via equation (32), i.e., via

$$R_q(t) = \frac{\phi_q(t) - \phi_q(t')}{\phi_q(t'') - \phi_q(t')} = \frac{G(t) - G(t')}{G(t'') - G(t')}. \tag{A.1}$$

  As this space–time factorization is a unique prediction of MCT, equation (A.1) will reveal whether the analysis of an observed two-step relaxation in terms of MCT is justified or not.

  Additionally, equation (A.1) is predicted to hold only close to T_{c}. This allows us to determine the T interval, $T_{\mathrm{c}} \lesssim T \leqslant T_{\max}$, where the asymptotic formulae should work in practice—some small print should appear here; we will come back to it after discussing the next test.

- Test of the TTSP via equation (26), i.e., via
$$\phi_q(t) = \tilde{\phi}_q(t/t'_\sigma) \qquad (t \geqslant t_\sigma). \tag{A.2}$$
Here, t_σ and t'_σ are the β and α relaxation times (cf equations (22,23)).
The key feature of equation (A.2) is that the scaling time t'_σ is independent of q. In practical applications we should thus employ a single relaxation time to attempt the construction of master curves for all q. The choice of this relaxation time depends on details of the available data, mainly on the length of the simulation runs, the accuracy of the time series at long times and the range of wavevectors studied. In our case [64], we used the α relaxation time τ_{q^*} determined at the maximum q^* of $S(q)$ via $\phi_{q^*}(\tau_{q^*}) = 0.1$. The threshold '0.1' is arbitrary, but convenient [64]: on the one hand, it is small enough that $\phi_q(t)$ is well in the α regime for $0 < q \lesssim 16$. On the other hand, it is sufficiently above the noise level that the statistical accuracy of the data remains satisfactory.
The superposition predicted by equation (A.2) will only work for T close to T_c. That is, in the T interval identified before by the test of the space–time factorization. There is however one reservation (the small print mentioned above). The TTSP breaks down in the immediate vicinity of T_c and for $T < T_c$, while equation (A.1) might still hold (cf figure 9, figure 11 and the discussion of section 3.3.3). So the TTSP allows us to determine the lowest temperature $T_{\min}$ for which the ideal MCT can be applied.
The TTSP provides further information: it suggests a lower bound for the nonergodicity parameter. According to equation (29), the α master curve has the following short time expansion:
$$\phi_q(t) = f_q^c - h_q B\left(t/t'_\sigma\right)^b \qquad (t_\sigma \leqslant t \ll t'_\sigma),$$
and so $\tilde{\phi}_q(t/t'_\sigma) \leqslant f_q^c$. ($B = B(\lambda)$ is a constant [145].) This implies that the fit result for f_q^c may not adopt values that cut the α master curve (see the discussion under the heading 'Critique of the quantitative analysis' in section 3.3.4). Thus, the master curve allows us to read off the lower bound $f_q^{c\,\min}$ for the fit parameter f_q^c in the β analysis.

(ii) The quantitative β analysis is based on equation (25) which we write as
$$\phi_q(t) = f_q^c + \frac{h_q^{\mathrm{fit}}}{t_\sigma^a}\, g(\hat{t}) + \frac{h_q^{\mathrm{fit}}}{t_\sigma^{2a}}\, B_q^{\mathrm{fit}}\, \hat{t}^{2b} + \underline{\frac{h_q^{\mathrm{fit}}}{t_\sigma^{2a}}\, A_q^{\mathrm{fit}}\, \hat{t}^{-2a}}, \tag{A.3}$$
where $h_q^{\mathrm{fit}} = h_q t_0^a$, $B_q^{\mathrm{fit}} = t_0^a B^2 B_q$, $A_q^{\mathrm{fit}} = t_0^a A_q$ and $\hat{t} = t/t_\sigma$ (see equations (22) and (25)). Equation (A.3) contains six fit parameters: f_q^c, h_q^{fit}, B_q^{fit}, A_q^{fit}, $t_\sigma(T)$ and λ. λ fixes the shape of $g(\hat{t})$ and determines the exponents a and b via equation (24). Of these parameters only t_σ depends on T.
When adjusting equation (A.3) to the simulation data we suggest proceeding in the following steps:
  (a) As a first step, we drop the underlined term in equation (A.3). It represents a correction to the short time behaviour of $g(\hat{t})$. Two justifications can be put forward. On the one hand, the precise determination of the short time behaviour of $g(\hat{t})$—and thus also of the correction to it—appears to be hard from simulations. References [106, 107] demonstrate this difficulty for simple glass-forming liquids. Structurally more complex glass formers, such as SiO_2 [174, 335], H_2O [172, 342] and *cis–trans* 1,4-polybutadiene [52], may exhibit a nonmonotonic t dependence at the beginning of

the plateau region. This still compounds the difficulty of a proper determination. On the other hand, the short time corrections are correlated with those at long times [142, 143]:

$$A_q^{\mathrm{fit}} = \frac{1}{B^2} B_q^{\mathrm{fit}} + \text{constant}. \tag{A.4}$$

As the dependence on q can thus be derived from the long time behaviour (for which the fit will be more precise), the short time corrections may be added later on (if necessary).

(b) The next step consists in utilizing equation (A.3) to determine λ. Following [178], information from the α process is crucial to this end. Two bits will be included. (i) We keep the term proportional to B_q^{fit}, i.e., the long time correction to the von Schweidler law (equation (29)). (ii) We require the fit result for f_q^{c} to obey $f_q^{\mathrm{c\,min}} \leqslant f_q^{\mathrm{c}} < 1$.
The actual (nonlinear) fit of the simulation data to equation (A.3) should be carried out at T_{min} and for, say, three wavevectors. We suggest working with q^*, a wavevector $q < q^*$ and q_{min}, the wavevector corresponding to the first minimum of $S(q)$. For q^* the von Schweidler process is pronounced; corrections to the factorization theorem should be small [143]. The final bit that is needed is the β scaling function $g(\hat{t})$. There are two ways to obtain it: either one calculates the full $g(\hat{t})$ numerically—the program may be requested from the authors of [141]—or one uses the asymptotic expressions published in [145]. (See e.g. [343] and [344] respectively for applications of the latter expressions to simulation and experimental data.)

(c) From this analysis we obtain estimates for λ and $t_\sigma(T_{\mathrm{min}})$. As a cross-check and/or to refine the fit parameters we propose repeating the last step for the incoherent scattering function $\phi_q^{\mathrm{s}}(t)$.

(d) The previous two steps yield f_q^{xc} (and thereby t_{co}), $h_q^{\mathrm{x\,fit}}$ and $B_q^{\mathrm{x\,fit}}$ at the selected q values. As a cross-check and to determine f_q^{xc} and $h_q^{\mathrm{x\,fit}}$ for other wavevectors we suggest using equation (47) and (48). That is,

$$\phi_q^{\mathrm{x}}(t_{\mathrm{co}}) = f_q^{\mathrm{xc}} \qquad \text{and} \qquad h_q^{\mathrm{x\,fit}} = \left.\frac{\partial_t \phi_q^{\mathrm{x}}(t)}{\partial_t[g(\hat{t})/t_\sigma^a]}\right|_{t=t_{\mathrm{co}}}. \tag{A.5}$$

Equation (A.5) is supposed to hold for all q and correlators ‘x’.
The remaining parameter $B_q^{\mathrm{x\,fit}}$ may then be fitted by equation (A.3).

(e) The previous steps provide λ, f_q^{xc}, $h_q^{\mathrm{x\,fit}}$, and $B_q^{\mathrm{x\,fit}}$. These parameters are supposed to be independent of T. Fixing them for $T_{\mathrm{min}} < T \leqslant T_{\mathrm{max}}$ we can apply equation (A.3) to the simulation data for $\phi_q(t)$ (and $\phi_q^{\mathrm{s}}(t)$) in the corresponding T interval to determine $t_\sigma(T)$. Equation (22) then gives the critical temperature,

$$t_\sigma^{-2a} \propto T - T_{\mathrm{c}} \qquad (T \geqslant T_{\mathrm{c}}).$$

(iii) *Variant of the analysis*. instead of fitting equation (A.3) one can also work with its long time behaviour only—that is, with the von Schweidler law (equation (29)) and the leading order correction to it,

$$\phi_q(t) = f_q^{\mathrm{c}} - \tilde{h}_q^{\mathrm{fit}} \left(t/t'_\sigma\right)^b + \tilde{h}_q^{\mathrm{fit}} \tilde{B}_q^{\mathrm{fit}} \left(t/t'_\sigma\right)^{2b} \qquad (t_\sigma \leqslant t); \tag{A.6}$$

$\tilde{h}_q^{\mathrm{fit}} = h_q B$, $\tilde{B}_q^{\mathrm{fit}} = B B_q$ and t'_σ is defined in equation (23). (The same constraints, $T_{\mathrm{min}} < T \leqslant T_{\mathrm{max}}$ and $f_q^{\mathrm{c\,min}} \leqslant f_q^{\mathrm{c}} < 1$, apply here too.) Equation (A.6) is easier to implement than equation (A.3)—we do not need the full $g(\hat{t})$—and might provide results of comparable quality, particularly for systems which exhibit a nonmonotonic t dependence at the beginning of the plateau (see the discussion above in item (a)).
While the knowledge of t_{co} can still be used via equation (A.5) to obtain f_q^{c} for other q values (and other correlators), $\tilde{h}_q^{\mathrm{fit}}$ has to be determined by the fit, in addition to $\tilde{B}_q^{\mathrm{fit}}$.

(iv) To broaden the comparison with MCT we may finally confront the results of the β analysis with those for the α process. The analysis of the α process involves two main steps. (i) KWW fits may be carried out for various q values to test the asymptotic predictions of equation (31). (ii) Again for various q values, the increase of the α relaxation time τ_q with decreasing T may be compared to equation (27):

$$\tau_q(T) = C_q t'_\sigma(T) \propto (T - T_\mathrm{c})^{-\gamma}, \tag{A.7}$$

which will be valid for $T > T_\mathrm{c}$ and for all q.

For the α analysis two caveats must be kept in mind. (i) The KWW fits depend sensitively on the fit interval; the stretching exponent β_q^{KWW} has large error bars (cf section 3.3.4 and e.g. [64] and references therein). (ii) To test equation (A.7) we can choose to fix γ from the β analysis, thus plotting $\tau_q{}^{-1/\gamma}$ versus T, or T_c from the β analysis, thus plotting $\log\tau_q$ versus $\log(T - T_\mathrm{c})$. In contrast to equation (A.7), the fits yield results for T_c or γ that depend on q (cf section 3.3.6, [60, 64] for our polymer model and [107, 162] for recent discussions in the context of simple liquids).

Appendix B. Supercooled liquids and potential energy landscape: some recent results

Consider a system of N structureless, classical particles interacting with each other. The interactions are governed by the potential energy U. U depends on the positions of the particles, $\{\boldsymbol{r}_i\}_{i=1,\ldots,N}$; it is a function of the coordinate $\boldsymbol{x} = (\boldsymbol{r}_1, \ldots, \boldsymbol{r}_N)$ locating the state of the system in configuration space. The function $U(\boldsymbol{x})$—the potential energy landscape (PEL)—is a complicated surface in a $(3N + 1)$-dimensional space. It determines the thermodynamic and dynamic properties of the system, as the system moves through configuration space along the trajectory $\boldsymbol{x}(t)$.

In the context of the supercooled liquids the challenge consists in understanding the correlation between topographic features of the PEL (minima, saddle points) and the way in which the trajectory $\boldsymbol{x}(t)$ samples the PEL at low T. This landscape-based approach to the glass transition was advocated more than 30 years ago by Goldstein [345], was turned into a practical simulation method by Stillinger and Weber [158, 346] and has recently found a lot of interest due to enhanced computational facilities and new theoretical developments originating from spin glass theory. In this appendix, we will not attempt to write a definitive account of these recent numerical and theoretical studies—they have been the subject of comprehensive reviews [20, 347, 348]. (For recent tests of the theoretical work see e.g. the review [34] (simulations) or [349] (experiment).) Here we provide rather a brief introduction to the field guided by some results that have emerged from recent simulations.

Thermodynamics and potential energy landscape. Important topographic features of the PEL are certainly the minimum positions. The configuration $\boldsymbol{x}_\mathrm{is}$ associated with a minimum is commonly referred to as 'inherent structure'; its energy $E_\mathrm{is} = U(\boldsymbol{x}_\mathrm{is})$ as 'inherent structure energy' [158]. Each inherent structure is surrounded by a 'basin of attraction', operationally defined by all configurations of the simulation trajectory, which can be mapped to the same $\boldsymbol{x}_\mathrm{is}$ via energy minimization—a bit more formally, $\{\boldsymbol{x}(t) | \min U(\boldsymbol{x}) = E_\mathrm{is}\}$ (see e.g. [333] for a pedagogical introduction). The assignment '$\boldsymbol{x} \to \boldsymbol{x}_\mathrm{is}$' naturally leads to a decomposition of configuration space into basins of inherent structures. This decomposition suggests approximating the free energy $F(T, V, N)$ of the supercooled liquid as a sum of a configurational and a vibrational part [20, 333, 350, 351]:

$$F(T, V, N) \approx \langle E_\mathrm{is}(T, V, N)\rangle - T S_\mathrm{conf}(\langle E_\mathrm{is}\rangle) + F_\mathrm{vib}(\langle E_\mathrm{is}\rangle; T, V, N). \tag{B.1}$$

The first two terms (the 'configurational part') characterize the system of inherent structures: $\langle E_{\mathrm{is}} \rangle$ is the average energy of the local minima sampled at temperature T and volume V. S_{conf} is called the 'configurational entropy'; it counts the number of minima with energy $\langle E_{\mathrm{is}} \rangle$. The third term, F_{vib}, represents the vibrational (harmonic and anharmonic) free energy of a basin of depth $\langle E_{\mathrm{is}} \rangle$; it depends on T explicitly and implicitly via $\langle E_{\mathrm{is}} \rangle$.

Simulation studies of simple [20, 333, 350] and molecular [351] glass formers indicate that this approach to the thermodynamics of supercooled liquids becomes viable below an 'onset temperature' $T_{\mathrm{o}} \approx 2T_{\mathrm{c}}$ [352, 353]. (T_{c} denotes again the critical temperature of MCT.) For $T_{\mathrm{c}} \lesssim T \lesssim 2T_{\mathrm{c}}$—the so-called 'landscape-influenced regime' [20]—$\langle E_{\mathrm{is}} \rangle$ and S_{conf} decrease strongly with T.[35] Parallel to that, the glass formers develop dynamic features predicted by MCT; the two-step relaxation of density and related correlation functions clearly emerges for $T_{\mathrm{c}} \lesssim T \lesssim 2T_{\mathrm{c}}$. This coincidence suggests searching for an interpretation of MCT from the viewpoint of the PEL.

Relaxation and potential energy landscape. The interpretation of the dynamics requires an analysis of the manner in which the system explores the PEL. Important topographic features in this context are the energy barriers that the system may encounter along its path. The task of characterizing the path and the barriers has been approached in different ways. Here we will briefly touch on two approaches.

One way of gathering information about the energy barriers, recently pursued by Sciortino and co-workers [354–356], is to analyse the minima of the 'pseudopotential' $W = |\nabla U(\boldsymbol{x})|^2$. Because configurations with $W = 0$ are saddle points, the minima $\boldsymbol{x}_{\mathrm{s}}$ of W are referred to as 'quasisaddles' [355]. The incentive for an analysis of W rests upon the fact that, at $\boldsymbol{x}_{\mathrm{s}}$, the force $\boldsymbol{F} = -\nabla U$ is small. So one can expect the dynamics to be slow. Whether it is slow should depend on the shape of the PEL near $\boldsymbol{x}_{\mathrm{s}}$. The shape can be characterized by the eigenvalues of the Hessian matrix at $\boldsymbol{x}_{\mathrm{s}}$, a negative eigenvalue corresponding to a downward curvature and, potentially, to a diffusive direction. An important feature of the quasisaddles is thus, besides their energy $E_{\mathrm{s}} = U(\boldsymbol{x}_{\mathrm{s}})$, their 'order' n_{s}, defined as the number of negative eigenvalues of the Hessian (divided by $3N$).

The analysis of W, performed on several glass-forming soft sphere and LJ systems, reveals two interesting results [355, 356]. (i) It is possible to construct master curves, e.g. for n_{s} versus T or $\langle E_{\mathrm{s}} \rangle - \langle E_{\mathrm{is}} \rangle$ versus n_{s}, when temperature or energy are scaled by T_{c}. (ii) n_{s} decreases with T and appears to vanish at T_{c}. Saddles of order zero ($n_{\mathrm{s}} = 0$) are inherent structures of the PEL. This latter finding was interpreted as evidence for the viewpoint of MCT that T_{c} marks the crossover temperature for a change in transport mechanism [23, 177]: below T_{c} the relaxation is governed by thermally activated hopping processes across saddle points of the PEL, whereas such hopping processes are subdominant for $T > T_{\mathrm{c}}$ and may be neglected for T not too close to T_{c} (see the discussion at the end of section 3.3.1).

The significance of the quasisaddles and, along with that, the interpretation of the results have been challenged by Doliwa and Heuer, on the basis of a detailed investigation of the PEL for a binary LJ mixture [357–359]. Doliwa and Heuer propose an original method for locating the transition states on the borders of the energy basins and argue that the quasisaddles systematically overestimate the true energy barriers determining the diffusion of a particle [358]. Their method offers the possibility of following closely the escape of the system

---

[35] The analysis of [350] suggests that the configurational entropy extrapolates to 0 at a finite temperature T_{K}. T_{K} may thus be identified with the 'Kauzmann temperature' (see e.g. [394] for a recent discussion), provided that the extrapolation is reliable—as carefully stated in [350]. The reliability of the extrapolation has recently been challenged by the results of new simulations, apparently achieving thermal equilibrium well below T_{c} via modern Monte Carlo methods [115]. See also [111] for a critical re-evaluation of recent numerical work on the 'entropy crisis' in model glass formers.

from an inherent structure. It reveals a funnel-like superstructure of the PEL. The PEL appears to be organized in 'metabasins' [158], defined as groups of adjacent minima which are repeatedly visited before the system finally succeeds in escaping from this region of the PEL. At temperature T, the metabasins of energy E_{mb} are populated with probability $p(E_{\mathrm{mb}}, T)$ and the temporary trapping of the system—the repeated visits of the same inherent structures—in the metabasin determines the average waiting time $\tau(E_{\mathrm{mb}}, T)$ before the system escapes from the basin. The analysis of [358, 359] reveals two interesting results in the 'landscape-influenced' regime ($T_{\mathrm{c}} \lesssim T \lesssim 2T_{\mathrm{c}}$). (i) The waiting time closely follows an Arrhenius law, $\tau(E_{\mathrm{mb}}, T) \propto \exp[E(E_{\mathrm{mb}})/k_{\mathrm{B}}T]$. (ii) The diffusion coefficient of a particle is well approximated by

$$D(T) \propto \int \mathrm{d}E_{\mathrm{mb}}\, p(E_{\mathrm{mb}}, T) \exp\left[-E(E_{\mathrm{mb}})/k_{\mathrm{B}}T\right], \tag{B.2}$$

suggesting that activated barrier crossings determine the diffusion dynamics up to $T \approx T_{\mathrm{o}} = 2T_{\mathrm{c}}$.

Equation (B.2) is not the only relation that has been proposed as a possible link between the topographic features of the PEL and the dynamics of supercooled liquids. Simulation studies on a binary LJ mixture [360] and models for water [329, 361] and *ortho*-terphenyl [362] suggest that the Adam–Gibbs formula (see e.g. [18, 20]),

$$\ln D(T) \propto \frac{1}{T S_{\mathrm{conf}}(T)}, \tag{B.3}$$

provides a viable description in the supercooled state (apparently, for both $T \geqslant T_{\mathrm{c}}$ and $T < T_{\mathrm{c}}$ [362]). A firm confirmation of equation (B.3) would imply that there is a relationship between the depth distribution of inherent structures and the barrier heights between them. Such a connection between thermodynamic (S_{conf}) and dynamic features (barrier heights) is not a necessity. For instance, the two contributions are well separated in equation (B.2), and this might appear more natural (see e.g. the discussion in [363]).

A final remark. While there appears to be some consensus as regards which features of the PEL determine the thermodynamics of (model) glass formers in the supercooled state, the preceding discussion demonstrates that the interpretation of the dynamics is still a matter of controversy. We feel that there are two challenges, one conceptual, the other technical.

Conceptually, the challenge consists in finding those landscape characteristics that are responsible for the slow relaxation of collective variables, such as longitudinal and traverse currents or density fluctuations on different length scales. Attempts to relate features of the PEL to the real space dynamics represent promising first steps [209, 213, 329].

Technically, the simulation studies of the PEL presented are at the limit of what is currently feasible. Nevertheless, they often only involve about 100 particles. For a particle density $\rho = 1$, this implies a linear extent of the simulation box of about 5—the pair distribution function is truncated between the second-and third-nearest neighbour shells. While arguments have been presented that this system size suffices to approximate the macroscopic limit, at least in the case of LJ systems for $T_{\mathrm{c}} \lesssim T \lesssim 2T_{\mathrm{c}}$ [208, 333], finite size effects may be a particular hazard at lower T or for other systems. Improved computational facilities should alleviate this problem in the future.

References

[1] Lodge T P and Muthukumar M 1996 *J. Phys. Chem.* **100** 13275
[2] Doi M and Edwards S F 1986 *The Theory of Polymer Dynamics* (Oxford: Oxford University Press)
[3] Rubinstein M and Colby R H 2003 *Polymer Physics* (Oxford: Oxford University Press)

[4] de Gennes P-G 1996 *Scaling Concepts in Polymer Physics* (Ithaca, NY: Cornell University Press)
[5] Witten T A 1998 *Rev. Mod. Phys.* **70** 1531
[6] Edwards S F 1975 *J. Phys. A: Math. Gen.* **8** 1670
[7] Muthukumar M and Edwards S F 1982 *J. Chem. Phys.* **76** 2720
[8] Wittmer J P *et al* 2004 *Phys. Rev. Lett.* **93** 147801
[9] McLeish T C B 2002 *Adv. Phys.* **51** 1379
[10] Meyer H and Müller-Plathe F 2001 *J. Chem. Phys.* **115** 7807
[11] Meyer H and Müller-Plathe F 2002 *Macromolecules* **35** 1241
[12] Strobl G 1997 *The Physics of Polymers: Concepts for Understanding their Structures and Behavior* (Berlin: Springer)
[13] Armitstead K and Goldbeck-Wood G 1992 *Adv. Polym. Sci.* **100** 219
[14] Muthukumar M 2004 *Adv. Chem. Phys.* **128** 1
[15] Strobl G 2000 *Eur. Phys. J.* E **3** 165
[16] Lotz B 2000 *Eur. Phys. J.* E **3** 185
[17] McKenna G B 1986 *Comprehensive Polymer Science* vol 2, ed C Booth and C Price (New York: Pergamon) pp 311–62
[18] Angell C A *et al* 2000 *J. Appl. Phys.* **88** 3113
[19] Donth E 2001 *The Glass Transition* (Berlin: Springer)
[20] Debenedetti P G and Stillinger F H 2001 *Nature* **410** 259
[21] Götze W 1999 *J. Phys.: Condens. Matter* **11** A1
[22] Götze W and Sjögren L 1992 *Rep. Prog. Phys.* **55** 241
[23] Götze W 1998 *Condens. Matter. Phys.* **1** 873
[24] Götze W 1991 *Proc. Les Houches Summer School of Theoretical Physics (Les Houches 1989, Session LI)* ed J P Hansen, D Levesque and J Zinn-Justin (Amsterdam: North-Holland) pp 287–503
[25] Crisanti A and Ritort F 2003 *J. Phys.: Condens. Matter* **36** R181
[26] Baljon A R C and Robbins M O 2001 *Macromolecules* **34** 4200
[27] Rottler J and Robbins M O 2003 *Phys. Rev.* E **68** 011801
[28] Baschnagel J, Wittmer J P and Meyer H 2004 *Computational Soft Matter: From Synthetic Polymers to Proteins* (*NIC Series* vol 23) ed N Attig, K Binder, H Grubmüller and K Kremer (Jülich: NIC) pp 83–40 (available from http://www.fz-juelich.de/nic-series)
[29] Kröger M 2004 *Phys. Rep.* **390** 453
[30] Kremer K 2004 *Computational Soft Matter: From Synthetic Polymers to Proteins* (*NIC Series* vol 23) ed N Attig, K Binder, H Grubmüller and K Kremer (Jülich: NIC) pp 141–68 (available from http://www.fz-juelich.de/nic-series)
[31] Clarke J H R 1995 *Monte Carlo and Molecular Dynamics Simulations in Polymer Science* ed K Binder (New York: Oxford University Press) pp 272–306
[32] Paul W and Smith G D 2004 *Rep. Prog. Phys.* **67** 1117
[33] Binder K, Baschnagel J and Paul W 2003 *Prog. Polym. Sci.* **28** 115
[34] Binder K 2004 *Proc. Int. School of Physics 'Enrico Fermi'* ed F Mallamace and H E Stanley (Amsterdam: IOS Press) pp 17–82
[35] Müller-Plathe F 2002 *Chem. Phys. Chem.* **3** 754
[36] Müller-Plathe F 2003 *Soft Mater.* **1** 1
[37] Glotzer S C and Paul W 2002 *Annu. Rev. Mater. Res.* **32** 401
[38] Binder K 1995 *Monte Carlo and Molecular Dynamics Simulations in Polymer Science* ed K Binder (New York: Oxford University Press) pp 3–46
[39] Kob W 1995 *Annual Reviews of Computational Physics* vol 3, ed D Stauffer (Singapore: World Scientific) p 1
[40] Kob W 1999 *J. Phys.: Condens. Matter* **11** R85
[41] Baschnagel J *et al* 2000 *Adv. Polym. Sci.* **152** 41
[42] Marx D and Hutter J 2000 *Modern Methods and Algorithms of Quantum Chemistry* (*NIC Series* vol 3) ed J Grotendorst, D Marx and A Muramatsu (Jülich: NIC) pp 329–477 (available from http://www.fz-juelich.de/nic-series)
[43] Allen M P 2004 *Computational Soft Matter: From Synthetic Polymers to Proteins* (*NIC Series* vol 23) ed N Attig, K Binder, H Grubmüller and K Kremer (Jülich: NIC) pp 1–28 (available from http://www.fz-juelich.de/nic-series)
[44] Binder K *et al* 2004 *J. Phys.: Condens. Matter* **16** S429
[45] Kremer K 2003 *Macromol. Chem. Phys.* **204** 257
[46] Clarke J H R 1998 *Curr. Opin. Solid State Mater.* **3** 596

[47] Colmenero J, Alvarez F and Arbe A 2002 *Phys. Rev.* E **65** 041804

[48] Colmenero J *et al* 2003 *J. Phys.: Condens. Matter* **15** S1127

[49] Lyulin A V and Michels M A J 2002 *Macromolecules* **35** 1463

[50] Lyulin A V and Michels M A J 2002 *Macromolecules* **35** 9595

[51] Lyulin A V, Balabaev N K and Michels M A J 2003 *Macromolecules* **36** 8574

[52] Smith G D, Bedrov D and Paul W 2004 *J. Chem. Phys.* **121** 4961

[53] Krushev S and Paul W 2003 *Phys. Rev.* E **67** 021806

[54] Krushev S, Paul W and Smith G D 2002 *Macromolecules* **35** 4198

[55] Smith G D, Borodin O and Paul W 2002 *J. Chem. Phys.* **117** 10350

[56] Smith G D, Paul W, Monkenbusch M and Richter D 2000 *Chem. Phys.* **261** 61

[57] Kremer K and Binder K 1988 *Comput. Phys. Rep.* **7** 259

[58] Bennemann C, Paul W, Binder K and Dünweg B 1998 *Phys. Rev.* E **57** 843

[59] Bennemann C, Baschnagel J and Paul W 1999 *Eur. Phys. J.* B **10** 323

[60] Bennemann C, Paul W, Baschnagel J and Binder K 1999 *J. Phys.: Condens. Matter* **11** 2179

[61] Bennemann C, Baschnagel J, Paul W and Binder K 1999 *Comput. Theor. Polym. Sci.* **9** 217

[62] Bennemann C, Donati C, Baschnagel J and Glotzer S C 1999 *Nature* **399** 246

[63] Aichele M and Baschnagel J 2001 *Eur. Phys. J.* E **5** 229

[64] Aichele M and Baschnagel J 2001 *Eur. Phys. J.* E **5** 245

[65] Buchholz J, Paul W, Varnik F and Binder K 2002 *J. Chem. Phys.* **117** 7364

[66] Aichele M *et al* 2003 *J. Chem. Phys.* **119** 5290
Aichele M *et al* 2003 *J. Chem. Phys.* **120** 6798 (publisher's note)

[67] Aichele M, Chong S-H, Baschnagel J and Fuchs M 2004 *Phys. Rev.* E **69** 061801

[68] Varnik F, Baschnagel J and Binder K 2000 *J. Chem. Phys.* **113** 4444

[69] Varnik F 2002 *Comput. Phys. Commun.* **149** 61

[70] Varnik F, Baschnagel J and Binder K 2002 *Phys. Rev.* E **65** 021507

[71] Varnik F, Baschnagel J and Binder K 2002 *Eur. Phys. J.* E **8** 175

[72] Varnik F and Binder K 2002 *J. Chem. Phys.* **117** 6336

[73] Varnik F, Baschnagel J, Binder K and Mareschal M 2003 *Eur. Phys. J.* E **12** 167

[74] Kremer K and Grest G S 1990 *J. Chem. Phys.* **92** 5057

[75] Dünweg B, Stevens M and Kremer K 1995 *Monte Carlo and Molecular Dynamics Simulations in Polymer Science* ed K Binder (New York: Oxford University Press) pp 125–93

[76] Kremer K and Grest G S 1995 *Monte Carlo and Molecular Dynamics Simulations in Polymer Science* ed K Binder (New York: Oxford University Press) pp 194–271

[77] Pütz M, Kremer K and Grest G S 2000 *Europhys. Lett.* **49** 735
see also Pütz M, Kremer K and Grest G S 2000 *Europhys. Lett.* **52** 719 (Comment)
Pütz M, Kremer K and Grest G S 2000 *Europhys. Lett.* **52** 721 (Reply)

[78] Grest G S and Murat M 1995 *Monte Carlo and Molecular Dynamics Simulations in Polymer Science* ed K Binder (New York: Oxford University Press) pp 476–578

[79] Grest G S 1999 *Adv. Polym. Sci* **138** 149

[80] Müller M and Gonzalez MacDowell L 2000 *Macromolecules* **33** 3902

[81] Virnau P, Müller M, Gonzalez MacDowell L and Binder K 2004 *New J. Phys.* **6** 7

[82] Heine D R, Grest G S and Webb E B III 2003 *Phys. Rev.* E **68** 061603

[83] Tsige M and Grest G S 2004 *Macromolecules* **37** 4333

[84] Allen M P and Tildesley D J 1994 *Computer Simulation of Liquids* (Oxford: Clarendon)

[85] Frenkel D and Smit B 2002 *Understanding Molecular Simulation* 2nd edn (London: Academic)

[86] Virnau P, Müller M, Gonzalez MacDowell L and Binder K 2004 *J. Chem. Phys.* **121** 2169

[87] Patrykiejew A, Sokolowski S and Binder K 2000 *Surf. Sci. Rep.* **37** 207

[88] Steele W A 1973 *Surf. Sci.* **36** 317

[89] Metzger S, Müller M, Binder K and Baschnagel J 2002 *Macromol. Theory Simul.* **11** 985

[90] Metzger S, Müller M, Binder K and Baschnagel J 2003 *J. Chem. Phys.* **118** 8489

[91] Müller M, Binder K and Albano E V 2001 *Int. J. Mod. Phys.* B **15** 1867

[92] Robbins M O and Müser M H 2001 *Modern Tribology Handbook* ed B Bhushan (New York: CRC Press) pp 717–65

[93] Varnik F 2000 *Dissertation* Johannes Gutenberg-Universität Mainz (available from http://archimed.uni-mainz.de/pub/2001/0007)

[94] Scheidler P, Kob W and Binder K 2004 *J. Phys. Chem.* B **108** 6673

[95] Hoover W G 1985 *Phys. Rev.* A **31** 1695

[96] Hoover W G 1986 *Phys. Rev.* A **34** 2499

[97] Melchionna S, Ciccotti G and Holian B 1993 *Mol. Phys.* **78** 533

[98] Soddemann T, Dünweg B and Kremer K 2003 *Phys. Rev.* E **68** 046702

[99] Barbieri A, Campani E, Capaccioli S and Leporini D 2004 *J. Chem. Phys.* **120** 437

[100] Rowlinson J S and Widom B 1982 *Molecular Theory of Capillarity* (Oxford: Clarendon)

[101] Davis H T 1995 *Statistical Mechanics of Phases, Interfaces and Thin Films* (New York: Wiley–VCH)

[102] Lovett R and Baus M 1997 *Adv. Chem. Phys.* **102** 1

[103] Jones R A L 1999 *Curr. Opin. Colloid Interface Sci.* **4** 153

[104] Forrest J A and Dalnoki-Veress K 2001 *Adv. Colloid Interface Sci.* **94** 167

[105] Landau D P and Binder K 2000 *A Guide to Monte Carlo Simulations in Statistical Physics* (Cambridge: Cambridge University Press)

[106] Gleim T, Kob W and Binder K 1998 *Phys. Rev. Lett.* **81** 4404

[107] Voigtmann T, Puertas A M and Fuchs M 2004 *Phys. Rev.* E **70** 061506

[108] Karayiannis N C, Giannousaki A E, Mavrantzas V G and Theodorou D N 2002 *J. Chem. Phys.* **117** 5465

[109] Banaszak B J and de Pablo J J 2003 *J. Chem. Phys.* **119** 2456

[110] Auhl R *et al* 2003 *J. Chem. Phys.* **119** 12718

[111] Brumer Y and Reichman D R 2004 *J. Phys. Chem.* B **108** 6832

[112] Bunker A and Dünweg B 2000 *Phys. Rev.* E **63** 016701

[113] Yamamoto R and Kob W 2000 *Phys. Rev.* E **61** 5473

[114] De Michele C and Sciortiono F 2002 *Phys. Rev.* E **65** 051202

[115] Yan Q, Jain T S and de Pablo J J 2004 *Phys. Rev. Lett.* **92** 235701

[116] Meyer H 2003 *Polymer Crystallization: Observations, Concepts and Interpretations* (*Springer Lecture Notes in Physics* vol 606) ed J-U Sommer and G Reiter (Berlin: Springer) pp 177–95

[117] Meyer H 2004 private communication

[118] Horbach J and Kob W 1999 *Phys. Rev.* B **60** 3169

[119] Hansen J P and McDonald I R 1986 *Theory of Simple Liquids* (London: Academic)

[120] Fuchs M and Schweizer K S 2002 *J. Phys.: Condens. Matter* **14** R329

[121] Barbieri A, Prevosto D, Lucchesi M and Leporini D 2004 *J. Phys.: Condens. Matter* **16** 6609

[122] Frick B, Farago B and Richter D 1990 *Phys. Rev. Lett.* **64** 2921

[123] Zorn R, Richter D, Frick B and Farago B 1993 *Physica* A **201** 52

[124] Schweizer K S and Curro J G 1994 *Adv. Polym. Sci.* **116** 319

[125] Morineau D and Alba-Simionesco C 1998 *J. Chem. Phys.* **109** 8494

[126] Morineau D and Alba-Simionesco C 2003 *J. Chem. Phys.* **118** 9389

[127] Hansen J-P and Verlet L 1969 *Phys. Rev.* **184** 151

[128] van Megen W 1995 *Transp. Theory Stat. Phys.* **24** 1017

[129] van Megen W, Mortensen T C, Müller J and Williams S R 1998 *Phys. Rev.* E **58** 6073

[130] Bartsch E 1998 *Curr. Opin. Colloid Interface Sci.* **3** 577

[131] Götze W and Sjögren L 1991 *Phys. Rev.* A **43** 5442

[132] Schweizer K S and Curro J G 1997 *Adv. Chem. Phys.* **98** 1

[133] Chandler D and Andersen H C 1972 *J. Chem. Phys.* **57** 1930

[134] Pütz M, Curro J G and Grest G S 2001 *J. Chem. Phys.* **114** 2847

[135] Sides S W *et al* 2002 *Macromolecules* **35** 6455

[136] Curro J G, Schweizer K S, Grest G S and Kremer K 1989 *J. Chem. Phys.* **91** 1357

[137] Schweizer K S, Honnell K G and Curro J G 1992 *J. Chem. Phys.* **96** 3211

[138] Curro J G *et al* 1999 *J. Chem. Phys.* **111** 9073

[139] Götze W and Sjögren L 1995 *Transp. Theory Stat. Phys.* **24** 801

[140] Götze W and Sjögren L 1987 *Z. Phys.* B **65** 415

[141] Fuchs M, Götze W, Hildebrand S and Latz A 1992 *J. Phys.: Condens. Matter* **4** 7709

[142] Franosch T *et al* 1997 *Phys. Rev.* E **55** 7153

[143] Fuchs M, Götze W and Mayr M R 1998 *Phys. Rev.* E **58** 3384

[144] Palmer R G 1982 *Adv. Phys.* **6** 669

[145] Götze W 1990 *J. Phys.: Condens. Matter* **2** 8485

[146] Fuchs M, Hofacker I and Latz A 1992 *Phys. Rev.* A **45** 898

[147] Fuchs M 1994 *J. Non-Cryst. Solids* **172–174** 241

[148] Franosch T, Götze W, Mayr M R and Singh A P 1998 *J. Non-Cryst. Solids* **235–237** 71

[149] Kob W, Nauroth M and Sciortino F 2002 *J. Non-Cryst. Solids* **307–310** 181

[150] Rössler E and Sillescu H 1991 *Material Science and Technology* vol IX, ed J Zarzycki (Weinheim: VCH) pp 573–618

[151] Götze W and Voigtmann T 2000 *Phys. Rev.* E **61** 4133

[152] Liu C Z-W and Oppenheim I 1997 *Physica* A **235** 369
[153] Gleim T and Kob W 2000 *Eur. Phys. J.* B **13** 83
[154] Signorini G F, Barrat J-L and Klein M L 1990 *J. Chem. Phys.* **92** 1294
[155] Kob W and Andersen H C 1995 *Phys. Rev.* E **51** 4626
[156] Kob W, Horbach J and Binder K 1999 *Slow Dynamics in Complex Systems* vol 469 (Woodbury, NY: AIP) pp 441–51
[157] Doliwa B and Heuer A 1998 *Phys. Rev. Lett.* **80** 4915
[158] Stillinger F H 1995 *Science* **267** 1935
[159] Zhou Y, Karplus M, Ball K D and Berry R S 2002 *J. Chem. Phys.* **116** 2323
[160] Chong S-H and Sciortino F 2004 *Phys. Rev.* E **69** 051202
[161] Rinaldi A, Sciortino F and Tartaglia P 2001 *Phys. Rev.* E **63** 061210
[162] Foffi G *et al* 2004 *Phys. Rev.* E **69** 011505
[163] Balucani U and Zoppi M 2003 *Dynamics of the Liquid State* (Oxford: Oxford University Press)
[164] Sköld K 1967 *Phys. Rev. Lett.* **19** 1023
[165] Bagchi B and Bhattacharyya S 2001 *Adv. Chem. Phys.* **116** 68
[166] Paul W *et al* 1998 *Phys. Rev. Lett.* **80** 2346
[167] Smith G D, Paul W, Monkenbusch M and Richter D 2001 *J. Chem. Phys.* **114** 4285
[168] Kob W and Andersen H C 1995 *Phys. Rev.* E **52** 4134
[169] Nauroth M and Kob W 1997 *Phys. Rev.* E **55** 657
[170] Kämmerer S, Kob W and Schilling R 1998 *Phys. Rev.* E **58** 2131
[171] Winkler A, Latz A, Schilling R and Theis C 2000 *Phys. Rev.* E **62** 8004
[172] Sciortino F, Fabbian L, Chen S-H and Tartaglia P 1997 *Phys. Rev.* A **56** 5397
[173] Mossa S, Di Leonardo R, Ruocco G and Sampoli M 2000 *Phys. Rev.* E **62** 612
[174] Horbach J, Kob W and Binder K 1998 *Phil. Mag.* B **77** 297
[175] Starr F W, Sciortino F and Stanley H E 1999 *Phys. Rev.* E **60** 6757
[176] Chong S-H and Fuchs M 2002 *Phys. Rev. Lett.* **88** 185702
[177] Franosch T and Götze W 1999 *J. Phys. Chem.* B **103** 4011
[178] Sciortino F and Tartaglia P 1999 *J. Phys.: Condens. Matter* **11** A261
[179] Zeng X C, Kivelson D and Tarjus G 1994 *Phys. Rev.* E **50** 1711
[180] Cummins H Z and Li G 1994 *Phys. Rev.* E **50** 1720
[181] Sciortino F and Kob W 2001 *Phys. Rev. Lett.* **86** 648
[182] Chong S-H and Götze W 2002 *Phys. Rev.* E **65** 041503
[183] Chong S-H and Sciortino F 2003 *Europhys. Lett.* **64** 197
[184] Chong S-H, Aichele M, Fuchs M and Baschnagel J 2005 Structural and conformational dynamics of supercooled polymer melts: insights from first-principles theory and simulations, in preparation
[185] Kob W 2003 *Slow Relaxations and Nonequilibrium Dynamics in Condensed Matter* ed J-L Barrat, M Feigelmann, J Kurchan and J Dalibard (Les Ulis: EDP Sciences) pp 201–69 (Berlin: Springer)
[186] Verdier P H 1966 *J. Chem. Phys.* **45** 2118
[187] Urakawa O, Swallen S F, Ediger M D and von Meerwall E D 2004 *Macromolecules* **37** 1558
[188] Chang I *et al* 1994 *J. Non-Cryst. Solids* **172–174** 248
[189] Swallen S F, Bonvallet P, McMahon R J and Ediger M D 2003 *Phys. Rev. Lett.* **90** 015901
[190] Sillescu H 1999 *J. Non-Cryst. Solids* **243** 81
[191] Ediger M D 2000 *Annu. Rev. Phys. Chem.* **51** 99
[192] Glotzer S C 2000 *J. Non-Cryst. Solids* **274** 342
[193] Richert R 2002 *J. Phys.: Condens. Matter* **14** R703
[194] Gebremichael Y, Schrøder T B, Starr F W and Glotzer S C 2001 *Phys. Rev.* E **64** 051503
[195] Kob W *et al* 1997 *Phys. Rev. Lett.* **79** 2827
[196] Donati C *et al* 1998 *Phys. Rev. Lett.* **80** 2338
[197] Donati C *et al* 1999 *Phys. Rev.* E **60** 3107
[198] Sciortino F, Gallo P, Tartaglia P and Chen S-H 1996 *Phys. Rev.* E **54** 6331
[199] Zorn R 1997 *Phys. Rev.* B **55** 6249
[200] Weeks E *et al* 2000 *Science* **287** 627
[201] Kegel W K and van Blaaderen A 2000 *Science* **287** 290
[202] Allegrini P, Douglas J F and Glotzer S C 1999 *Phys. Rev.* E **60** 5714
[203] Garrahan J P and Chandler D 2002 *Phys. Rev. Lett.* **89** 035704
[204] Berthier L and Garrahan J P 2003 *J. Chem. Phys.* **119** 4367
[205] Whitelam S, Berthier L and Garrahan J P 2004 *Phys. Rev. Lett.* **92** 185705
[206] Cates M E and Candau S J 1990 *J. Phys.: Condens. Matter* **2** 6869

[207] Wittmer J P, Milchev A and Cates M E 1998 *J. Chem. Phys.* **109** 834

[208] Doliwa B and Heuer A 2003 *J. Phys.: Condens. Matter* **15** S849

[209] Vogel M, Doliwa B, Heuer A and Glotzer S C 2004 *J. Chem. Phys.* **120** 4404

[210] Gebremichael Y, Vogel M and Glotzer S C 2004 *J. Chem. Phys.* **120** 4415

[211] Vogel M and Glotzer S C 2004 *Phys. Rev. Lett.* **92** 255901

[212] Teboul V *et al* 2004 *Eur. Phys. J.* B **40** 49

[213] Büchner S and Heuer A 2000 *Phys. Rev. Lett.* **84** 2168

[214] Doliwa B and Heuer A 2002 *J. Non-Cryst. Solids* **307–310** 32

[215] Lačević N, Starr F W, Schrøder T B and Glotzer S C 2003 *J. Chem. Phys.* **119** 7372

[216] Donati C, Glotzer S C and Poole P H 1999 *Phys. Rev. Lett.* **82** 5064

[217] Sillescu H, Böhmer R, Diezemann G and Hinze G 2002 *J. Non-Cryst. Solids* **307–310** 16

[218] Glotzer S C, Novikov V N and Schrøder T B 2000 *J. Chem. Phys.* **112** 509

[219] Doliwa B and Heuer A 2000 *Phys. Rev.* E **61** 6898

[220] Yamamoto R and Onuki A 1998 *Phys. Rev. Lett.* **81** 4915

[221] Adam G and Gibbs J H 1965 *J. Chem. Phys.* **43** 139

[222] Frick B, Zorn R and Büttner H (ed) 2000 *Proc. Int. Workshop on Dynamics in Confinement*; *J. Physique Coll.* IV **10** 3

[223] Frick B, Koza M and Zorn R (ed) 2003 *Proc. 2nd Int. Workshop on Dynamics in Confinement*; *Eur. Phys. J.* E **12** 5

[224] Morineau D, Xia Y and Alba-Simionesco C 2002 *J. Chem. Phys.* **117** 8966

[225] Alba-Simionesco C *et al* 2003 *Eur. Phys. J.* E **12** 19

[226] Jackson C L and McKenna G B 1996 *Chem. Mater.* **8** 2128

[227] Wendt H and Richert R 1999 *J. Phys.: Condens. Matter* **11** A199

[228] Pissis P *et al* 1998 *J. Phys.: Condens. Matter* **10** 6205

[229] Arndt M *et al* 1997 *Phys. Rev. Lett.* **79** 2077

[230] Levent Demirel A and Granick S 2001 *J. Chem. Phys.* **115** 1498

[231] Keddie J L, Jones R A L and Cory R A 1994 *Europhys. Lett.* **27** 59

[232] Teichroeb J H and Forrest J A 2003 *Phys. Rev. Lett.* **91** 235701

[233] Sharp J S and Forrest J A 2003 *Phys. Rev. Lett.* **91** 235701

[234] Forrest J A 2002 *Eur. Phys. J.* E **8** 261

[235] Herminghaus S, Jacobs K and Seemann R 2001 *Eur. Phys. J.* E **5** 531

[236] Herminghaus S 2002 *Eur. Phys. J.* E **8** 237

[237] Herminghaus S, Seemann R and Landfester K 2004 *Phys. Rev. Lett.* **93** 017801

[238] Johannsmann D 2002 *Eur. Phys. J.* E **8** 257

[239] Reiter G 2002 *Eur. Phys. J.* E **8** 251

[240] Kajiyama T, Tanaka K and Takahara A 1998 *Polymer* **39** 4665

[241] Grohens Y *et al* 2002 *Eur. Phys. J.* E **8** 217

[242] Fukao K and Miyamoto Y 2000 *Phys. Rev.* E **61** 1743

[243] Fukao K and Miyamoto Y 2001 *Phys. Rev.* E **64** 011803

[244] Schönhals A and Stauga A 1998 *J. Chem. Phys.* **108** 5130

[245] Schönhals A, Goering H, Brzezinka K W and Schick C 2003 *J. Phys.: Condens. Matter* **15** S1139

[246] Kim J H, Jang J and Zin W-C 2001 *Langmuir* **17** 2703

[247] Tsui O K C and Zhang H F 2001 *Macromolecules* **34** 9139

[248] Bernazzani P, Simon S L, Plazek D J and Ngai K L 2002 *Eur. Phys. J.* E **8** 201

[249] Bliznyuk V N, Assender H E and Briggs G A D 2002 *Macromolecules* **35** 6613

[250] Ellison C J and Torkelson J M 2003 *Nat. Mater.* **2** 695

[251] Singh L, Ludovice P J and Henderson C L 2004 *Thin Solid Films* **449** 231

[252] Fryer D S, Nealey P F and de Pablo J J 2000 *Macromolecules* **33** 6439

[253] Xu G and Mattice W L 2003 *J. Chem. Phys.* **118** 5241

[254] Starr F W, Schrøder T B and Glotzer S C 2001 *Phys. Rev.* E **64** 021802

[255] Starr F W, Schrøder T B and Glotzer S C 2002 *Macromolecules* **35** 4481

[256] Yoshimoto K, Jain T S, Nealey P F and de Pablo J J 2005 *J. Chem. Phys.* **122** 144712

[257] Jain T S and de Pablo J J 2004 *Phys. Rev. Lett.* **92** 155505

[258] Jain T S and de Pablo J J 2002 *Macromolecules* **35** 2167

[259] Böhme T R and de Pablo J J 2002 *J. Chem. Phys.* **116** 9939

[260] Torres J A, Nealey P F and de Pablo J J 2000 *Phys. Rev. Lett.* **85** 3221

[261] Mansfield K F and Theodorou D N 1991 *Macromolecules* **24** 6283

[262] Manias E, Kuppa V, Yang D-K and Zax D B 2001 *Colloids Surf.* A **187/188** 509

[263] Baljon A R C, Van Weert M H M, Barber DeGraaff R and Khare R 2005 *Macromolecules* **38** 2391

[264] Baljon A R C, Billen J and Khare R 2004 *Phys. Rev. Lett.* **93** 255701

[265] Roder A, Kob W and Binder K 2001 *J. Chem. Phys.* **114** 7602

[266] Scheidler P, Kob W and Binder K 2000 *Europhys. Lett.* **52** 277

[267] Scheidler P, Kob W and Binder K 2002 *Europhys. Lett.* **59** 701

[268] Gallo P, Pellarin R and Rovere M 2002 *Europhys. Lett.* **57** 212

[269] Gallo P, Rovere M and Spohr E 2000 *J. Chem. Phys.* **113** 11324

[270] Fehr T and Löwen H 1995 *Phys. Rev.* E **52** 4016

[271] Teboul V and Alba-Simionesco C 2002 *J. Phys.: Condens. Matter* **14** 5699

[272] Böddeker B and Teichler H 1999 *Phys. Rev.* E **59** 1948

[273] de Gennes P G 2000 *Eur. Phys. J.* E **2** 201

[274] McCoy J D and Curro J G 2002 *J. Chem. Phys.* **116** 9154

[275] Truskett T M and Ganesan V 2003 *J. Chem. Phys.* **119** 1897

[276] Mittal J, Shah P and Truskett T M 2004 *J. Phys. Chem.* B **108** 19769

[277] Chow T S 2002 *J. Phys.: Condens. Matter* **14** L333

[278] Long D and Lequeux F 2001 *Eur. Phys. J.* E **4** 371

[279] Merabia S, Sotta P and Long D 2004 *Eur. Phys. J.* E **15** 189

[280] Mayes A M 1994 *Macromolecules* **27** 3114

[281] Ngai K L 2003 *Eur. Phys. J.* E **12** 93

[282] Roth C B and Dutcher J R 2005 *Soft Materials: Structure and Dynamics* ed J R Dutcher and A G Marangoni (New York: Dekker) pp 1–38

[283] Alcoutlabi M and McKenna G B 2005 *J. Phys.: Condens. Matter* **17** R461

[284] Mischler C, Baschnagel J and Binder K 2001 *Adv. Colloid Interface Sci.* **94** 197

[285] Netz R R and Andelman D 2003 *Phys. Rep.* **380** 1

[286] Frischknecht A L and Curro J G 2004 *J. Chem. Phys.* **121** 2788

[287] Müller M, MacDowell L G and Yethiraj A 2003 *J. Chem. Phys.* **118** 2929

[288] Eisenriegler E and Maassen R 2002 *J. Chem. Phys.* **116** 449

[289] Hooper J B, McCoy J D and Curro J G 2000 *J. Chem. Phys.* **112** 3090

[290] Hooper J B *et al* 2000 *J. Chem. Phys.* **112** 3094

[291] Yethiraj A 1998 *J. Chem. Phys.* **109** 3269

[292] Brazhnik P K, Freed K F and Tang H 1994 *J. Chem. Phys.* **101** 9143

[293] Sen S, Cohen J M, McCoy J D and Curro J G 1994 *J. Chem. Phys.* **101** 9010

[294] Müller M 2002 *J. Chem. Phys.* **116** 9930

[295] Cavallo A *et al* 2005 *J. Phys.: Condens. Matter* **17** S1697

[296] Mischler C, Baschnagel J, Dasgupta S and Binder K 2002 *Polymer* **43** 467

[297] Baschnagel J and Binder K 1995 *Macromolecules* **28** 6808

[298] Götzelmann B and Dietrich S 1997 *Phys. Rev.* E **55** 2993

[299] Jang J H and Mattice W L 2000 *Macromolecules* **33** 1467

[300] Yethiraj A 1994 *J. Chem. Phys.* **101** 2489

[301] Yethiraj A and Hall C K 1990 *Macromolecules* **23** 1865

[302] Kumar S K, Vacatello M and Yoon D Y 1990 *Macromolecules* **23** 2189

[303] Bitsanis I and Hadziioannou G 1990 *J. Chem. Phys.* **92** 3827

[304] Kim J H, Jang J and Zin W-C 2000 *Langmuir* **16** 4067

[305] Park C H *et al* 2004 *Polymer* **45** 4507

[306] Forrest J A, Dalnoki-Veress K and Dutcher J R 1997 *Phys. Rev.* E **56** 5705

[307] Reiter G and de Gennes P G 2001 *Eur. Phys. J.* E **6** 25

[308] de Gennes P G 2001 *Eur. Phys. J.* E **6** 421

[309] Jäckle J and Kawasaki K 1995 *J. Phys.: Condens. Matter* **7** 4351

[310] Jäckle J 1998 *J. Phys.: Condens. Matter* **10** 7121

[311] Kim H *et al* 2003 *Phys. Rev. Lett.* **90** 068302

[312] Madsen A *et al* 2004 *Phys. Rev. Lett.* **92** 096104

[313] Long D 2002 *Eur. Phys. J.* E **8** 245

[314] Baschnagel J 2002 *Eur. Phys. J.* E **8** 247

[315] Reiter G 1994 *Macromolecules* **27** 3046

[316] Tracht U *et al* 1998 *Phys. Rev. Lett.* **81** 2727

[317] Merabia S and Long D 2002 *Eur. Phys. J.* E **9** 195

[318] Bunde A and Havlin S 1996 *Fractals and Disordered Systems* ed A Bunde and S Havlin (Berlin: Springer) pp 59–113

[319] Binder K, Landau D and Müller M 2003 *J. Stat. Phys.* **110** 1411

[320] Binder K 1983 *Phase Transitions and Critical Phenomena* vol 8, ed C Domb and J L Lebowitz (New York: Academic) pp 1–144

[321] Henkel M, Andrieu S, Bauer P and Piecuch M 1998 *Phys. Rev. Lett.* **80** 4783

[322] Berriot J *et al* 2003 *Europhys. Lett.* **64** 50

[323] Starr F W, Sastry S, Douglas J F and Glotzer S C 2002 *Phys. Rev. Lett.* **89** 125501

[324] Roth C B and Dutcher J R 2003 *Eur. Phys. J.* E **12** S103

[325] Pelissetto A and Vicari E 2002 *Phys. Rep.* **368** 549

[326] Berthier L 2003 *Phys. Rev. Lett.* **91** 055701

[327] Barrat J-L and Bocquet L 1999 *Faraday Discuss.* **112** 119

[328] Fuchs M and Kroy K 2002 *J. Phys.: Condens. Matter* **14** 9223

[329] Giovambattista N, Buldyrev S V, Starr F W and Stanley H E 2003 *Phys. Rev. Lett.* **90** 085506

[330] Smith G D, Bedrov D and Borodin O 2003 *Phys. Rev. Lett.* **90** 226103

[331] Tanguy A, Wittmer J P, Leonforte F and Barrat J-L 2002 *Phys. Rev.* B **66** 174205

[332] Leonforte F *et al* 2005 Continuum limit of amorphous elastic bodies (III): three dimensional systems *Preprint* cond-mat/0505610

[333] Büchner S and Heuer A 1999 *Phys. Rev.* E **60** 6507

[334] Kim K and Yamamoto R 2000 *Phys. Rev.* E **61** R41

[335] Horbach J, Kob W, Binder K and Angell C A 1996 *Phys. Rev.* E. **54** R5897

[336] Horbach J and Kob W 1999 *Phil. Mag.* B **79** 1981

[337] Jäckle J and Kawai H 2001 *Physica* A **291** 184

[338] Yamamoto R and Onuki A 2002 *J. Chem. Phys.* **117** 2359

[339] Wallace M L, Joós B and Plischke M 2004 *Phys. Rev.* E **70** 041501

[340] Barrat J-L, Feigelmann M, Kurchan J and Dalibard J (ed) 2003 *Slow Relaxations and Nonequilibrium Dynamics in Condensed Matter* (Paris: EDP Sciences) (Berlin: Springer)

[341] Yoshimoto K *et al* 2004 *Phys. Rev. Lett.* **93** 175501

[342] Sciortino F 2000 *Chem. Phys.* **258** 307

[343] Baschnagel J 1994 *Phys. Rev.* B **49** 135

[344] Bartsch E *et al* 1997 *J. Chem. Phys.* **106** 3743

[345] Goldstein M 1969 *J. Chem. Phys.* **51** 3728

[346] Stillinger F H and Weber T A 1984 *Science* **225** 983

[347] Mézard M and Parisi G 2000 *J. Phys.: Condens. Matter* **12** 6655

[348] Parisi G 2003 *Slow Relaxations and Nonequilibrium Dynamics in Condensed Matter* ed J-L Barrat, M Feigelmann, J Kurchan and J Dalibard (Les Ulis: EDP Sciences) pp 271–365 (Berlin: Springer)

[349] Krakoviack V and Alba-Simionesco C 2000 *Europhys. Lett.* **51** 420

[350] Sciortino F, Kob W and Tartaglia P 2000 *J. Phys.: Condens. Matter* **12** 6525

[351] La Nave E *et al* 2003 *J. Phys.: Condens. Matter* **15** S1085

[352] Sastry S, Debenedetti P G and Stillinger F H 1998 *Nature* **393** 554

[353] Brumer Y and Reichman D 2004 *Phys. Rev.* E **69** 041202

[354] Angelani L *et al* 2002 *J. Chem. Phys.* **116** 10297

[355] Angelani L, Ruocco G, Sampoli M and Sciortino F 2003 *J. Chem. Phys.* **119** 2120

[356] Angelani L, De Michele C, Ruocco G and Sciortino F 2004 *J. Chem. Phys.* **121** 7533

[357] Doliwa B and Heuer A 2003 *Phys. Rev.* E **67** 030501

[358] Doliwa B and Heuer A 2003 *Phys. Rev.* E **67** 031506

[359] Doliwa B and Heuer A 2003 *Phys. Rev. Lett.* **91** 235501

[360] Sastry S 2001 *Nature* **409** 164

[361] Scala A *et al* 2000 *Nature* **406** 166

[362] Mossa S *et al* 2002 *Phys. Rev.* E **65** 041205

[363] Berthier L and Garrahan J P 2003 *J. Chem. Phys.* **68** 041201

[364] Poon W C K 2002 *J. Phys.: Condens. Matter* **14** R859

[365] Puertas A M, Fuchs M and Cates M E 2002 *Phys. Rev. Lett.* **88** 098301

[366] Dawson K *et al* 2000 *Phys. Rev.* E **63** 011401

[367] Kröger M and Hess S 2000 *Phys. Rev. Lett.* **85** 1128

[368] Everaers R *et al* 2004 *Science* **303** 823

[369] Todd B D, Evans D J and Daivis P J 1995 *Phys. Rev.* E **52** 1627

[370] Thompson P A and Robbins M O 1990 *Phys. Rev.* A **41** 6830

[371] Varnik F, Bocquet L, Barrat J-L and Berthier L 2003 *Phys. Rev. Lett.* **90** 095702

[372] Middelton T F, Hernández-Rojas J, Mortensen P N and Wales D J 2001 *Phys. Rev.* B **64** 184201

[373] Dzugutov M 1992 *Phys. Rev.* A **46** R2984
[374] Doye J P K, Wales D J, Zetterling F H M and Dzugutov M 2003 *J. Chem. Phys.* **118** 2792
[375] Di Leonardo R, Angelani L, Parisi G and Ruocco G 2000 *Phys. Rev. Lett.* **84** 6054
[376] Fischer E W 1993 *Physica* A **201** 183
[377] Schweizer K S and Saltzman E J 2004 *J. Chem. Phys.* **121** 1984
[378] Pesché R, Kollmann M and Nägele G 2001 *J. Chem. Phys.* **114** 8701
[379] Branchio A J, Nägele G and Bergenholtz J 2000 *J. Chem. Phys.* **113** 3381
[380] Hoffmann G P and Löwen H 2001 *J. Phys.: Condens. Matter* **13** 9197
[381] Shaffer J S 1994 *J. Chem. Phys.* **101** 4205
[382] Shaffer J S 1995 *J. Chem. Phys.* **103** 761
[383] Barrat J-L, Götze W and Latz A 1989 *J. Phys.: Condens. Matter* **1** 7163
[384] Barrat J-L and Latz A 1990 *J. Phys.: Condens. Matter* **2** 4289
[385] Tölle A 2001 *Rep. Prog. Phys.* **64** 1473
[386] Götzelmann B, Haase A and Dietrich S 1996 *Phys. Rev.* E **53** 3456
[387] Semenov A N and Johner A 2003 *Eur. Phys. J.* E **12** 469
[388] Granick S *et al* 2003 *J. Polym. Sci.* B **41** 2755
[389] Efremov M Y *et al* 2004 *Macromolecules* **37** 4607
[390] Hutcheson S A and McKenna G B 2005 *Phys. Rev. Lett.* **94** 076103
[391] Yamamoto R and Kim K 2000 *J. Physique Coll.* IV **10** 15
[392] Mattson J, Forrest J A and Börjesson L 2000 *Phys. Rev.* E **62** 5187
[393] Arndt M, Stannarius R, Gorbatschow W and Kremer F 1996 *Phys. Rev.* E **54** 5377
[394] Stillinger F H, Debenedetti P G and Truskett T M 2001 *J. Phys. Chem.* B **105** 11809